QUANTITATIVE THERMAL INFRARED ANALYSES OF VOLCANIC PROCESSES AND PRODUCTS: APPLICATION TO BEZYMIANNY VOLCANO, RUSSIA

by

ADAM JOSEPH CARTER

BSc Geological Sciences (honours), University of Leeds, Yorkshire, England 2001

DEA Volcanic and Magmatic Studies, University of Blaise Pascal, Clermont-Ferrand, France, 2003

Submitted to the Graduate Faculty of

Arts and Sciences in partial fulfilment

of the requirements for the degree of

Doctor of Philosophy

University of Pittsburgh

2008

UNIVERSITY OF PITTSBURGH

FACULTY OF ARTS AND SCIENCES

This dissertation was presented

by

ADAM JOSEPH CARTER

It was defended on

1 August, 2008

and approved by

Michael S. Ramsey (Primary Advisor), Associate Professor, University of Pittsburgh

Alexander B. Belousov, Professor, Institute of Marine Geology and Geophysics, Yuzno-Sakhalinsk, Russia (External Examiner)

William Harbert, Associate Professor, University of Pittsburgh

Michael Rosenmeier, Assistant Professor, University of Pittsburgh

Ian P. Skilling, Assistant Professor, University of Pittsburgh

QUANTITATIVE THERMAL INFRARED ANALYSES OF VOLCANIC PROCESSES AND PRODUCTS: APPLICATION TO BEZYMIANNY VOLCANO, RUSSIA

Adam Joseph Carter, BSc, DEA

University of Pittsburgh, 2008

Bezymianny (55.98°N, 160.59°E) is a Holocene andesitic composite volcano with a summit elevation of approximately 2,900 m and is located on the Kamchatka Peninsula, eastern Russia. Previously inactive for about 1,000 years, Bezymianny reactivated in 1955, culminating in a cataclysmic eruption on 30 March 1956. This directed blast generated a 1.3 km (north–south) by 2.8 km (east–west) horseshoe shaped crater opening to the east, similar in morphology and activity to Mt. St. Helens (USA). During the last 30 years Bezymianny has been regularly active, erupting one to two times per year on average. This work focuses on field-based and remote sensing observations of explosive eruptions and their products at Bezymianny, concentrating on the pyroclastic flow (PF) deposits on the southeast flank. The events of March 2000, January 2005, December 2006, May 2007 and October 2007 were focused on to elucidate information on the pyroclastic flow (PF) deposits that were emplaced. Two principal themes were addressed: (1) A thermal infrared (TIR) investigation of the eruptive events and products. This encompassed ground-based field work, Forward Looking Infrared Radiometer (FLIR) image data, and spaceborne data from the Advanced Spaceborne Thermal Emission and Reflection Radiometer (ASTER). (2) A micrometer-scale textural investigation of vesicular block and ash samples collected in the field on the pyroclastic flow deposits. Scanning Electron Microscope (SEM)

images were used to generate micron-scale digital elevation models (DEM) for the surfaces of each volcanic sample collected. These were compared to TIR emission spectra that were deconvolved to estimate surface vesicularity. This work demonstrates the utility of TIR observations from satellite, aerial, and ground-based data that, in combination with standard geological mapping, provide timely, accurate, and quantitative remote sensing data to assist in the prediction and monitoring of explosive volcanoes.

TABLE OF CONTENTS

LIST OF TABLES

LIST OF FIGURES

PREFACE

"*We know from science that nothing in the universe exists as an isolated or independent entity*" (Margaret J. Wheatley).

Firstly, I would like to sincerely thank Michael Ramsey for several years of advice and support, and the opportunity to be part of such an interesting and challenging project.

My committee members, Ian Skilling, Michael Rosenmeier, and Bill Harbert are also thanked for their support with my work. My external committee member Alexander Belousov is also thanked for his time spent in the field, discussions, and general advice.

This project has involved many international collaborators, in particular the Russian scientists and administrators, without whom this would not have been possible. Many, many thanks to Alexander Belousov and Marina Belousova, Olga Girina, and Alexei Ozerov for their field support, assistance and collaboration in writing scientific articles. At the institute of Volcanology and Seismology (IVS), Kamchatka, I would like to thank Evgenni Gordeev for his support in arranging our logistics, and to Oxana Evdokimova, who spent a long time over the years arranging our visits.

Several of the people involved have also become my co-authors, who I acknowledge and thank for their time on this work: Michael Ramsey, Alexander Belousov, Olga Girina, Ian

Skilling, Adam Durant, and Amy Wolfe. Thank you all for edits, advice, and the determination to progress through the publishing process.

In Alaska, thanks to Alaska Volcano Observatory (AVO) members Rick Wessels and Tina Neal for participating in the project. At the University of Alaska, Fairbanks (UAF), thanks to Jon Dehn ("Polar Bear"), John Eichelberger, Pavel Izbekov, and Mike West for assistance and collaboration in the field. Every trip to Russia is always an adventure.

In the field, many people have spent their time in the field on Bezymianny during 2004, 2005, and 2007, chasing around after me: Marina Belousova, Shellie Rose, Susan Wacaster, Courtney Kearney, Andrea Steffke, Julie Calkins, Lara Owens, Jill Shipman, Andreas Auer, Saskia van Manen, and Geofrroy Avard. A special thank you also goes to Jeff Byrnes, who not only co-ordinated the 2004 field campaign, he also let me crash on his sofa until I found an apartment in Pittsburgh. I should also thank his wife, Jeanette, who in combination with their dog Jake, made me very welcome.

Several organizations must be mentioned for funding: NASA (MSR), Andrew Mellon Foundation (2 years, AJC), National Geographic Expeditions (MSR, AJC), National Science Foundation (AJC), the University Centre for International Studies (UCIS, AJC), Henry Leighton Memorial Scholarships (3 years, AJC), Geological Society of America (GSA, AJC), and the University of Pittsburgh Grad Expo awards (2 years, AJC).

In the Geology dept. office, thanks to Matt Romick, Deanna Hitchcock, Dolly Chavez, and new members Lorraine Robbins and Shannon Granahan for all their logistical support.

Thanks to all the other Grad students in the IVIS team: Shellie Rose, Veronica Peet (and honorary members Chris Zebley and Inca), Topher Hughes, Rachel Lee, and my great friend Stephen ("Beast") Scheidt. Shellie's cakes, Topher's dry sense of humour, Rachel's dancing,

Veronica's teasing (!), and Steve allowing me to win once in a while at racquetball, all made it worthwhile. They are all great people and have been a close-knit family during my time here- good luck to you all getting finished!

Other Grad students, Nathan Stansell and Byron Steinman were always good company for Steelers/Penguins/Pirates games. Sherry Stafford and Tim Seiple should also be mentioned for their kindness when I first arrived here. Best wishes to Daniel Lao Davila who is also finishing around the same time as me, *buena suerte* in the future!

I thank all of my friends for their support over the years and making me feel very welcome in the U.S., in particular Jenn Hyland for being my American sister, Scott Carslaw and Bill Byrne for the DJing, Jason ("night time camera") Quackenbush for being a top housemate in the Penthouse, Chris Thomas for his artistic influence (and sushi), Jim Leety for great darts, Matt Crouch for his wiffle ball skills, and the aptly named Marcin ("Mouth") Krieger for his wholehearted opinions on pretty much everything, and Julie, his partner.

Back in the homeland (home of cricket, real football, and good tea), I thank my good friends Charlie ("Chateau Lafitte") Maxwell, Karl ("Cliff-hanger") Garnett, and Mark ("Hippy") Bell for keeping in touch despite the 6,000 mile distance. My sister, Amy, for being my best friend- she's my hero on many levels. Thanks for looking out for me Ams. Thanks also to Paul, my step-father, for his many trips at all hours to the airport to pick me up from my regular travels. Thanks to Hal Lister for his tales of survival in Antarctica in the 1950's, and to Mr. Brambles (Queen Katherine School, Kendal) who both inspired me to pursue Geology. In Ireland, thanks to my Aunty Arlene and Uncle Kevin, for supporting me and keeping in touch.

To any people I may have forgotten to mention, I apologize. Countless people have helped in my travels to volcanoes around the world. I truly appreciated the opportunity to travel at an early age and meet so many people from such diverse backgrounds.

Finally, special thanks go to Robyn, thank you for your love and support.

I dedicate my dissertation and publications to my father, Denis Carter, who sadly passed away from Motor Neurone Disease in 1995, but knew my goals, determination, and interests even then, and to my mother, Jennifer Harris, who continues to amaze me in her kindness, understanding, and success.

AJC, July 2008.

1 INTRODUCTION

1.1 EXPLOSIVE VOLCANISM AND GEOGRAPHIC SETTING

Globally, over 1500 subaerial volcanoes have erupted in the last 10,000 years, many of which have not been investigated in detail or have adequate monitoring systems installed (Simkin and Siebert, 1994). The Pacific "Ring of Fire" marks the boundary of the Pacific plate that is undergoing subduction, which is responsible for the majority of subaerial explosive volcanism on Earth (Francis, 1993). One area of intense volcanic activity within the ring of fire is the 700 km long Kuril-Kamchatka Arc, which contains 68 active volcanoes, 29 of which are on the Kamchatka Peninsula (Fedotov et al., 1991). The peninsula is bound to the west by the Sea of Ohkotsk and to the east by the Pacific Ocean, connecting to mainland Russia to the north (Figure 1). To the east, the central mountain belt is connected to the Aleutian trench which forms the northern part of the arc, containing at least 41 historically active volcanoes that extend eastward into the mainland Alaska, USA (Brantley et al., 2004).

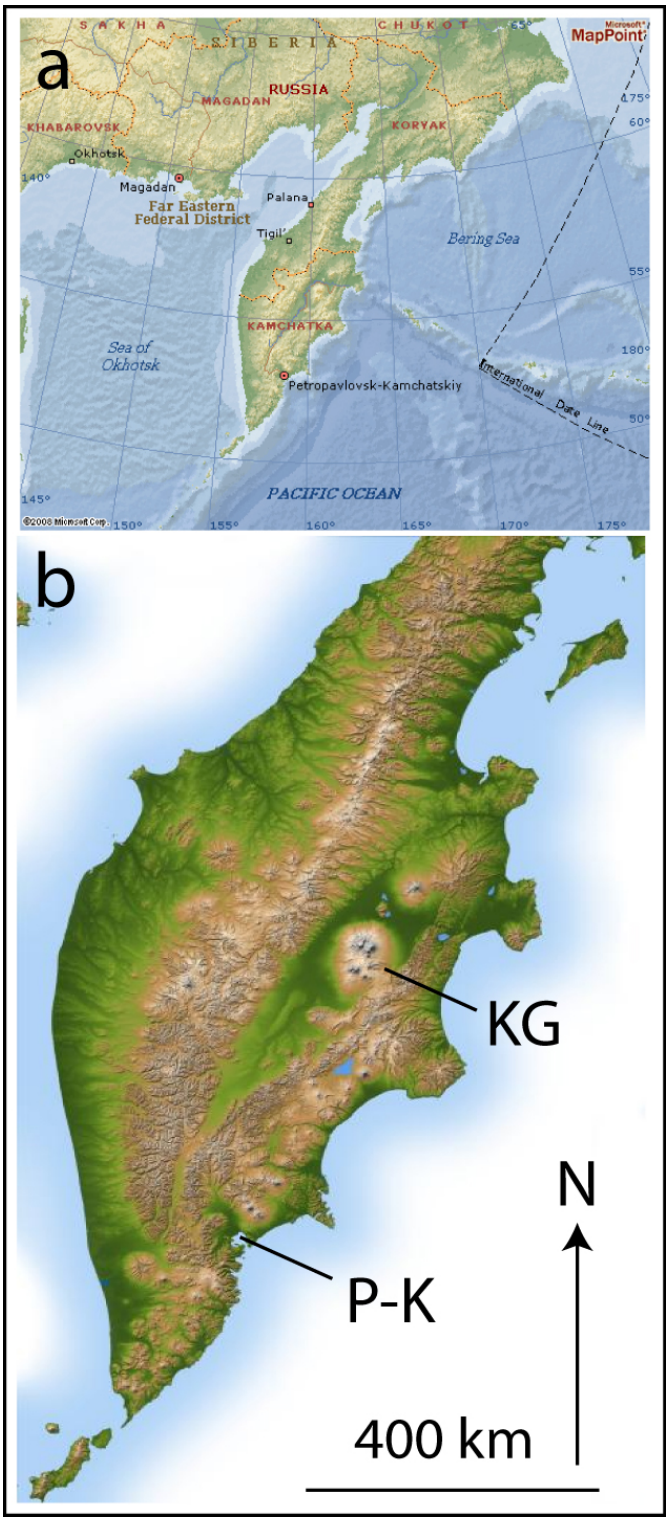

Figure 1 Location map of the Kamchatka Peninsula. (a) The peninsula extends from mainland Russia, between the Sea of Okhotsk and the Pacific Ocean and the Aleutian arc extends east towards Alaska. Image courtesy of Microsoft MapPoint. URL: http://encarta.msn.com/map_701513589/kamchatka.html (b) NASA/JPL topographic image of the peninsula showing the location of Petropavlovsk-Kamchatsky (P-K), the main city, and the Klyuchevskaya volcanic group (KG) which is located the central Kamchatka depression. URL: http://commons.wikimedia.org/wiki/Image:Kamchatka_peninsula_topo.jpg

Relatively inaccessible for foreign visitors prior to 1991 due to the collapse of the Soviet Union, the Kamchatka Peninsula now provides a unique natural laboratory to study volcanism and the impact of volcanic activity.

1.2 TECTONIC SETTING AND HISTORY OF KAMCHATKA

Subduction-related, submarine volcanism gave rise to the Kamchatka Peninsula during the late Cretaceous period, beginning ~65 Ma (Fedotov et al., 1991). Earlier volcanism stemmed from the "backbone" of the peninsula, named the Median Kamchatka Volcanic Belt. More recent Quaternary activity has been concentrated in the Eastern volcanic belt, closer to the Pacific coast. The bulk of the landmass is thought to have been constructed in the Pleistocene as flood basalt eruptions, emerging above sea level to initially form a series of volcanic islands (Fedotov et al., 1991). During the Quaternary period glaciers caused large scale erosion, as the last major ice retreated around 10,000 years ago. Today, 29 active volcanoes exist on the Kamchatka Peninsula (see Table 1), which is ~8% of the total number of volcanoes in the "Ring of Fire" (Fedotov et al., 1991).

Table 1 List of potentially active volcanoes of Kamchatka (based on information in Fedotov et al. 1991), updated in December 2007. Volcanoes marked in bold form the Klyuchevskaya group.

	Volcano	**Last known eruption**
1	Avachinsky	2001
2	**Bezymianny**	**2007**
3	Bolshoi Semiachik	1976
4	Dzenzursky	Holocene
5	Gamchen	Holocene
6	Gorely	1986
7	Ichinsky	Holocene
8	Iliyinsky	Holocene
9	Kambalny	Holocene
10	Karymsky	2007
11	Kikhpinych	600 B.P.
12	Kizimen	1927
13	**Klyuchevskoy**	**2007**
14	Komarov	Holocene
15	Koryasky	1956
16	Koshelev	17th Century
17	Krasheninnikov	1100 B.P.
18	Kronotsky	1941
19	Ksudach	1907
20	Maly Semiachik	1804
21	Mutnovsky	2000
22	**New Tolbachik**	**1975**
23	Opala	1894
24	**Plosky Tolbachik**	**1975**
25	Sheveluch	2007
26	**Ushkovsky**	**1890**
27	Uzon Caldera/Valley of Geysers	1986
28	Zheltovsky	1923
29	Zhupanovsky	1956

The volcanoes marked in bold represent the Klyuchevskaya group, a cluster of volcanoes named after the largest active volcano in Europe and Asia: the 4,850 m high Klyuchevskoy (meaning *key* in Russian*)*. A wide variety of magma compositions and activity types have been observed in the Klyuchevskaya group, from Hawaiian style fire fountain products (*e.g.* Tolbachik in 1976), to highly evolved magmas with consequent explosive eruptions, dome growth, and ash-emitting eruptions (*e.g.* Bezymianny Volcano, 1956-present). Spatially, the group lies above a point of intense magma production where the Aleutian-Kamchatka arc forms a ~90° angle. Significant slab loss at the "Aleutian-Kamchatka junction" (AKJ) may be responsible for the elevated thermal flux and magma production observed locally (Levin et al., 2002; Yogodzinski et al., 2001).

The Kamchatka Peninsula is comprised of a series of accreted terranes containing a complex group of sedimentary, igneous and metamorphic suites (*e.g.* Harbert, 1992; Harbert et al., 1998). From south to north, the subducting Pacific plate dip angle shallows from 55º to 35º at the Wadati-Benioff zone (Peyton et al., 2001). The greatest depth of the Pacific slab is 500 km in the south, becoming more shallow in the north (Gorbatov et al., 2000). The slab is ~70 km thick and the Mohorovic discontinuity ("Moho") is ~35 km under the peninsula (Gorbatov et al., 2000). Within a tectonic framework of the north Pacific region, Mackey et al. (1997), using seismic data, proposed that a Bering plate exists, further complicating tectonic interpretation in the Kamchatka and Chukotka regions.

1.3 THE KLYUCHEVSKAYA VOLCANIC GROUP

The Klyuchevskaya group lies isolated within a portion of the peninsula named the Central Kamchatka Depression (CKD) The CKD contains large volumes of sedimentary material due to erosion of mountains within the Sredinny ridge to the west (Gorbatov et al., 2000). The group is comprised of the following volcanoes: Klyuchevskoy (4850 m), Bezymianny (~2900 m), Ushkovsky (3943 m) and Ostry and Plosky Tolbachik (3682 and 3085 m respectively), all of which are considered active (Fedotov et al., 1991). Additionally Kamen (4575 m), Krestovsky (3943 m), Ovalnaya (meaning *oval*) Zimina (3081 m), Ostraya ("sharp") Zimina (2744 m), Bolashaya Udina (2943 m), Srednyaya (2990 m), Zarechny (un-measured) and Kharachinsky (un-measured) are all considered inactive or are non-volcanic (Fedotov et al., 1991). The volcanoes in the centre of the group are displayed on an ASTER-derived map (Figure 2). In 2007 alone, Klyuchevskoy and Bezymianny each erupted. In addition, Sheveluch (80 km to the northeast) and Karymsky (230 km to the southeast) also erupted at least once, highlighting the intense activity over a relatively small geographic area.

1.4 BEZYMIANNY VOLCANO

Bezymianny Volcano (55.98º N, 160.59º E, ~2,900 m elevation), which means *no name* in Russian, is a complex stratovolcano (Figure 3). It lies 4.8 km south of Kamen, and 9.5 km southeast of Klyuchevskoy. The basement of the volcano consists of volcanic sequences from the southern flank of Kamen Volcano. These sequences are primarily basalts and basaltic andesites up to 1300 m thick (Bogoyavlenskaya et al., 1991).

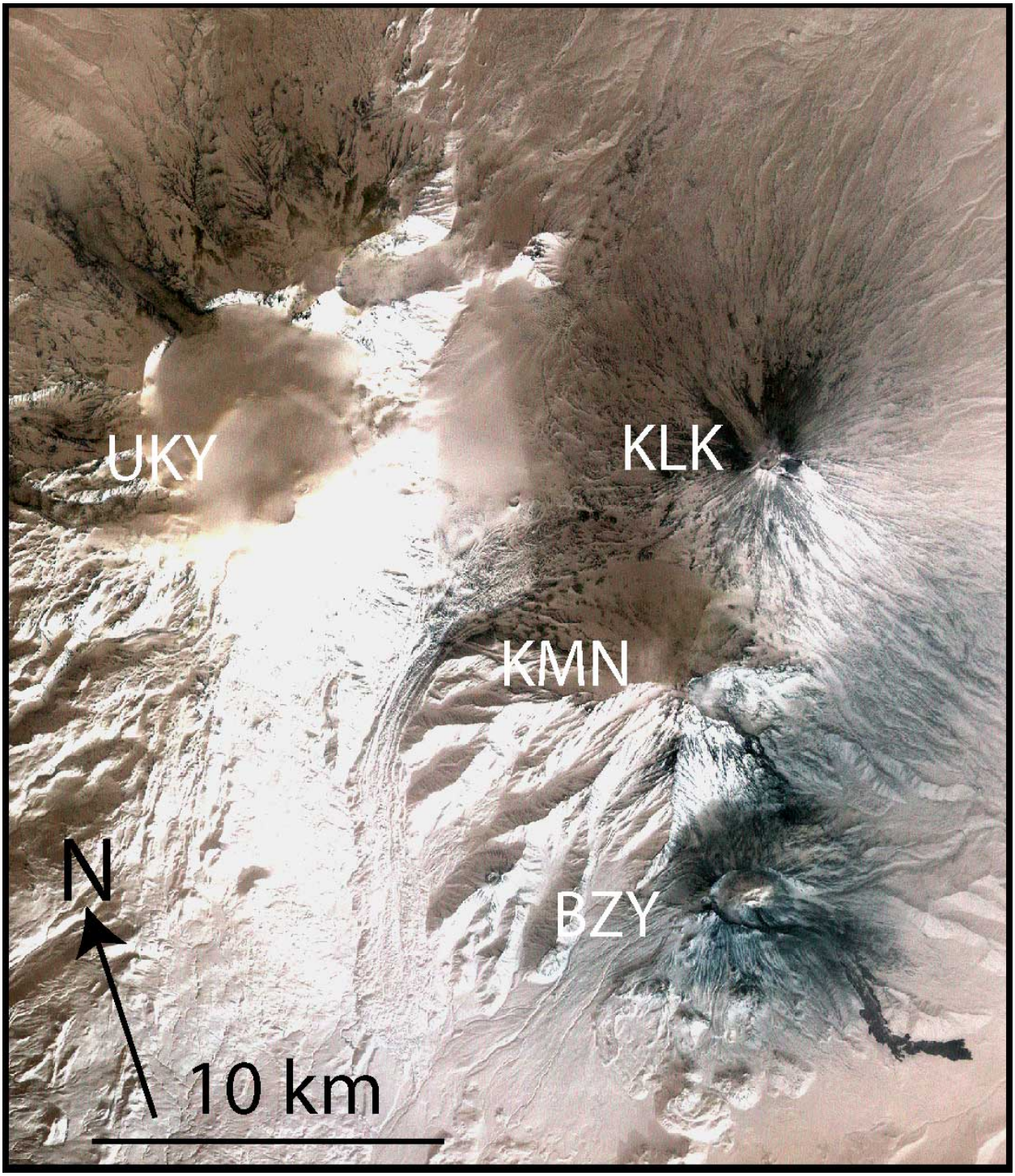

Figure 2 Map of the central Klyuchevskaya Volcanic Group. The volcanoes marked (to the west of each peak) are Bezymianny (BZY), Kamen (KMN), Ushkovsky (UKY) and Klyuchevskoy (KLK). Map based on an ASTER daytime image from 4 January 2007. Bezymianny and Klyuchevskoy are highly active at the time of writing.

Nineteen dacitic domes lying stratigraphically beneath Bezymianny indicate that volcanism has occurred in this area over the last 15-20,000 years before present (B.P. Ozerov et al., 1997). At least four of the domes likely originated from subglacial eruptions (Bogoyavlenskaya et al. 1991). Earliest deposits from the "pre-Bezymianny" Volcano have been dated at 10-11,000 years B.P., at the beginning of the Holocene epoch (Bogoyavlenskaya et al., 1991). This was followed by a 3,000 year hiatus in activity, truncated by the deposition of a tephra layer at 7,000 years B.P. Basaltic andesite and andesite lavas and ash created the modern Bezymianny complex, between 5,000 and 3,000 years ago. During the last 3,000 years there have been three large periods of activity: (1) between 2,400 and 1,700 years ago, (2) between 1,350 and 1000 years ago, and (3) from 1955 to the present day (summarised in Bogoyavlenskaya et al., 1991).

Geochemical analyses indicate that the primary composition of the Bezymianny complex is currently andesitic and dacitic (57-62% SiO_2), with some basaltic andesites (Fedotov et al., 1991). Recent models (*e.g.* Ozerov et al., 1997) suggest that the Bezymianny magma reservoir could be linked to the Klyuchevskoy chamber, known to be most recently producing High Aluminium Basalts (HAB). It has been proposed that the main magma conduit separates into two branches for Klyuchevskoy and Bezymianny at an estimated depth of 30 to 40 km (Ozerov et al., 1997). Geophysical and petrological evidence suggests the Bezymianny magma chamber lies at a depth of around 15 to 20 km (Ozerov et al., 1997).

Prior to 1955, the volcano was considered extinct and was thus termed Bezymianny. Geological analysis demonstrated that the volcano had not erupted for around 1,000 years (Bogoyavlenskaya et al., 1991). The summit region contained a small crater and was approximately 500 m in diameter. The volcano reactivated in 1955, when a total of 1285 pre-eruptive earthquakes occurred between 29 September and 22 October (Bogoyavlenskaya and

Kirsanov, 1981). From 1 January 1956 to 29 March, moderate explosive activity occurred at the summit of Bezymianny (Bogoyavlenskaya and Kirsanov, 1981). During this time severe uplift (ca. 100 m) exposed solid lava at the summit and on the southeast flank of the volcano, considered to be the remains of an older lava dome system (Bogoyavlenskaya and Kirsanov, 1981). This suggested that the system was pressurizing and undergoing juvenile magma injection at relatively shallow depths. On 30 March 1956 a paroxysmal blast occurred, creating a 40 km high ash column that travelled northeast (Gorshkov, 1959). The initial explosion depressurised a partially exposed cryptodome (defined as a lava dome that is emplaced at very shallow levels within the interior of the volcano), sending approximately 0.5 km^3 of volcaniclastic material to the southeast (Gorshkov, 1959; Belousov, 1996). A 1.3 x 2.8 km horseshoe-shaped crater formed (with an approximate volume of 0.74 km^3) opening to the southeast (Fedotov et al., 1991). The deposits moved 22 km to the southeast as a rock slide that developed into a debris avalanche (Belousov and Belousova, 1998).

This was the first documented directed blast (defined as a volcanic explosion of rocks and magma, or both, erupted at a low angle relative to the ground), which later was well-documented during the 18 May 1980 eruption at Mt. St. Helens Volcano (MSH) in the United States. Bezymianny became the diagnostic volcano for this type of eruption following new research into lateral blast eruptions after MSH (Swanson et al., 1987; Anderson and Fink, 1990; Druitt, 1992). At Bezymianny, burnt organic material in the deposit indicated that the debris avalanche was hot. The avalanche fault plane dissected the cryptodome causing instantaneous depressurization and a gas-driven blast that flattened vegetation and ultimately overtook the debris avalanche (Belousov, 1996). The debris avalanche was then redirected to the east upon contact with the base of Mount Zimina (Belousov, 1996).

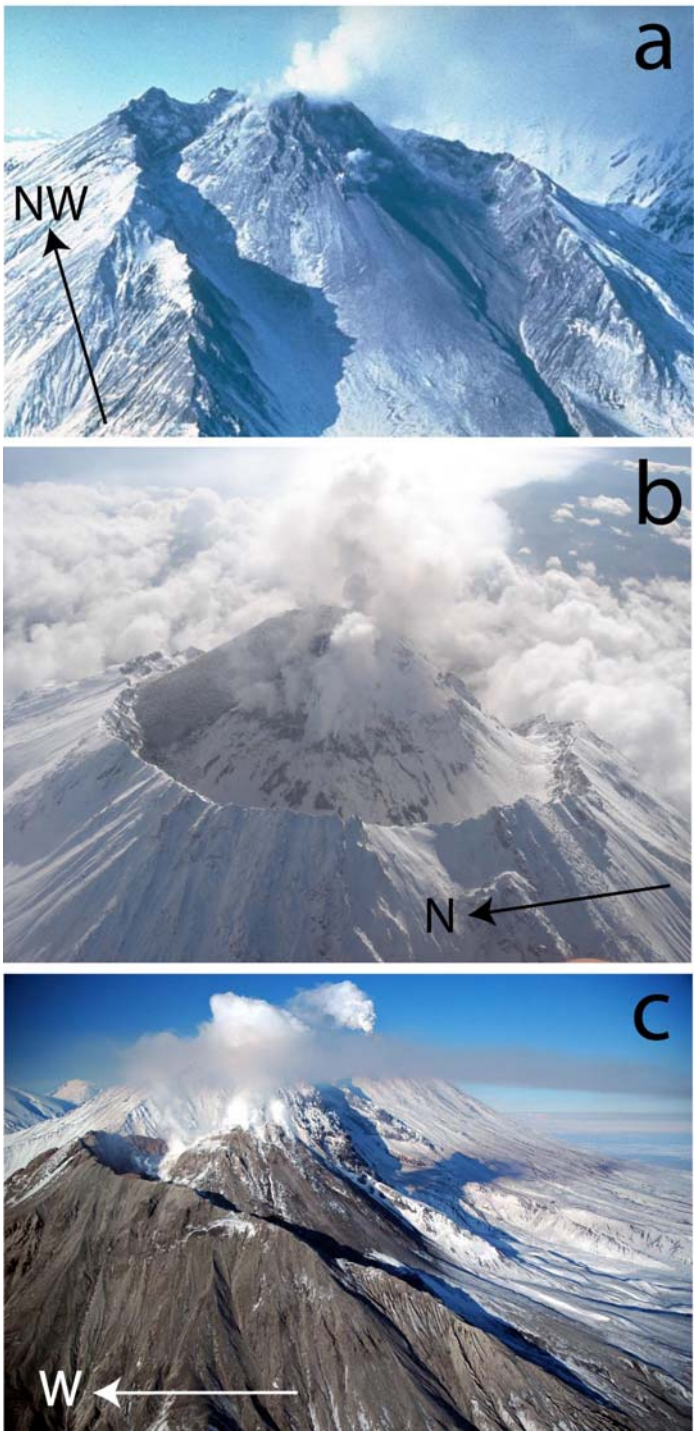

Figure 3 Aerial field images of Bezymianny Volcano. (a) Lava dome photo taken in the late 1980's by Yuri Doubik, KOGS RAS. The 1956 crater can be clearly seen, with the new dome (Novy) growing within the crater. (b) Photograph taken August 2004 facing southeast. (c) KVERT photograph from 5 February 2006. At the time of writing, the lava dome exceeds the height of the 1956 crater rim.

An exogenic dome, named "Novy" (*New* in Russian), has been growing and collapsing in the central crater since 1956. The current phase of activity has included effusion of viscous lava flows that commonly travel for less than 1 km. Ash emitting eruptions, pyroclastic density currents (PDCs) and lahars (defined as volcanic mudflows) also occurred during this time. Activity at the summit of Bezymianny has been concentrated within the central dome region and down to the southeast, forming an inter-bedded sequence of deposits.

Episodes of extrusion of rigid spines and blocky lavas are common at Bezymianny and occurred with considerable frequency between 1969 and 1975 (Bogoyavlenskaya et al., 1991) and more recently during 2005 and 2006. A moderate to large eruption (Volcanic Explosivity Index, VEI = 3) occurred in 1977 and produced a large crater at the summit (Newhall and Self, 1982). This cyclic activity has been recognised by repeated observations since the eruption of 1956. Belousov et al. (2002) suggested that this cyclic activity consists of three stages: (1) an initial stage consisting of the extrusion of low temperature, crystalline spines that may collapse producing rock avalanches. Warmer lava flows typically follow, with the emplacement of short (< 1 km) "lobes" (used from here to describe short, viscous lava flows) on/around the dome summit. (2) An explosive phase follows, which may produce a vertical eruption column, the dispersal of ash several tens to hundreds of kilometres away, and the generation of a pyroclastic flow (PF) on the eastern flank. (3) The creation of a "crater-like depression" on the upper surface of the dome, which may become the origin point for later effusion of viscous lava lobes. Recently, eruptions have occurred two times per year on average, suggesting a significant cyclicity in behaviour in the magmatic system at Bezymianny (Ramsey and Dehn, 2004). The 2000-2007 time period was studied in detail within this thesis.

1.5 LAVA DOME INSTABILITY AND VOLCANIC HAZARDS

Explosive volcanism is typically associated with intermediate (54-62% SiO_2) and acidic/felsic (>63% SiO_2) compositions. Intermediate and felsic composition lavas, due to their higher viscosities and commonly lower eruptive temperatures, tend to produce short lava flows (also termed coulées) and domes, as they effuse from a vent (Blake, 1990). A lava dome is a mound of volcanic rock that forms as lava flows onto the surface and amasses over a vent (Fink and Anderson, 2000). Lava domes and coulees are capable of growing to large volumes (several km^3) with steep fronted lobes (slope angles up to 90º). Such flow fronts are capable of collapse, which can generate PDCs (Francis, 1993). Degassed, crystalline lavas are also capable of blocking the vent, and causing a build up of pressure that can culminate in violent explosions due to trapped, exsolved gases typically dominated by water vapour.

Lava dome growth and collapse has been responsible for several thousand deaths over the last century (Rothery, 1989). For example, in May 1902, ~30,000 people were killed in the eruption of Mt. Pelée, Martinique (Walker and McBroome, 1983). Thus, it is critical to attempt to understand the growth and collapse phases of intermediate/silicic lava domes for effective hazard mitigation. Volcanoes such as Mount Saint Helens (MSH. Swanson et al., 1987; Druitt, 1992), Soufrière Hills Volcano (SHV), Montserrat, West Indies (Calder et al., 2002; Druitt et al., 2002), Colima, Mexico (Bretòn González et al., 2002), and Bezymianny, Russia (*e.g.* Gorshkov, 1959), all contain active lava domes with similar geohazards. Monitoring of active, hazardous volcanoes can be costly, dangerous for visiting scientists to install and maintain monitoring equipment, and highly dependent on seasonal weather conditions. For these reasons, remote sensing data can be invaluable to supplement ground-based data.

Lava domes are prone to collapse due to gravitational instability or an increased internal pressure due to volatiles (*e.g.* Francis, 1993). For example, at SHV, Montserrat, exogenous growth of shear lobes at the dome summit was observed during the 1995 – 1998 activity episode and prompted dome collapse events (Watts et al., 2002). At Mt. Unzen, Japan, endogenous growth of the lava dome was observed from 1993 - 1994, creating pressure ridges and open cracks (Nakada et al., 1995). Thus, several processes may occur at a lava dome that can influence the subsequent deposits that are emplaced.

1.6 NORTH PACIFIC MONITORING SYSTEMS

Volcano monitoring on the Kamchatka Peninsula is conducted by the Kamchatka Volcano Eruption Response Team (KVERT, Kirianov et al., 2002) in Petropavlovsk-Kamchatsky, Russia, in collaboration with the Alaska Volcano Observatory (AVO). KVERT was established in 1993 with the intention of limiting volcanic risk posed to the sparse local population of Kamchatka and to the large volume of air traffic (principally cargo and over 20,000 people per day) that links North America to Asia (Kirianov et al., 2002). Explosive eruptions are capable of injecting ash into the upper atmosphere and through the tropopause (around 12 km at ~60º latitude), where the jet stream winds can rapidly distribute ash/aerosols into air routes as well as the entire circumpolar region, possibly impacting the climate (*e.g.* McCormick et al., 1995). Planes entering concentrated ash clouds are subject to intense abrasion, with re-melting of the ash within the jet engines that can coat components in molten glass and ultimately lead to engine failure (Miller and Casadevall, 2000). In one recorded case in 1989 following the eruption of

Redoubt Volcano all four engines failed on a KLM Boeing 747, although the plane eventually landed safely with no fatalities (Brantley et al., 2004).

Routine monitoring is commonly based solely on seismic observations in the Klyuchevskaya group. However certain seismometers are not permanently functioning and have also recorded multiple events from synchronously erupting volcanoes such as the activity of Bezymianny and Klyuchevskoy in January to February in 1999 and again in 2005. Visual and webcam observations are recorded from the town of Klyuchi 50 km northwest of the group, but changes can be missed due to extensive cloud cover. Thus, some changes in activity do not always reach the international volcanology community.

KVERT releases year-round weekly reports outlining changes in activity in Kamchatka and issues predictions when necessary. Since September 2002 KVERT has received Moderate Resolution Imaging Spectroradiometer (MODIS) images and has the ability to process thermal images on-site. Regular (several times per day) Advanced Very High Resolution Radiometer (AVHRR) images are collected over the Kamchatka, Aleutian, and mainland Alaska area by AVO and sent, when necessary to KVERT representatives. Thus, KVERT and AVO collaborate to collect high temporal, low-spatial resolution spaceborne data to monitor the area. To supplement these data, University of Pittsburgh (UP) co-ordinates the collection of satellite-derived rapid response data to provide high spatial resolution data over targeted areas (see section 2.1.1). Thus, the following project capitalized on available field- and satellite-derived data to provide a detailed case study over Bezymianny Volcano.

1.7 WEATHER CONDITIONS IN KAMCHAKTA

Severely cold weather conditions and snow in the winter limit field work in the Bezymianny region. On the peninsula, weather conditions are typically overcast, with an average winter temperature range of –16 ºC to -35 ºC and a typical summer range of 10 to 20 ºC. Satellite monitoring of this area is challenging due to pervasive cloud cover and rain in the summer and low temperatures and snow cover in the winter which obscure the land surface. Thus, geological interpretation of ground deposits using orbital data is difficult during much of the year. However, in winter, the low atmospheric temperatures also provide a distinct thermal contrast with geothermal and volcanic products, increasing the possibility of detecting changes. Remote sensing data, where available, can therefore be invaluable when interpreting volcanological events and attempting to make predictions as to future events.

1.8 REMOTE SENSING HISTORY AND PRINCIPLES

Remote sensing is the analysis of a target without being in physical contact with the object (*e.g.* Sabins, 1987) and encompasses the collection of electromagnetic (EM) energy at different wavelength regions of the spectrum. Early investigations were carried out by Sir Isaac Newton during the late 17th and early 18th Century, who demonstrated the use of a prism to separate white light into the colours of the rainbow (Newton, 1704). He was strongly criticised for his publishing of *Opticks* (1704) due to his firm belief that light travelled as a corpuscular unit and not as a wave. Young, in a lecture in 1801, went against this notion by using interference patterns to prove that light must have been refracted at the contact between the air and a lens (Sobel

1987). The dark fringes in the patterns were shown to be areas where two troughs were converging to give a low reflection, conversely the light areas were areas where two crests were arriving together. This led to the development of the term wavelength, or the distance between wave crests, and Young correctly measured the wavelength of red light at 0.7 μm (0.00007 cm or 700 nanometers) and violet light at 0.4 μm (0.00004 cm), which set the standards for modern physics (Sobel, 1987). The human eye itself has evolved to be coincident with the peak in solar radiance (0.55 μm) in the visible region (0.4 – 0.7 μm) of the Earth's atmosphere that is relatively clear of atmospheric scattering/absorption. Beyond visible light, the longer wavelength infrared or Thermal Infrared (TIR, "infra" being Latin for below) region (0.7- 100 μm) is less studied (*e.g.* Jensen, 2006). Study of this region began in the 19th Century primarily by Sir William Herschel, a German-born Astronomer. Herschel performed experiments using sunlight passing through a prism in 1800, and discovered that a thermometer placed beyond the visible red region of the prism showed a distinct temperature increase, which led him to suggest the existence of an "invisible" region of light, which he coined "dark heat" or "invisible rays". Today the IR region is used for many applications, and was principally developed by the military in World War I (1914-1918) for night vision.

Research continued on heat and EM interactions, spear-headed by German Physicist Max Planck in the 19th century. He created the term blackbody ("a body whose surface absorbs all radiation incident upon it"). Planck suggested that any two blackbodies will emit the same amount of radiation provided they are heated to the same temperature, and that a blackbody will emit more radiation than any other material at the same temperature (Figure 4). The best blackbody is not a surface (such as a painted mat black surface) but is a small hole into a large cavity (Sobel, 1987).

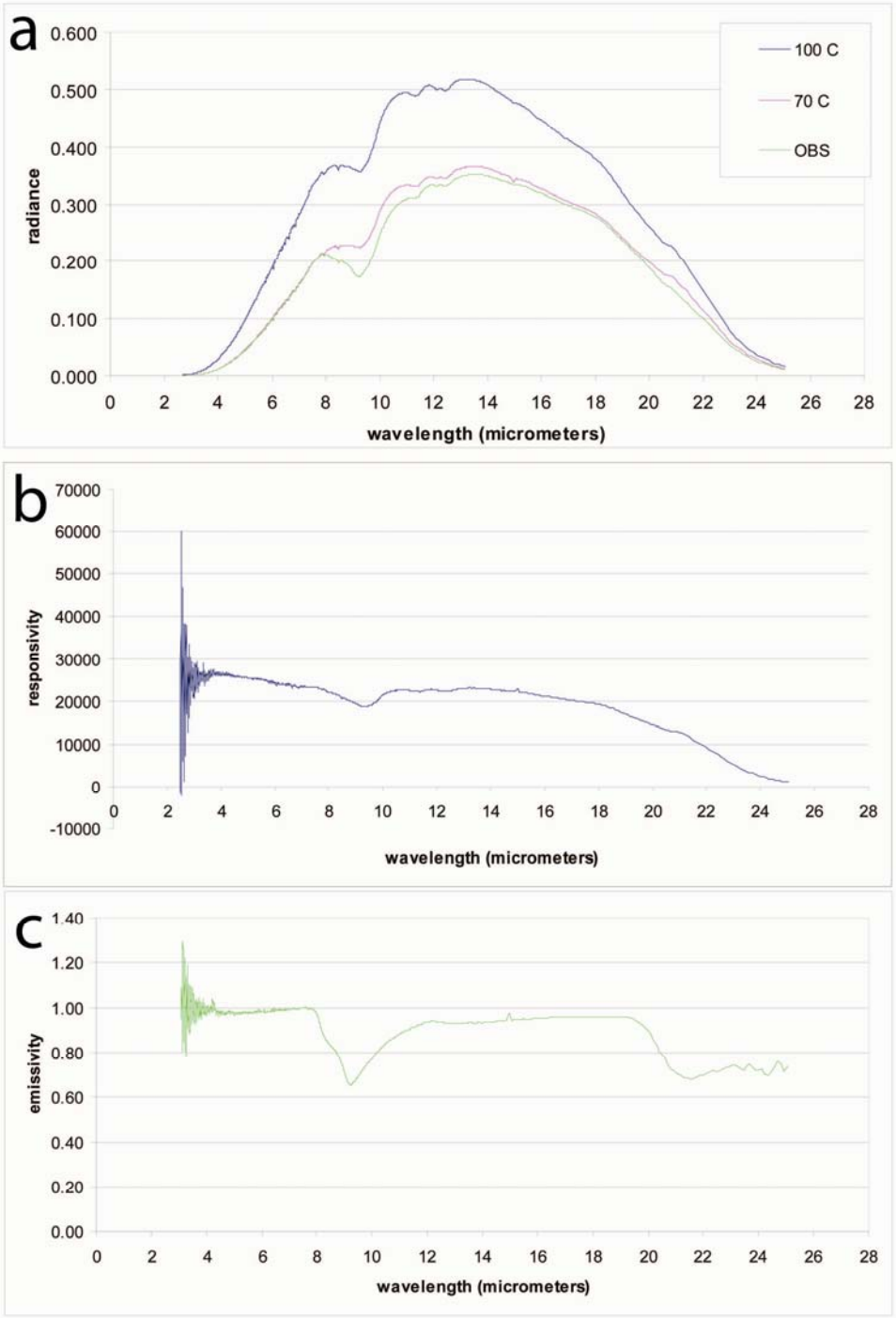

Figure 4 (a) Spectral plots for blackbody curves at 70 °C, and 100 °C, plus an obsidian (OBS). Wien's Law states that the shift of the peak radiance can be seen moving to shorter wavelengths with higher temperatures. (b) Responsivity in V/W/cm^2/sr. (c) Calibrated emissivity spectrum for the OBS sample.

Planck used oscillators to calculate emitted energy and related it to the frequency of oscillation:

$$e = h\nu$$

where e = the elementary unit of energy (the quantum), h = Planck's constant, and ν = frequency in Hz. Planck was also responsible for the law of blackbody radiation, which predicts the spectral intensity of EM radiation at all wavelengths for a blackbody at a given temperature:

$$L_{(\lambda,T)} = \varepsilon_\lambda B_{(\lambda,T)} = \varepsilon_\lambda \left\{ \frac{C_1 \lambda^{-5}}{[\exp(C_2 / \lambda T) - 1]} \right\}$$

where L = thermal energy or radiance, λ = wavelength, B = blackbody radiance, T = temperature, ε = emissivity, $C_1 = 3.74 \times 10^{-16}$ W m^2 and $C_2 = 0.0144$ m K.

Willhelm Wien, during the later 19th Century, showed that the peak emitted energy moved to shorter wavelengths for higher temperature objects. Wien's Law states that there is an inverse relationship between the peak of the emission of a blackbody and its temperature:

$$\lambda_p = 0.2898\, x\, 10^{-3} / T$$

where λ_p = Peak wavelength (m) and T = surface temperature (K).

Much of the basis of remote sensing originates from the early work of James Clerk Maxwell, who included four equations (later termed the 'Maxwell Equations") in his 1873 paper,

A Treatise on Electricity and Magnetism. These equations described the wave-like behaviour that light exhibited (Maxwell 1991, reprinted), and were the basis for Einstein's Theory of Relativity.

Within the last fifty years, physics, engineering, chemistry and geology have all contributed to the creation of the subject of remote sensing. Within this broad field, several sub-groups are defined, a primary group being spectroscopy. Following Lyon (1965), researchers began using thermal infrared spectra in the 8 to 25 micron region for identification of silicates, carbonate, and rock types. It was shown that many igneous rocks can be identified from their spectral emission features (*e.g.* Hamilton and Christensen, 2000). This led to investigations into individual mineralogical spectra and the unmixing or deconvolution of spectra from mixed sources (Adams et al., 1986; Salisbury et al., 1991; Ramsey and Christensen, 1998; Christensen et al., 2000).

An "atmospheric window", an area of minimal absorption/scattering from gases in the Earth's atmosphere (principally, water vapour, carbon dioxide, and ozone) is located from 8-13 μm, where terrestrial sensors concentrate their data collection. Intrinsic properties of silicate minerals (the most common group on Earth) such as the index of refraction (n), absorption coefficient (k), and thus the emissivity (ε) are diagnostic for remote identification. The atmospheric window also corresponds to high k, and relatively low n in silicate minerals, which allows for the detection of the primary absorption band (critical for the identification of a mineral) as well as single photon-particle interaction (critical for identification of mixed surfaces). These physical properties therefore result in the spectra of mixed materials on a surface adding linearly in proportion to their areal abundance (Adams et al., 1986; Salisbury et al., 1991; Ramsey and Christensen, 1998; Christensen et al., 2000).

On 1 April 1960, the Television Infrared Observation Satellite (TIROS) was launched to detect meteorological changes using spaceborne data, and was the World's first weather satellite. This was followed by the Heat Capacity Mapping Mission (HCMM) in 1978 (*e.g.* Ramsey, 2004). More recently, Landsat Thematic Mapper (TM) and the Advanced Very High Resolution Radiometer (AVHRR) have been the only available instruments providing TIR data on a moderate to high spatial resolution. An aerial NASA instrument, Thermal Infrared Multispectral Scanner (TIMS) was used from 1981 to 1996 collecting multispectral data in six bands and was widely considered the precursor to the ASTER instrument.

Within this thesis, remote sensing (satellite, aerial and ground-based, and laboratory-derived) data are used to supplement limited field work in difficult, remote conditions. It also provides data that would be impossible, from a safety perspective, to collect at actively growing, explosive lava domes.

2 DATA SETS AND METHODS

2.1 THE ADVANCED SPACEBORNE THERMAL EMISSION AND REFLECTION RADIOMETER (ASTER)

In December 1999, the *Terra* satellite platform was launched by NASA, as part of the Earth Observing System (EOS) and was intended to improve on moderate resolution land-imaging sensors such as the Landsat Thematic Mapper (Francis et al., 1996). Terra was placed in a near polar orbit at an altitude of 702 km, imaging the land surface with a 60 by 60 km spatial foot print. Five sensors were aboard Terra, including the Advanced Spaceborne Thermal Emission and Reflection Radiometer (ASTER, see Table 2). The ASTER instrument, a Japan-USA collaboration, collects reflected solar and thermally-emitted electromagnetic radiation within three spectral regions: visible near infrared (VNIR) in three bands at 15 m spatial resolution; short-wave infrared (SWIR) in six bands at 30 m spatial resolution; and TIR in five bands at 90 m spatial resolution (Yamaguchi et al., 1998; Abrams, 2000). The nominal repeat time for ASTER data is 16 days at the equator and as low as 5 days at higher latitudes such as the Kamchatka Peninsula due to the off-nadir pointing capability of ASTER and convergence of the orbital tracks.

Table 2 ASTER specification. Spectral range is given in micrometers (µm).
http://www.science.aster.ersdac.or.jp/en/documnts/users_guide/part1/pdf/Part1_4E.pdf

Subsystem	Band No.	Spectral Range (µm)	Spatial Resolution (m)
VNIR	1	0.52-0.60	15
VNIR	2	0.63-0.69	15
VNIR	3N	0.78-0.86	15
VNIR	3B	0.78-0.86	15
SWIR	4	1.60-1.70	30
SWIR	5	2.145-2.185	30
SWIR	6	2.185-2.225	30
SWIR	7	2.235-2.285	30
SWIR	8	2.295-2.365	30
SWIR	9	2.360-2.430	30
TIR	10	8.125-8.475	90
TIR	11	8.475-8.825	90
TIR	12	8.925-9.275	90
TIR	13	10.25-10.95	90
TIR	14	10.95-11.65	90

At the latitude of Bezymianny (55.98º N, 160.59º E), for example, ASTER is able to perform sequential day/night observations which can document thermal changes on the volcano over a 12 hour period. In some cases, ASTER can also collect a night/day/night set of three images with pointing. This information was previously unavailable using other satellite instruments.

2.1.1. Applications of ASTER data in Volcanology

The 14 spectral bands of ASTER have many applications for volcanology, including a low repeat time, high spatial resolution, multispectral thermal infrared bands and Digital Elevation Model (DEM) capabilities from its nadir and backward-looking telescope (Pieri and Abrams, 2004).

The TIR Noise Equivalent Delta Temperature (NEΔT) of 0.3 K at 300 K result in high radiometric accuracy of the extracted surface temperatures (Arai and Tonooka, 2004; Pieri and Abrams, 2004). In addition, the ability to generate 30 m resolution DEMs can be of great value to volcanic hazard mapping for data visualization and modelling. For example, Stevens et al. (2004) compared ASTER DEM data to Shuttle Radar Topography Mission (SRTM) elevation data, concluding that ASTER has enormous potential considering that the SRTM mission was a single collection campaign in 2000, whereas ASTER continues (at the time of writing) to collect data. This provides over eight years of data for three dimensional evaluations. ASTER DEM data are relatively simple to process, whereas multiple corrections are necessary for SRTM data.

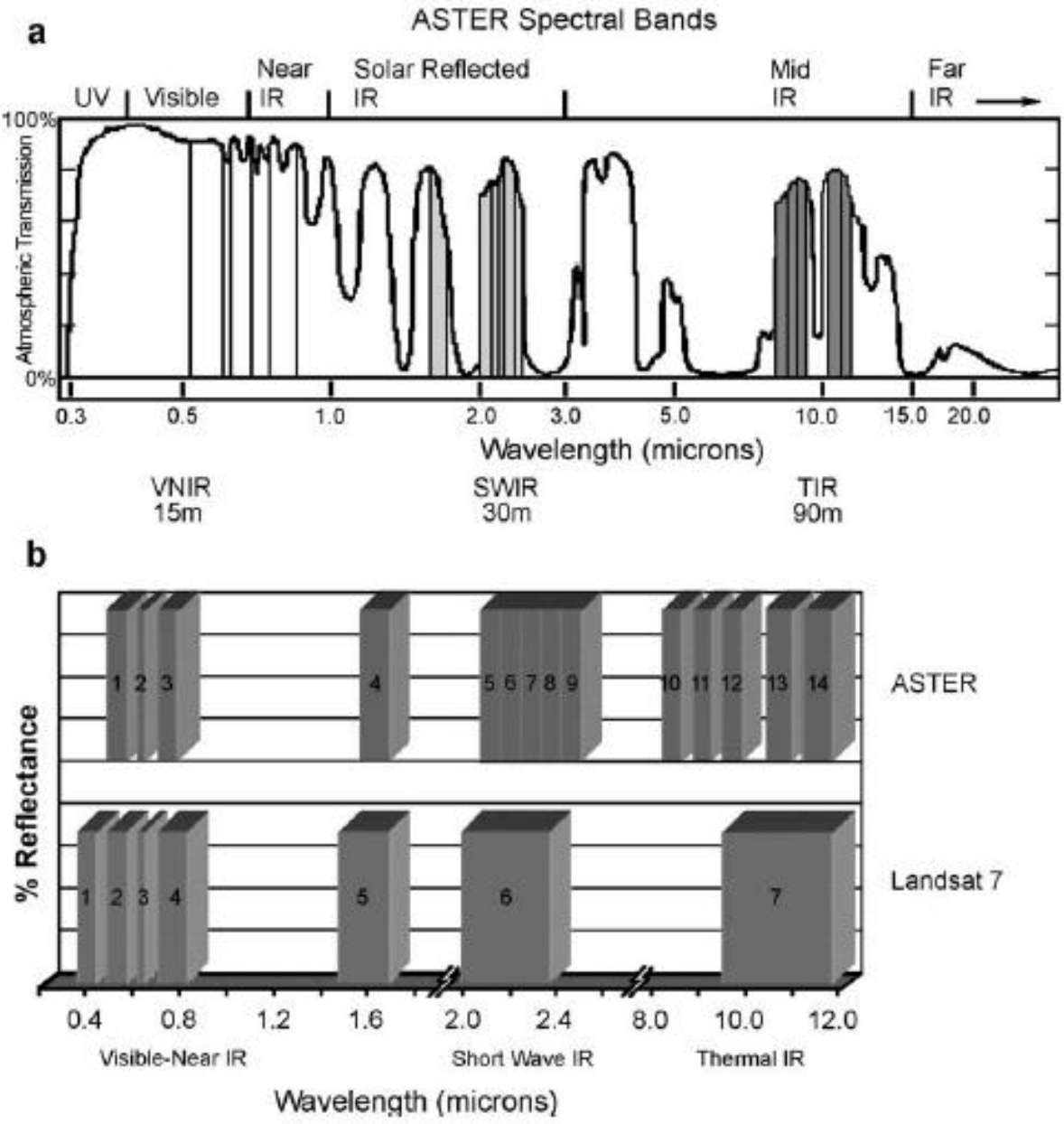

Figure 5 (a) ASTER spectral bands with wavelength. (b) Comparison of ASTER to Landsat 7 spectral bands (Pieri and Abrams, 2004).

ASTER is also now being utilized in rapid response mode, linked to larger-scale monitoring alerts (Ramsey et al., 2004). The first phase of this project is in conjunction with the Alaska Volcano Observatory's current near-real-time volcanic monitoring system that relies on high temporal/low spatial resolution (~6 hours/1 km) orbital data from the AVHRR instrument (Dehn et al., 2000). A thermal anomaly detected by this method triggers an ASTER scheduled observation of that volcano at the next available opportunity. This synergy allows future small-scale activity to be targeted for hazard response and scientific observation. Initial testing of this system in 2005 involved manual triggering of the ASTER response after an eruption is confirmed. This procedure allowed for six cloud-free satellite daytime (VNIR-SWIR-TIR) and 11 night time (SWIR-TIR) images to be acquired from January to September 2005 over Bezymianny, for example. Thus, ASTER provides the opportunity to collect TIR multispectral, high resolution data that can be linked to VNIR reflectance and radiance images several times per month to view frequent changes on active volcanic surfaces (Pieri and Abrams, 2004).

2.1.2. ASTER data products

ASTER data are distributed though the National Aeronautics and Space Administration (NASA) and the Land Process Distributed Active Archive Center (LP DAAC. URL: http://edcdaac.usgs.gov/main.asp, cited March 2007. Appendix A.). This will be changing to the Warehouse Inventory Search Tool (WIST) during late 2008 (URL: http://lpdaac.usgs.gov/news/edg_to_wist_migration.asp, cited July 2008). ASTER data are arranged in a hierarchical data format (HDF), with several derived products available from Level 1-3. ASTER Level 1A data (L1A) is unprocessed radiance at sensor that must be corrected radiometrically and georeferenced to form Level 1B (L1B) data. Level 2 (L2) products such as

AST-09T land-leaving TIR surface radiance have been further processed and atmospherically corrected (*e.g.* Thome et al., 1998). The AST-09T product has an absolute accuracy of 2%. More information is available at http://edcdaac.usgs.gov/aster/ast_09td.asp, cited March 2007). AST-5 emissivity products are corrected for down-welling radiance, which is energy absorbed by the atmosphere and re-emitted at the wavelength being detected by the remote sensing instrument (*e.g.* Ramsey, 2004). This energy would reflect from the surface, which, using Kirchoff's law (R = 1 - ε, where R = reflection and ε = emissivity), would have the effect of increasing the emissivity values, producing a reduction in spectral contrast. Thus, AST-5 products provide more accurate values in terms of spectral contrast and these data were used within this study.

The highest level of processing is on the DEM and ortho-corrected image files (Level 3). These utilize the nadir (3N) and backward-viewing (3B) telescope to produce 30 m resolution relative DEM, which can then be used to correct any geometric distortions in the image data. All ASTER data from L1B to L3 are considered on-demand and processed with the latest calibration coefficients/atmospheric parameters from the L1A archived data at the time of ordering. For this research, L1-L3 data products were used. A full explanation of ASTER data products are available at http://asterweb.jpl.nasa.gov/data_products.asp (cited in February 2007).

2.1.3. ASTER data processing

ASTER products may require further processing when analysing day and night time data. For example, L1B data were radiometrically corrected, but required the use of band scale factors to convert an integer value to a floating point value. For the TIR data, the band scale factors used are located in Appendix B. TIR-derived radiance data were input into ENVI software as an external, Earth Observing System (EOS) file, and converted using the band scale factors. The

radiance at-ground data were then split in to temperature and emissivity using the Emissivity Normalization technique, which has been integrated into a function within the software (Realmuto, 1990). This method is essential due to the Planck equation being under-determined and requires at least one assumption generate a solution.

In 2004 a latitude/longitude correction tool was applied to data (http://asterweb.jpl.nasa.gov/latlon.asp , cited March 2007). This was needed to correct for changes in the Earth's rotation (nutation) since the TERRA launch in 1999, which was causing a positional error of up to 300 m in latitude and a 200 m in longitude. In addition, a compensation for altitude was implemented due to ASTER using the WGS-84 ellipsoid instead of the real surface of the Earth. In areas of great variation in altitude and mountainous regions, the pre-corrected data error was calculated as up to 400 m. Existing data previously ordered from 1999-2004 are corrected via an upload site, and all on-demand data now ordered are automatically corrected.

2.2 FORWARD-LOOKING INFRARED RADIOMETER (FLIR) DATA

2.2.1. Thermal imaging history

Handheld TIR devices have been in development since the early 20th Century, with major advances made by the US military for heat-seeking and night vision technology. Earlier imaging systems required large coolant tanks for liquid nitrogen storage, however this is no longer

necessary due to the advent of uncooled microbolometer detectors, which measure minute changes in heat radiated by an object as changes in resitivity in the detector plane.

Forward Looking Infrared (FLIR) Inc. devices measure broadband radiance from 7.5- 13 μm in the Earth's atmospheric window (Table 3). FLIR cameras are light and portable and can be attached to specialized zoom lenses for imaging at greater distances, making them ideal for volcanological research (URL: http://www.flir.com/US/).

2.2.2. FLIR camera and data specification

A FLIR ThermaCAM^{TM} S40 model was used to collect image and video data within this thesis (Table 3). This instrument has an Instantaneous Field of View (IFOV) of 1.3 mrad, and a detector array of 320 × 240 pixels, thereby producing 76,800 data points per image (FLIR, 2007). The camera has a maximum recordable temperature of up to 1500 ºC using three gain settings to avoid saturation (-40 ºC to 120 ºC, 0ºC to 500 ºC, and 350 ºC to 1500 ºC). The software also allows several input parameters such as emissivity, atmospheric temperature, humidity, and distance to the target to be entered in order to correct for the intervening atmosphere. In addition, a 7º zoom lens was used where larger distances were involved. The FLIR S40 had a thermal sensitivity of 0.08 ºC at 30 ºC, and an overall accuracy of ±2 ºC or ±2% (FLIR, 2007). For high-speed acquisition (up to 60 frames per second), the FLIR was attached directly to a laptop via Firewire or USB2.0 producing large (>1 gigabyte) data files. Post processing was conducted in ThermaCAM^{TM} Researcher Pro software (version 2.8). Images and video were processed and exported as fixed temperature range images used in thermal composites, or ASCII extension files (*e.g.* *.CSV) for import into other programs such as the ENVI image processing software.

2.2.3. Volcanic thermal imaging using FLIR products

Volcano research using FLIR data has drastically increased in the last ten years. A monitoring system that does not require direct contact with the target is highly desirable when studying active, rapidly changing volcanoes. FLIR data are invaluable for volcanological applications such as lava flow thermal output (*e.g.* Harris et al., 2005), ash-emitting explosions (*e.g.* Patrick et al., 2007), rate of magma rise (Ramsey et al., 2005), lava flow emplacement (*e.g.* Lodato et al., 2007), and three dimensional imaging of lava flows (James et al., 2006).

2.3 LABORATORY THERMAL EMISSION SPECTROSCOPY

2.3.1. Thermal infrared spectroscopy

TIR remote observations can be used to provide quantitative, reproducible, non-destructive information on most materials (*e.g.* Clark, 2004). In the laboratory, thermal emission spectra can be collected using highly sensitive Fourier-Transform Infrared (FTIR) spectrometers (King et al., 2004). TIR emitted energy is comprised of the radiant temperature and the wavelength-dependant emissivity of the material (*e.g.* Hapke, 1993; Byrnes et al., 2007). Most of the primary rock-forming minerals have absorption features that lie within the TIR region, which is also coincident with a high transmission atmospheric window on Earth (8-14 μm), making it possible to "see" features in this region (Sabins, 1987).

Table 3 FLIR specification. URL: http://www.flirthermography.com/media/S40_datasheet.pdf

Field of view/ minimum focus distance	24º x 18º / 0.3
Spatial Resolution/IFOV	1.3 mrad
Image Frequency	60 Hz
Thermal sensitivity @ 50/60 Hz	0.08ºC at 30ºC
Detector Type	Focal plane array (FPA)
	uncooled microbolometer
	320x240 pixels
Spectral range (µm)	7.5 to 13

However, there is still atmospheric attenuation and the data from all sensors (especially spaceborne instruments due to their long pathlength) must be corrected accordingly (*e.g.* Thome et al., 1998). A pioneering paper on TIR emission spectra of rock-forming (*e.g.* silicate) rocks was written by Lyon (1965), concluding that the absorption features due to the stretching and bending of silica tetrahedra could be used to produce a "fingerprint" for each unit. Specifically, minerals have a unique spectral signature that can be used to distinguish it from others, providing a method to extract quantitative results from samples (*e.g.* Ramsey and Christensen, 1998).

2.3.2. Data collection

TIR spectra within this thesis were collected at the Image Vizualization and Infrared Spectroscopy (IVIS) laboratory, University of Pittsburgh (Figure 5), and Arizona State University (ASU). At the University of Pittsburgh, a Nicolet Nexus 670 FTIR spectrometer with a potassium bromide (KBr) beamsplitter and a Deuterated Triglycine Sulfate (DTGS) detector was used (allowing data from 5-25 μm). At ASU, a Caesium Iodide (CsI) beamsplitter was used instead and allowed data collection out to 50 μm.

Samples were placed on a heating stage in an atmospherically-controlled glovebox, which was purged of water vapour and carbon dioxide. Further purging could be maintained manually using a separate nitrogen flow. The difference in temperature (ΔT) between the sample and the detector must be large enough to generate an adequate signal. Thus, the sample is heated to 80 °C, or conversely, the detector can be cooled (*e.g.* using liquid nitrogen).

Following the apparatus set up within Ruff et al. (1997), a two-temperature method was used (*i.e.* a blackbody was scanned at 70 ºC and 100 ºC) to derive the instrument response function. This is used to eliminate all energy and instrument effects and produce a calibrated

emissivity spectrum. If an instrument detector temperature change of over 1 ºC occurred then a new set of blackbody spectra were collected and a new instrument response function created (Ruff et al., 1997). The entire process results in a combined error of no more than 2% (Ruff et al., 1997). Following the acquisition of the blackbody spectra, the heated samples are scanned (normally 256 times) to produce an averaged spectrum. Processed spectra are filtered using a standard boxcar filter to minimize random noise.

2.3.3. Data processing

Radiance data were saved as a Comma-Separated Value file (*.CSV) using OMNIC processing software attached to the spectrometer and imported into VM, a spectral processing program developed at ASU. The two blackbody radiance files are used to create the response function (F) of the spectrometer (Figure 4 b), which is then used to create the calibrated emissivity spectrum of each sample (Figure 4 c). Following this, the sample spectra were output in ASCII format (*e.g.* *.TXT file), which could be imported into Microsoft Excel to create spectral plots.

Figure 6 Photograph of the exterior of the spectrometer at the University of Pittsburgh. The main spectrometer (centre) is attached to the glovebox (right) where the samples are stored. Within the glovebox, the housing that contains the sample which is cooled by water to 25 ºC (in red). Internal temperature and glovebox humidity is monitored with a hygrometer (in blue, attached to the spectrometer). The glovebox environment is purged with nitrogen (red cylinders) to reduce noise from water vapour.

2.3.4. Spectral library archives

A library of mineral spectra has been compiled to produce an archive that can be used for further spectral processing (Christensen et al. 2000). Spectral deconvolution relies on the assumption that the spectral features of mineral components add linearly in proportion to their areal abundance. For example, a rock containing 50% mineral A and 50% mineral B would produce a mixed spectrum that represented 50% of minerals A and B (Thomson and Salisbury 1993; Ramsey and Christensen 1998). Subsequently, pixel integrated mixed spectra (*e.g.* ASTER 90 m TIR pixels or laboratory sample spectra) can be collected and further deconvolved to estimate the percentage of each mineral on the ground. This technique can prove valuable where mapping mineral distributions over large areas, or also for planetary applications where ground data is limited and/or impossible. For the data presented in Chapter 6, a two-component deconvolution model was used (obsidian and blackbody) following the work of Ramsey and Fink (1999).

2.4 SCANNING ELECTRON MICROSCOPE (SEM) DATA

2.4.1. Method

Scanning Electron Microscope (SEM) images were collected at Michigan Technological University (MTU) in 2006 and 2008 on a JEOL JSM-6400 instrument. In secondary electron mode, a set of coils concentrates the electron beam and scans the surface row by row. In this method, SEM images of the sample are captured at a separation angle of 6˚, ensuring that magnification and working distance are held constant. The smallest aperture setting on the

instrument (50 μm) is used to create a low convergence angle and the greatest depth of field. Imaging is conducted rapidly to limit sample coating degradation by the electron beam.

A small portion (~ 10 mm by 8 mm) of samples from Bezymianny pyroclastic flow deposit that were used for TIR spectroscopy were subsequently prepared for SEM analysis. These small samples were fixed to aluminium stubs using a wax adhesive and coated with gold using a sputter coater to a thickness of 15 nanometres (nm). Image quality was enhanced through the application of silver paint between the sample and stub to improve the electrical ground. Ash samples were prepared using a dispersion method (O.P. Mills, personal communication, 2006). A small amount of ash was placed in a sealed plastic container, adjacent to an aluminium sample stub; the stub had an electrically conductive sticky coating on its upper surface. Several short bursts of pressurised gas were aimed at the ash sample through an opening in the top of the container, which produced a homogeneous dispersion over the sample stub.

Post-processing software allowed the 3-D characteristics to be measured using a stereo-pair of secondary electron images (*e.g.* Podsiadlo and Stachowiak, 1997). A detailed explanation of the SEM imaging process is available from Goldstein et al. (1981). A DEM was then generated from the images using professional software and the morphology and surface area of the DEM was quantitatively measured to infer surface characteristics of the sample. The number of pixels per line (PPL) in each image was set at 1500, to provide a high resolution without a large processing time. Quality testing using 1000, 1500 and 2000 PPL was performed before deciding on the 1500 PPL value, which resulted in an image size of 1.7 megabytes. Using a magnification between 12× and 3000× the range of horizontal spatial resolutions were 22 micrometers (μm) to 0.009 μm. For each sample a context, low magnification image was used (12×), followed by a series of either moderate/high magnification (200-400×), high

magnification (800×), or very high magnification (1000-3000×). If a stereo pair of images were required, the sample was imaged at 3º from vertical, then rotated 6º, 3º past vertical.

2.5 SUMMARY OF DATA/METHODS USED

The primary goal for this project was to integrate ASTER, FLIR, and laboratory thermal emission spectra with SEM image data to evaluate the thermal and textural differences on the lava dome and deposits of Bezymianny Volcano. In addition, the associated errors, agreements, and differences were considered to test multiple methods of remote sensing and field-based investigations in order to investigate volcanological processes at Bezymianny.

2.6 EXECUTIVE SUMMARY OF CHAPTERS 3 - 6

Chapters 3 – 6 are peer-reviewed papers that have either been published (Chapters 3 and 4) or are, at the time of writing, in review (Chapters 5 and 6). Within this thesis, five abstracts have also been referenced that were presented at professional meetings (Appendix C).

Chapter 3 outlines the use of ASTER and FLIR data around the winter period of 2005 and an explosive eruption that occurred on 11 January 2005 (Carter et al., 2007a). A new summit crater was detected in March 2005 in the ASTER data that was interpreted to be of collapse origin, based on the morphology of the crater. This was strengthened by helicopter-based aerial

photography and FLIR video of the summit region. It was also suggested that the collapse crater may have blocked the upper conduit and eventually lead to a more explosive eruption in the future. This was confirmed when an above-average sized explosive summit eruption occurred in May 2006.

Chapter 4 is a continuation of the use of TIR data, focussing on the events of December 2006 to April 2007, when another explosive eruption occurred at Bezymianny on 24 December 2006 (Carter et al., 2008a). ASTER TIR and SWIR data were used to analyse the eruption and its products, which was difficult to investigate in the field due to winter conditions. From the dataset, a precursory TIR and SWIR signal was detected in data from the 20 December 2006, four days prior to the eruption. Field work was then used to verify the presence of a new PF deposit which was photographed in December 2006 and March 2007.

Chapter 5 presents fourteen months of ASTER data (October 2006 to December 2007) that was used to analyze three eruptions (December 2006, May 2007, and October 2007. Carter and Ramsey, 2008a). Clear peaks in TIR thermal data were noted over the eruption periods. In addition, field work was carried out in August 2007 and a pyroclastic flow from the May 2007 eruption was investigated in detail using ground-based and aerial FLIR data. It was shown that the deposit may have thickened with distance from the vent, as the slope angle decreased, and that hot fumaroles (up to 377 °C) were still detected on the surface, three months after the eruption. ASTER, FLIR and thermocouple data were all used to compare multiple techniques of temperature retrieval. It also provided the first high temporal and spatial resolution dataset over Bezymianny over a one year period to assess eruptive and non-eruptive episodes.

The interaction of EM emitted energy with micron-scale surface roughness (and vesicularity) was studied for PF samples from Bezymianny and is presented in Chapter 6 (Carter

et al. 2008b). SEM images of the samples were used to create DEMs, calculate the average surface roughness (R_a), and derive an image-derived surface vesicularity. A positive correlation was observed between increasing image-derived surface vesicularity and the R_a value of each sample. These results were compared to laboratory TIR emission spectra, which can also be used to extract the surface micron-scale roughness (Ramsey and Fink, 1999). However, the correlation between SEM and TIR data was weaker. This work clearly delineated a cross-comparison methodology and provided a staging point for a future study using more PF samples from Bezymianny.

3 DETECTION OF A NEW SUMMIT CRATER ON BEZYMIANNY VOLCANO LAVA DOME: SATELLITE AND FIELD-BASED THERMAL DATA

3.1 CHAPTER SUMMARY

An explosive eruption occurred at the summit of Bezymianny volcano (Kamchatka Peninsula, Russia) on 11 January 2005 which was initially detected from seismic observations by KVERT. This prompted the acquisition of 17 ASTER satellite images of the volcano over the following 10 months. Visible and infrared data from ASTER revealed significant changes to the morphology of the summit lava dome, later seen with field-based TIR camera surveys in August 2005. The morphology of the summit lava dome was observed to have changed from previous year's observations and historical accounts. In August 2005 the dome contained a new crater and two small lava lobes. Stepped scarps within the new summit crater suggest a partial collapse mechanism of formation, rather than a purely explosive origin. Hot pyroclastic deposits were also observed to have pooled in the moat between the current lava dome and the 1956 crater wall. The visual and thermal data revealed a complex eruption sequence of explosion(s), viscous lava extrusion, and finally the formation of the collapse crater. Based on this sequence, the conduit could have become blocked/pressurized, which could signify the start of a new behavioural phase for the volcano and lead to the potential of larger eruptions in the future.

3.2 INTRODUCTION

Bezymianny (55.98º N, 160.59º E) is a Holocene andesitic composite volcano (Figure 7 a) with a summit elevation of approximately 2,900 m and is located 350 km north of Petropavlovsk-Kamchatsky (Bogoyavlenskaya et al., 1991). It forms part of the Klyuchevskaya group within the central Kamchatka depression. Previously inactive for about one thousand years, Bezymianny reactivated in 1955, culminating in a cataclysmic eruption on 30 March 1956 (Gorshkov, 1959; Belousov, 1996). This directed blast generated a 1.3 km (north-south) by 2.8 km (east-west) horseshoe-shaped crater opening to the east. Following this, a long-term phase of lava dome growth began in the crater, which was mostly endogenous prior to 1969 (Bogoyavlenskaya and Kirsanov, 1981). Similar to activity at Mt. St. Helens (Swanson et al., 1987), lava at Bezymianny was commonly extruded in a near-solidified state as rigid spines in different locations within the crater (Bogoyavlenskaya and Kirsanov, 1981). After 1977, exogenous activity became more common, with lava lobes being emplaced periodically from a single location on the upper part of the dome, adding to its volume (Alidibirov et al., 1990; Bogoyavlenskaya and Kirsanov, 1981). During the last 30 years Bezymianny has been regularly active, erupting one to two times per year on average (Belousov et al., 2002; Ramsey and Dehn, 2004). However, this activity has been punctuated by much larger eruptions such as the sub-Plinian events of 1985 and 1997 (Alidibirov et al., 1990; Belousov et al., 2002) and the recent 9 May 2006 eruption (KVERT, 2006).

The remote location combined with common cloud cover make satellite and field observations of the volcano difficult. However, it remains a critical volcano to monitor due to the

chance of much larger eruptions that can form ash-rich plumes which traverse into north Pacific air traffic routes (Miller and Casadevall, 2000). Similar surveys have also been completed elsewhere at remote or inaccessible volcanoes such as Láscar, Chile (Oppenheimer et al., 1993 and references therein) and Mount Belinda on Montagu Island (Patrick et al. 2005) and required similar verification of results by direct field surveys.

3.3 SATELLITE OBSERVATIONS

The primary satellite instrument used for higher resolution data was ASTER, which acquires reflected solar and thermally-emitted electromagnetic radiation within three spectral regions and at three spatial resolutions (Yamaguchi et al., 1998). However, initial detection of an eruption was made on 11 January by KVERT, which issued a report stating an eruption had occurred at 08:02 am (UTC) and produced an 8-10 km ASL ash column (KVERT, 2005). The eruption was also detected by the AVO AVHRR thermal anomaly detection system (Dehn et al., 2000), which then triggered an ASTER rapid response imaging sequence that involved targeted and regular data collection (Ramsey et al., 2004). This resulted in six daytime and eleven night time images from January to October 2005.

The first ASTER acquisition on 15 January 2005 (described in Carter et al., 2005) revealed night time thermal anomalies around the summit crater as well as up to 3 km away (Figure 7 b). The dome region had a maximum TIR-derived temperature of 26 ºC above the average background temperature (-24 ºC), which was derived from a 20 km^2 non-volcanic area to remove seasonal effects. Three night time scenes (15 January, 16 February, and 4 March 2005) show a cooling trend on the eastern portion of the dome (Figure 7 b). However, PDC deposits

ponded between the 1956 crater wall and dome retained their heat much longer, and continued to show temperatures elevated above background during the field surveys in August 2005. On 12 March 2005, reduced shadowing in the crater and less snow cover allowed for improved viewing conditions of the dome and revealed a distinct circular crater structure at the summit (Figure 7 c). This was the first indication of a new summit pit structure on Bezymianny's dome. An ASTER-derived DEM created from the 12 March images revealed a crater depth of ~50 m and a diameter of 310 m north-south and 385 m east-west. However, the first aerial observations in July 2005 suggested the crater could be up to 200 m deep (O. Girina, personal communication, 2005). The DEM-derived depth was probably an underestimation due to the spatial averaging that occurs at the 30 m resolution of ASTER. Using an inverted, truncated cone as a simplified geometric model, with a large radius of 173.75 m (crater edge) and short radius of 82 m (inner crater base), the volumes calculated for depths of 50 m and 200 m were 2.6 x 1010^{6} m^3 and 10.7 x ^{6} m^3, respectively.

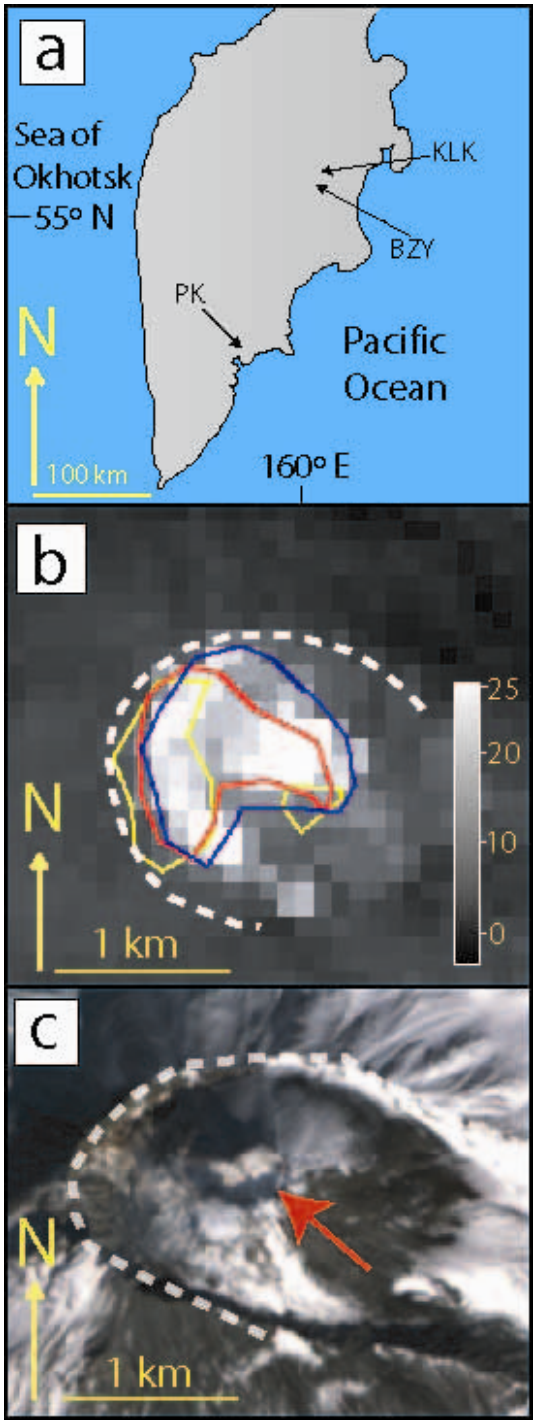

Figure 7 Location and satellite-based observations of Bezymianny Volcano. (a) Map of the Kamchatka Peninsula centred on 55 ºN, 160 ºE, with Bezymianny (BZY) and Klyuchevskoy (KLK) volcanoes located to the north of the city of Petropavlovsk-Kamchatsky (PK). (b) Night time TIR ASTER temperature image in Celsius from 15 January 2005 showing a thermal anomaly around the summit. Overlain: temporal composite overlay of the 10 ºC contour above background temperature for the 15 January (blue), 16 February (red), 4 March (yellow) images. The cooling trend with time over the dome and a sustained anomaly over the deposit within the 1956 crater is evident. (c) Daytime ASTER VNIR image from 12 March 2005 showing the new collapse crater evident on the dome (indicated by a red arrow).

3.4 AERIAL AND GROUND-BASED OBSERVATIONS

Field campaigns in August 2004 and 2005 were performed to verify the recent ASTER observations. During these, aerial high resolution TIR and visible photographic surveys of the dome and pyroclastic deposits were made from a helicopter. In August 2004 no summit crater was present; however, one year later the new summit crater and hot, ponded deposits originally detected with ASTER were verified (Figure 8 a). Thermal surveys were conducted using a FLIR camera. Similar surveys of volcanoes have become a useful monitoring tool in locations such as Stromboli, Italy (Harris et al., 2005) and Mount Saint Helens, USA (Vaughan et al., 2005) for example. The FLIR contains an uncooled microbolometer detector array that captures radiation from the 7.5-13 μm wavelength region. Still images were extracted from video data files taken between 19 and 25 August 2005, which were collected at a minimum of one image per second. A 24º FLIR lens was used, with an instantaneous field of view (IFOV) of 1.3 mrad. Helicopter altitude was around 3500 m and the distance to the upper dome region varied from 600 m to 850 m. Thus, the range of spatial resolutions was 0.78 to 1.11 m. The maximum derived pixel-integrated temperature was 163 ºC, with an average temperature of 10 ºC over the dome area (1.27 km^2). Digital photograph and thermal (FLIR) image mosaics were created and four regions of interests were identified (Figure 8 b and 8 c): 1) a short (60 m long by 150 m wide) lava lobe (Lobe A); 2) a 150 m long lava lobe (Lobe B); 3) the new central summit crater; and 4) two flat-bottomed oval collapse pits 20 by 30 m in diameter in the ponded pyroclastic deposits.

Lobe A flowed to the west and video footage showed that it exhibited partial ductile deformation, sagging back into the crater. Thus, we interpret that Lobe A had not completely

solidified prior to crater formation. The flow surface of Lobe A contained deep ridges perpendicular to flow direction and the FLIR-derived temperature over its area was 10 ºC, with a maximum temperature of 77 ºC. Lobe B was located south of Lobe A, with no apparent cross-cutting relationship to it. The flow surface was visibly smoother and lighter in colour than Lobe A and it had an average temperature of 12 ºC, with a maximum of 56 ºC.

The formation of a central summit crater was the most dramatic change observed at Bezymianny in recent observations. It contained concentric stepped ledges and fractures that surrounded the rim. The crater cut older lava lobes and pyroclastic material as seen in its walls. The warmest areas corresponded to more competent rock layers and hot cracks that bounded the concentric ledges. Surrounding the dome and within the main summit crater of the volcano, the moat was filled with newly-emplaced PDC deposits that contained several collapse pits. The areas within the pits had an average temperature of 33 ºC, with the hottest surfaces at 124 ºC. These collapse structures may be caused by PDC deposition onto (or the entrainment of) ice/snow, which was observed in ice-rich lahars by Branney and Gilbert (1995). At Bezymianny, the thickest part of this new deposit, located west of the dome summit inside the 1956 crater rim, was also the location of the small pits. It is most likely that the PDC deposit was emplaced onto the snow and ice present in this shadowed part of the crater during the January eruption. It cooled slowly over several months while differential melting occurred beneath the deposit, producing the pits (lower Figure 8 b-delimited by a black rectangle) and the thermal TIR anomaly (Figure 7 b).

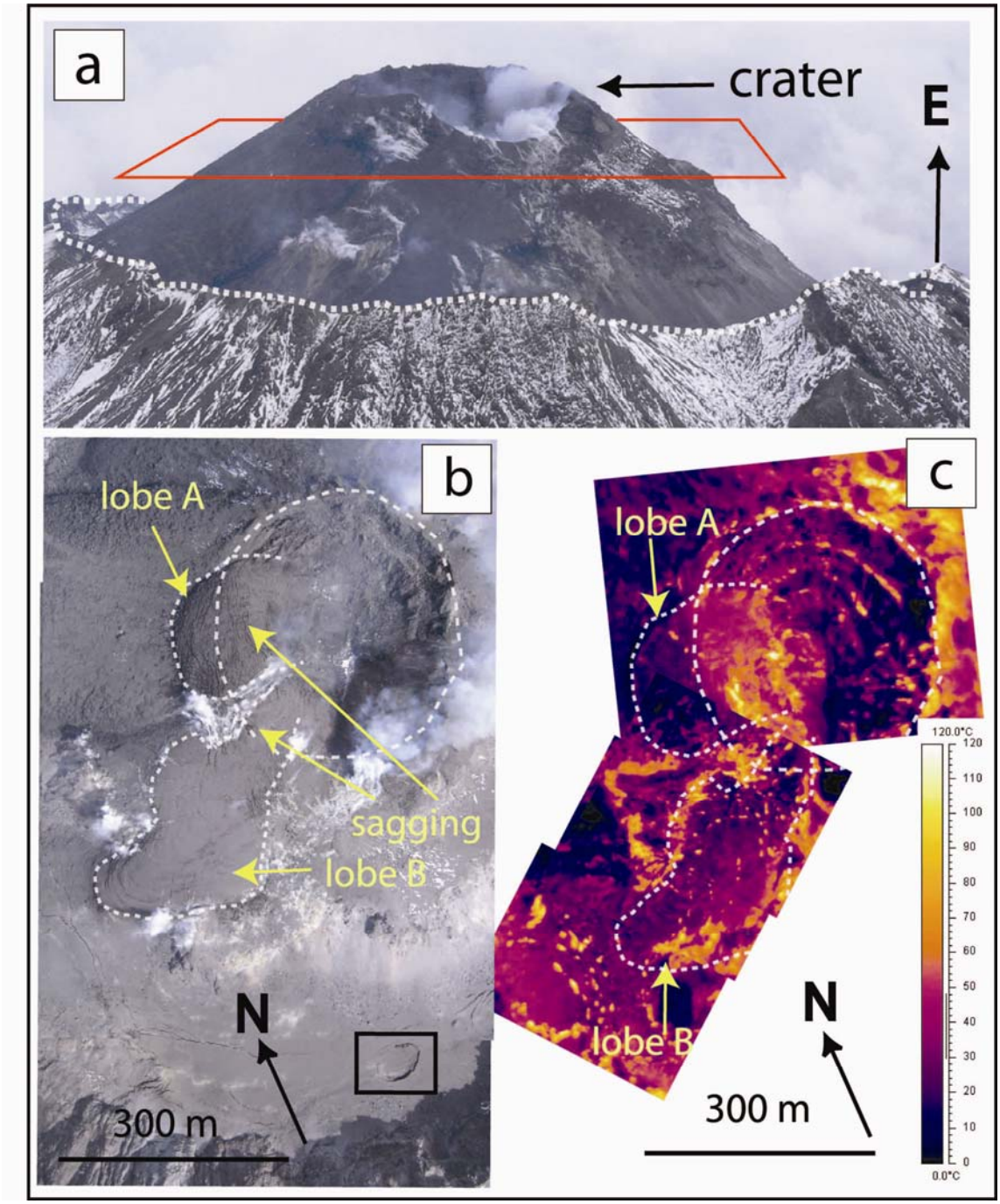

Figure 8 (a) Aerial, digital photograph from 19 August 2005 showing the new summit crater on the lava dome. The 1956 crater (1.3 km north-south) opening to the east is denoted by the white dashed line. The red square delineates the area of study for part b and c. (b) Part of the 19 August 2005 digital photograph composite taken simultaneously with FLIR observations. Lobes A/B and the collapse crater are marked with arrows and dashed lines, with sagging back into the crater marked with arrows. In the lower right (delimited by a black rectangle) one of the oval pits observed within the ponded PDC deposits is shown. (c) FLIR colour composite image with a temperature range from 0 ºC to 120 ºC. The temperatures were derived using an average distance to the dome of 725 m, an assumed emissivity of 0.97 for the surface, a humidity of 30 %, and an atmospheric temperature of 5 ºC. The stepped ledges within the crater can be seen, with both Lobes A and B partially draped into the crater.

3.5 DISCUSSION AND CONCLUSIONS

An explosive eruption occurred at Bezymianny on 11 January 2005 and deposited juvenile and older dome material within the 1956 crater. The eruption also generated one or more PDC deposits, which, based on later field sampling, primarily contained fresh vesicular blocks and ash with smaller quantities of older, hydrothermally altered dome material. Based on the radial deposition observed, the presence of ash on the slopes outside of the 1956 crater, and the column height (8-10 km), we interpret that column collapse most likely formed these deposits. A large fraction of the material pooled between the 1956 crater rim and the dome, with the remainder of this flow continuing down slope to the southeast, carrying hot ash and blocks with unweathered vesicular centres as far as 3 km from the vent.

We infer that the eruption sequence progressed from explosive to extrusive with the emplacement of two short viscous lava lobes (Lobe A and Lobe B) that appear to have erupted from near or at the summit of the existing dome, similar to the previous exogenous dome growth at Bezymianny. Following the flow emplacement, a crater with a volume estimated to be between 2.6 x 10^6 $m^3$and 10.7 x 10^6 m^3 formed within the older lava dome. We cannot infer the exact timing of the crater formation; however, field observations confirmed the lack of a crater in August 2004 and no unusual activity was observed over August-December 2004. Based on field observations and superposition relationships we infer that a collapse at the dome summit occurred following emplacement of these lava flows to form the crater. We propose that the crater is of at least partial collapse origin, based on aerial views of Lobe A that showed a steep cliff on the western rim. In addition, some ductile deformation occurred on the flows as both lobes sagged back into the newly formed crater. This style of deformation further suggests a relatively slow, low-energy collapse process. In addition, the collapse-origin model is supported

by concentric fractures seen in proximity to the crater rim as well as stepped terraces within the crater, which could represent inward-dipping blocks. This crater-forming event was a deviation from recent eruptive behaviour and indicates that the sub-surface conduit structure may have been modified or partially blocked within the lava dome. We hypothesize that if this was the case, it could promote a build-up of pressure, leading to a larger eruption in the future. This was potentially validated by a larger than average eruption on 9 May 2006 that produced a 15 km ASL ash column, which was 5 km higher than most eruptions during the past five years (KVERT 2006). This new phase of activity of Bezymianny may be part of a larger cycle of explosions, dome effusion, and subsidence, as observed at Láscar volcano, Chile (Matthews et al., 1997). This work highlights a possible change in the eruptive behaviour of Bezymianny volcano, which was successfully observed first using the high resolution data from ASTER and later confirmed with detailed ground and airborne observations.

4 ASTER AND FIELD OBSERVATIONS OF THE 24 DECEMBER 2006 ERUPTION OF BEZYMIANNY VOLCANO, RUSSIA

4.1 CHAPTER SUMMARY

An explosive eruption occurred at Bezymianny Volcano (Kamchatka Peninsula, Russia) on 24 December 2006 at 09:17 (UTC). Seismicity increased three weeks prior to the large eruption, which produced a 12-15 km above sea level (ASL) ash column. We present field observations from 27 December 2006 and 2 March 2007, combined with satellite data collected from 8 October 2006 to 11 April 2007 by the ASTER sensor, as part of the instrument's rapid-response program to volcanic eruptions. Pixel integrated brightness temperatures were calculated from both ASTER 90 m/pixel TIR data as well as 30 m/pixel SWIR data. Four days prior to the eruption, the maximum TIR temperature was 45 ºC above the average background temperature (-33 ºC) at the dome, which we interpret was a precursory signal, and had dropped to 8 ºC above background by 18 March 2007. On 20 December 2006, there was also a clear thermal signal in the SWIR data of 128 °C using ASTER Band 7 (2.26 μm). The maximum SWIR temperature was 181 ºC on the lava dome on 4 January 2007, decreasing below the detection limit of the SWIR data by 11 April 2007. On 4 January 2007 a hot linear feature was observed at the dome in

the SWIR data, which produced a maximum temperature of 700 °C for the hot fraction of the pixel using the dual band technique. This suggests that magmatic temperatures were present at the dome at this time, consistent with the emplacement of a new lava lobe following the eruption. The eruption also produced a large, 6.5 km long by up to 425 m wide PF deposit that was channelled into a valley to the south-southeast. The PF deposit cooled over the following three months but remained elevated above the average background temperature. A second field investigation in March 2007 revealed a still warm PF deposit that contained fumaroles. It was also observed that the upper dome morphology had changed in the past year, with a new lava lobe having in-filled the crater that formed following the 9 May 2006 eruption. These data provide further information on effusive and explosive activity at Bezymianny using quantitative remote sensing data and reinforced by field observations to assist in pre-eruption detection as well as post-eruption monitoring.

4.2 INTRODUCTION

Bezymianny volcano (55.98º N, 160.59º E, ~2900 m elevation) is located within the Klyuchevskaya volcanic group on the Kamchatka Peninsula in eastern Russia (Figure 9. Bogoyavlenskaya et al., 1991). It erupted catastrophically in March 1956, collapsing to form a debris avalanche and directed blast deposit, which removed 0.5 km^3 of material (Gorshkov 1959; Bogoyavlenskaya et al., 1985; Braitseva et al., 1991; Belousov, 1996; Belousov et al., 2007). This eruption created a summit crater that opens to the southeast and was the location of effusive

activity that began to form *Novy*, the new summit lava dome (Bogoyavlenskaya et al., 1991). This style of activity, including a large lateral-blast eruption and subsequent crater in-filling by lava dome growth, was later seen following the Mt. Saint Helens 1980 eruption and subsequent activity (Swanson et al., 1987; Anderson and Fink, 1990; Vaughan et al., 2005).

Effusive dome growth at Bezymianny has continued for over fifty years since the formation of Novy, with the lava dome now exceeding the height of the 1956 crater rim (Bogoyavlenskaya et al., 1991). By 1976, the dome had already grown to 0.36 km^3 (Seleznev et al., 1984). Exogenous dome growth by short (< 1 km) lava lobes is now the common style, with new material added to the dome surface. Lobe emplacement has been observed after several explosive eruptions (Belousov et al., 2002; Ramsey and Dehn, 2004; Carter et al., 2007a).

Explosive phases have also been noted at Bezymianny. PF deposits have been concentrated, but not entirely restricted to, the south-eastern flank, channelled by the 1956 crater walls. Explosive eruptions occur one or two times a year on average, a pattern that has been observed over the past two decades (Belousov et al., 2002; Ramsey and Dehn, 2004). The explosive phase commonly lasts several hours to days and is typically preceded by a crystalline spine (plug) that collapses to form rock avalanches (Belousov et al., 2002). The effusion of a lava flow or flows at the dome normally follows this phase several days to months after the explosion(s). PFs typically travel 4 to 7 km from the vent, with one recorded case (1985) of a PF travelling 12.5 km to the southeast (Belousov et al., 2002). In addition, lower bulk density pyroclastic surges have also been observed to travel off the main PF to not more than a few hundred metres away (Belousov et al., 2002).

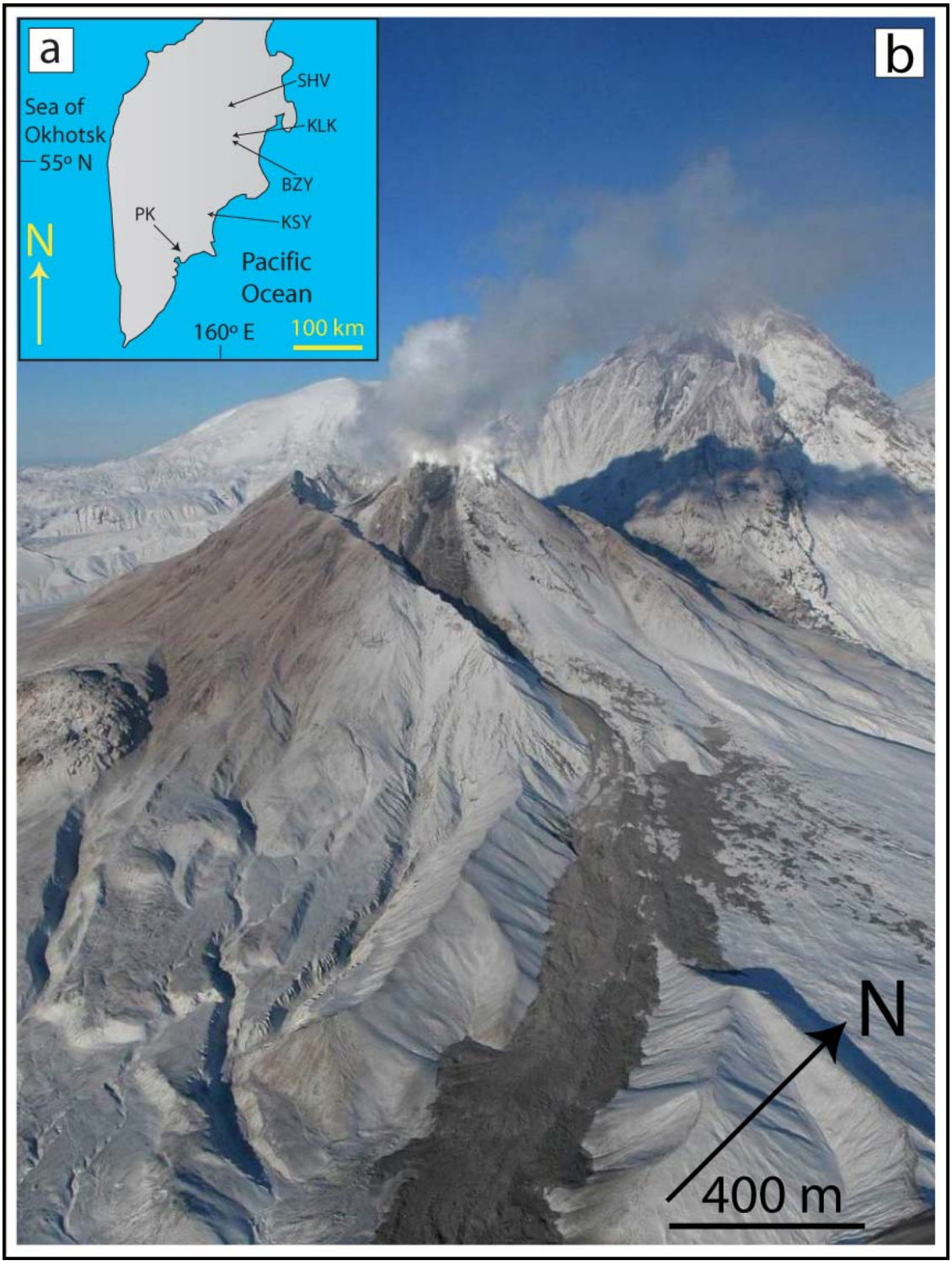

Figure 9 (a) Geographic setting of the Kamchatka Peninsula, North Pacific Ocean. The main city of Petropavlovsk-Kamchatsky (PK) is indicated, as is the location of Sheveluch (SHV), Klyuchevskoy (KLK), Bezymianny (BZY), and Karymsky (KSY) volcanoes. (b) Aerial photograph taken 27 December 2006 looking northwest (Yu. Demyanchuk). Vigorous degassing was occurring at the summit, with dispersed ash observed on the south and west flanks (upper left of the image). In the foreground, part of the fresh pyroclastic flow deposit can be seen.

Monitoring is conducted by KVERT, the Institute of Volcanology and Seismology (IVS) Far East Division, Russian Academy of Sciences (FED RAS), the Kamchatkan Branch (KB) of Geophysical Surveys, Russian Academy of Sciences (GS RAS), and AVO, which is a joint program of the United States Geological Survey (USGS), the Geophysical Institute of the University of Alaska Fairbanks (UAFGI), and the State of Alaska Division of Geological and Geophysical Surveys (ADGGS). In addition, the University of Pittsburgh (UP) assists in observations through orbital data collection of data from the ASTER sensor (Ramsey et al., 2004; Carter et al., 2007a). The eruption described here as well as the recent high level of activity at Klyuchevskoy, Karymsky, and Sheveluch volcanoes demonstrates the need for continuous monitoring and information dissemination to interested groups (*i.e.*, scientists, government agencies, and the aviation industry). This need does not originate from a direct danger to local populations, as there are very few inhabitants living close to the volcano. Rather, it is important for the mitigation of potential threats to aircraft from moderate to occasionally larger ash-emitting eruptions that penetrate the tropopause (~10-12 km above sea level (ASL) at 55º N). Such activity may threaten many trans-Pacific routes of passenger and cargo jet aircraft from the United States to eastern Asia (Miller and Casadevall, 2000).

Bezymianny has been selected as a test target for the ASTER sensor as part of a research investigation by the UP and AVO (Ramsey et al., 2004; Ramsey and Dehn, 2004; Carter et al., 2007a). A previously-developed algorithm by AVO, which automatically processes thermal anomalies from low spatial resolution AVHRR data (Dehn et al., 2000), has been significantly improved allowing the triggering of an automatic urgent-priority ASTER image. These ASTER "rapid response" datasets can commonly be scheduled and acquired within 1 – 5 days, and the

data are available to the research team within 4 hours of acquisition. This system does not have the ability to provide real-time data on an eruption, but does greatly improve the nominal ASTER scheduling/acquisition/processing pathway, which is typically 1-2 weeks long. Once acquired, the higher spatial and spectral resolution ASTER data can be of great value to scientists interested in assessing the post-eruption state of the volcano (*i.e.*, small-scale spatial, temporal, and thermal changes on lava domes and associated deposits). Since January 2000, 12 detected eruptions have coincided with the ASTER monitoring program (KVERT online report 2007). Rapid-response ASTER data have been used to monitor the state of Bezymianny volcano following the March 2000 eruption (Ramsey and Dehn, 2004), and together with limited field studies using a FLIR thermal camera to successfully describe the 11 January 2005 eruption (Carter et al., 2007a). We continue this work by analyzing field and satellite observations from the 24 December 2006 eruption and, in particular, investigate the emplacement of its deposits on the south-eastern flank.

4.3 OBSERVATION CHRONOLOGY AND DATA

4.3.1. Local seismic observations and visual data

The KB GS RAS observed that the seismic precursory phase of the 24 December 2006 explosive eruption began at the end of November, with the amount of near-surface volcanic earthquakes and their amplitudes increased gradually (Girina et al., 2006). From 9 December 2006, a series of low-frequency seismic events were registered almost daily, presumably linked to extrusive

activity or rockfalls. The number of these events increased daily from 5 to 10 to 19 in the three days between 19 December and 21 December (KVERT report, 2006a). This increase in activity caused KVERT to change the colour code from yellow to orange at 20:30 UTC on 23 December. A prediction was issued, based on past experience from seismic evidence that an explosive eruption could occur between 23-31 December, possibly producing an eruption column of up to 15 km ASL (KVERT report, 2006b). According to webcam video data from Kozyrevsk village at a distance of 50 km to the west of Bezymianny, a large hot avalanche occurred at 23:52 UTC on 23 December, associated with an ash cloud that rose to 6 km ASL. At 02:40 UTC on 24 December the colour code for aviation hazards was again increased from orange to red (KVERT report, 2006c). Based on seismic data from the KB GS RAS, a strong explosive event began at 09:17 UTC (21:17 Kamchatka local time) on 24 December (KVERT report, 2006d). This message was sent at 11:10 UTC on 24 December by KVERT to aviation and scientific organizations in north Pacific region. The paroxysmal phase of eruption went on from 09:17 until 10:20 UTC on 24 December, with the volcanic tremor reaching 42.5 μm/s. Visual data from a seismic station located in Kozyrevsk suggested that the eruption column rose to approximately 12-15 km ASL. The eruption reached its peak during the night, therefore the determination of the maximum column altitude was made using visible lightning flashes. On AVHRR and MODIS satellite images collected from 24 to 27 December, the ash cloud was observed to have gradually moved approximately 850 km northeast from the volcano. A report from the associates of F.Y. Lewinson-Lessing Kamchatkan Volcanological Station on 24 December in the town of Klyuchi stated that approximately 1 cm of ash from Bezymianny volcano had settled on the ground (Figure 10 a). In addition, the observers noted that during the ash-fall there was a strong smell of sulphur.

Seismicity dropped to the background level at 22:00 UTC on 24 December, however, from 10:20 to 24:00 UTC on the same day there were approximately 30 (presumably hot) avalanches recorded. This was followed by only two events on 25 December. The colour code was lowered back to orange at 07:30 UTC on 25 December (KVERT report, 2006e) and then to yellow at 22:30 UTC on 28 December. A helicopter-based aerial survey was carried out by members of the KB GS RAS and KVERT on 27 December (Figure 9). It was observed that the southern slope of the dome was partially destroyed and a pyroclastic flow deposit was detected on the south-eastern slope of the volcano.

4.3.2. ASTER data processing

ASTER collects image-based data of reflected and emitted energy in the VNIR region in three wavelength channels (0.56 – 0.81 μm) at 15 m/pixel spatial resolution, in the SWIR region in six wavelength channels (1.65 – 2.40 μm) at 30 m/pixel spatial resolution, and in the TIR region in five wavelength channels (8.29 –11.32 μm) at 90 m/pixel spatial resolution (Yamaguchi et al., 1998).

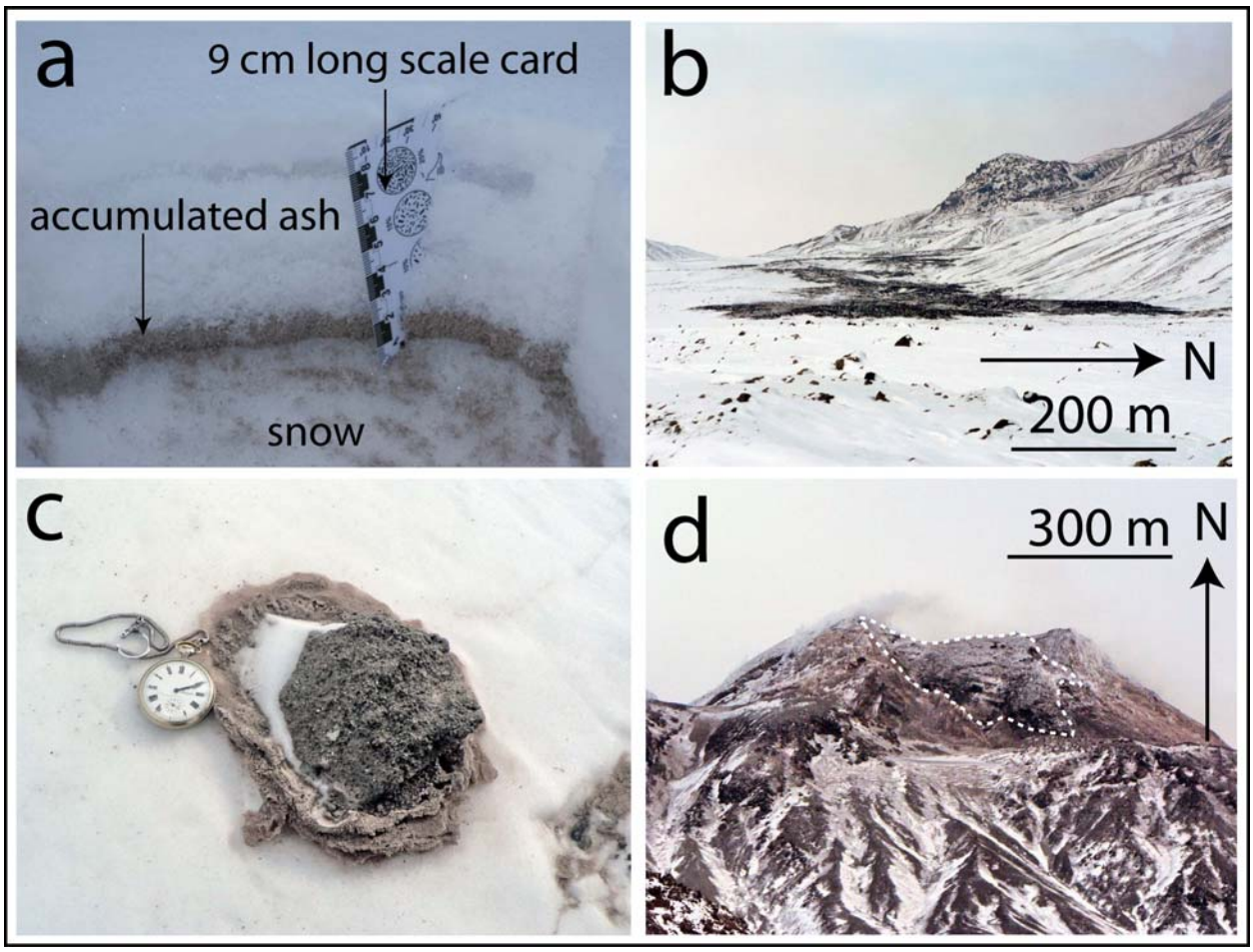

Figure 10 Field photographs. (a) Bezymianny ash deposits at the village of Klyuchi (40 km north-northeast from the volcano). The image was taken on 25 December 2006 with the scale in centimetres (by Yu. Demyanchuk). (b) Pyroclastic flow deposits on 2 March 2007, taken at the PF terminus (by A.V. Sokorenko). On the surface of the deposits, several weak fumaroles were also observed. (c) Photo of a newly-emplaced bread-crust bomb surrounded by an icy crust taken on 2 March 2007, with pocket watch for scale (by A.V. Sokorenko). (d) New lava flow (delineated as a dashed white line) on the summit of Bezymianny taken on 2 March 2007 (by A.V. Sokorenko). The lava lobe continued to fill the southern part of the dome and over-spilled to the south.

These data are processed into various higher level data products that range from geometrically and radiometrically corrected level 1 data (L1B) to level 2 (L2) data, which have been corrected for atmospheric radiance and sensor-specific errors (Abrams, 2000).

For this work, the L2 atmospherically corrected thermal radiance product (AST_09T) was used for the TIR analysis. TIR data have a lower sensitivity to higher surface temperatures where compared to SWIR data and lack the variable gain settings of the SWIR sensor. However, the TIR sensor has a much greater sensitivity to lower temperatures (-73 – 97 ºC) with a 1-2 ºC detection threshold and ±3 K radiometric accuracy (Yamaguchi et al., 1998). Thus the TIR can be used to monitor subtle thermal, compositional, and textural changes over time, especially after the dome and/or deposits have cooled below the detection threshold of the SWIR sensor (*i.e.*, less than approximately 100 °C). Seven ASTER TIR-derived temperature images were used to create a time series of thermal changes at Bezymianny (Table 4). All TIR data were extracted from the L2 radiance product and separated into temperature and emissivity using the emissivity normalization technique (Realmuto, 1990). The average background temperature for each image was calculated from a non-volcanic area of 50 x 50 TIR pixels (~20 km^2) at a similar elevation to the active dome. This value was used to derive the temperature at the volcano above the background.

For volcano studies, an advantage of the SWIR data other than its higher spatial resolution is the much higher detection limit for brightness temperatures, which is a function of the gain setting selected at the time of a scheduling as well as the SWIR wavelength examined. For example, at 2.40 μm (band 9) the detectable brightness temperature range spans from 86 ºC – 329 ºC (high gain versus low gain 2), whereas at 1.65 μm (band 4) the range for the same gain settings increases to 250 ºC – 467 ºC (Urai et al., 1999). This can be useful where distinguishing

volcanic features such as high temperature fumaroles, lava flows, and PF emplacement. For the SWIR analysis, either L1B data (night-time acquisitions) or L2 atmospherically and cross-talk corrected (AST_09XT) data (daytime acquisitions) were used. The higher-level data products for ASTER SWIR were originally derived by the ASTER science team for daytime scenes only and therefore not available for night-time SWIR data. As the sun contributes a small fraction of reflected energy to the surface, it becomes averaged together with the energy emitted from the hot surfaces. Therefore, this solar reflected component was removed for all daytime data prior to extracting the temperature. Similar to the calculation for the average TIR background temperature, the radiance from a ~20 km^2 non-active region of similar albedo, shadowing, and elevation to the dome was selected and the solar reflected component was subtracted from the thermally elevated SWIR pixels. ASTER SWIR data were acquired on four dates from 20 December 2006 to 11 April 2007 (Table 5). The pixel-integrated brightness temperature was extracted from the 2.26 μm band (SWIR band 7) using the reference channel approach (Kahle, 1987). For this approach, a maximum emissivity is assumed and assigned to one wavelength, thus allowing the Planck equation to be solved for the temperature.

4.3.3. Pre-eruption satellite observations

Following the first thermal anomaly detected by the AVHRR sensor, ASTER was scheduled in rapid-response mode to collect data, which it continued to do over the following 3 months (Tables 4, 5). Prior to the eruption, three night-time images were acquired on 8 October, 27 November, and 20 December 2006, with TIR brightness temperatures of 17 °C, 20 °C, and 45 °C, respectively.

Table 4 ASTER TIR data used for this study, with all temperatures shown (in ºC) and derived using ASTER Level 2 AST-09T (TIR) data. TIR-derived background temperature (T_{bg}), maximum dome temperature above background (Dome T_{max}), and maximum PF deposit temperature above background (PF T_{max}) are shown. (*) denotes that on 21 January 2007, clouds partially obscured the dome, generating a lower derived maximum temperature on this date.

Date	ASTER Granule ID	Day/Night	Product	T_{bg}	Dome T_{max}	PF T_{max}
10/8/06	AST_L1A.003:2037597787	night	L2 AST09 T	-12.22	17.28	
11/27/06	AST_L1A.003:2038844472	night	L2 AST09 T	-23.47	19.96	
12/20/06	AST_L1A.003:2039512095	night	L2 AST09 T	-33.76	45.06	
1/4/07	AST_L1A.003:2039800277	day	L2 AST09 T	-33.44	34.62	18.26
1/21/07	AST_L1A.003:2040146335	night	L2 AST09 T	-30.79	2.98*	22.31
2/15/07	AST_L1A.003:2040856230	night	L2 AST09 T	-28.11	25.28	14.91
3/18/07	AST_L1A.003:2041808904	day	L2 AST09 T	-4.22	8.38	15.6

Table 5 ASTER SWIR data used for this study (temperatures in ºC). Two product types were used: Level 2 AST-09XT cross-talk corrected for daytime images and Level 1B data for night time images (where the AST_09XT product was not available). The maximum temperatures (in ºC) were extracted from ASTER Band 7 and recorded at the upper dome region near the summit crater. (*) denotes that on 11 April 2007, the temperature was below the detection threshold of the SWIR sensor at this wavelength.

Date	ASTER granule ID	Day/Night	Product	Dome T_{max}
20-Dec-2006	AST_L1A.003:2039512095	night	Level 1B	128
4-Jan-2007	AST_L1A.003:2039800277	day	Level 2 AST_09XT	181
18-Mar-2007	AST_L1A.003:2041808904	day	Level 2 AST_09XT	180
11-Apr-2007	AST_L1A.003:2042182677	night	Level 1B	*

On 20 December, much of the surface of the dome was thermally-elevated above the background, with 526,500 m^2 (65 pixels) more than 10 ºC, 48,600 m^2 (6 pixels) more than 20 ºC, 32,400 m^2 (4 pixels) more than 30 ºC, and 8100 m^2 (1 pixel) more than 40 ºC. Over the same area, the maximum SWIR-derived brightness temperature was 128 ºC, however the higher spatial resolution of SWIR allowed for much better discrimination and location of the thermal anomalies.

The persistently active degassing and low temperature emission from Bezymianny's dome commonly produces thermally-elevated TIR pixels in ASTER data. However, only during times of eruption with a dramatic temperature increase in the fumaroles and/or the emplacement of new lava flows on the surface of the dome are elevated SWIR radiance values detected. Therefore, we interpret the elevated SWIR temperatures and the rapid increase in TIR temperature on 20 December 2006 to be an indication of precursory high temperature fumarole activity or the extrusion of a lava spine.

4.3.4. Post-eruption satellite observations

The next ASTER scene was a daytime VNIR-SWIR-TIR image, collected on 4 January 2007, 11 days after the eruption (Figures 11, 12). Dispersed fine ash covered the flanks of the volcano discolouring the snow and a steam plume was concentrated over the central dome. A low albedo, narrow feature was noted leading from the central craters down slope on the southeast flank of the dome (Figure 11). This also coincided with the warmest ASTER TIR pixel on that date (35 ºC above background). Twelve ASTER TIR pixels, corresponding to an area of 97,200 m^2, were more than 10 ºC above background in this area.

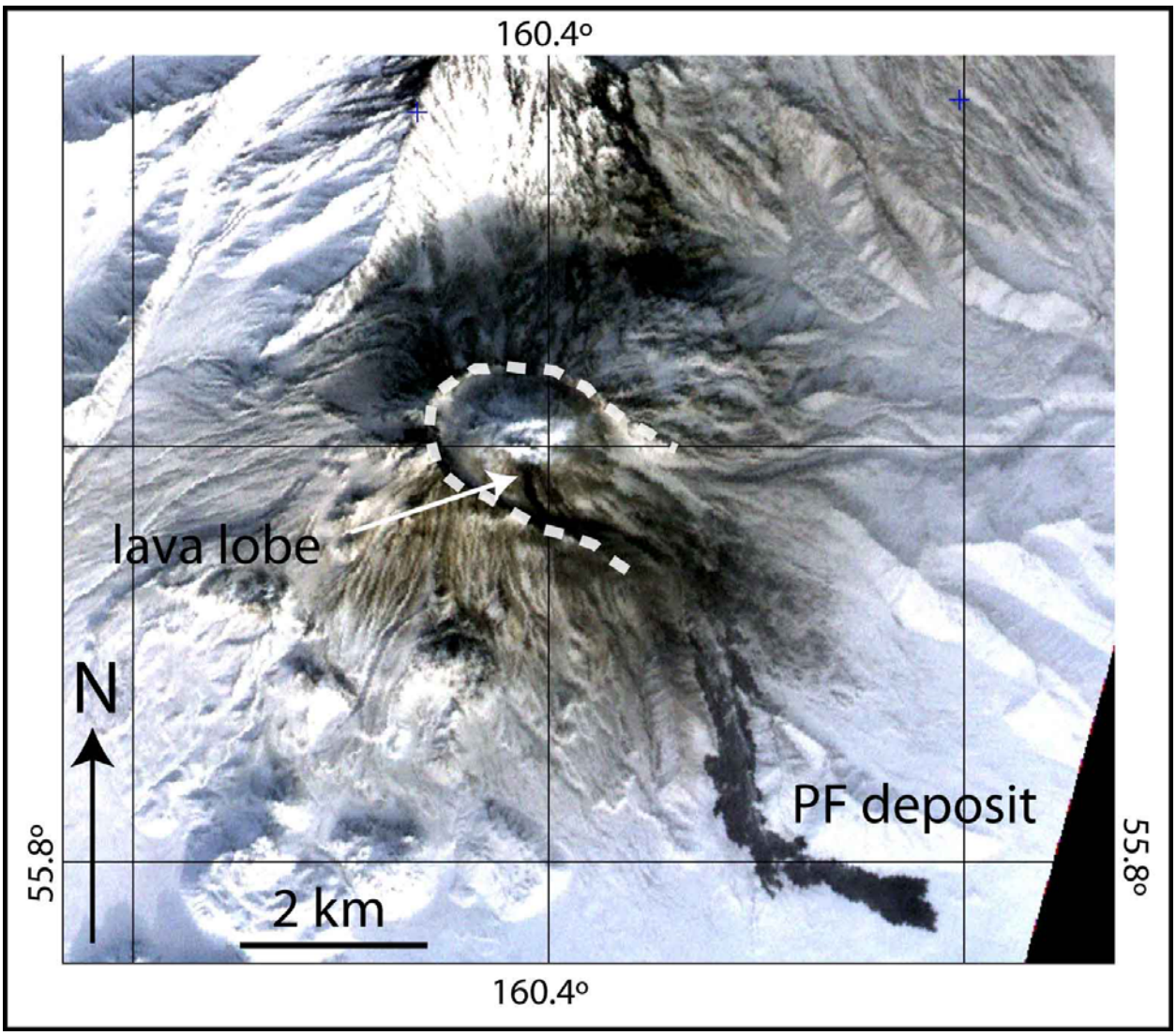

Figure 11 ASTER VNIR image of Bezymianny from 4 January 2007. Coordinates are given in latitude/longitude. The 1956 crater is highlighted with a white dashed line. At the dome summit a dark, linear feature was observed on the upper part of the southeast face of the dome. In addition, the 6.5 km long fresh pyroclastic flow can be seen to the southeast of the summit in a connecting valley.

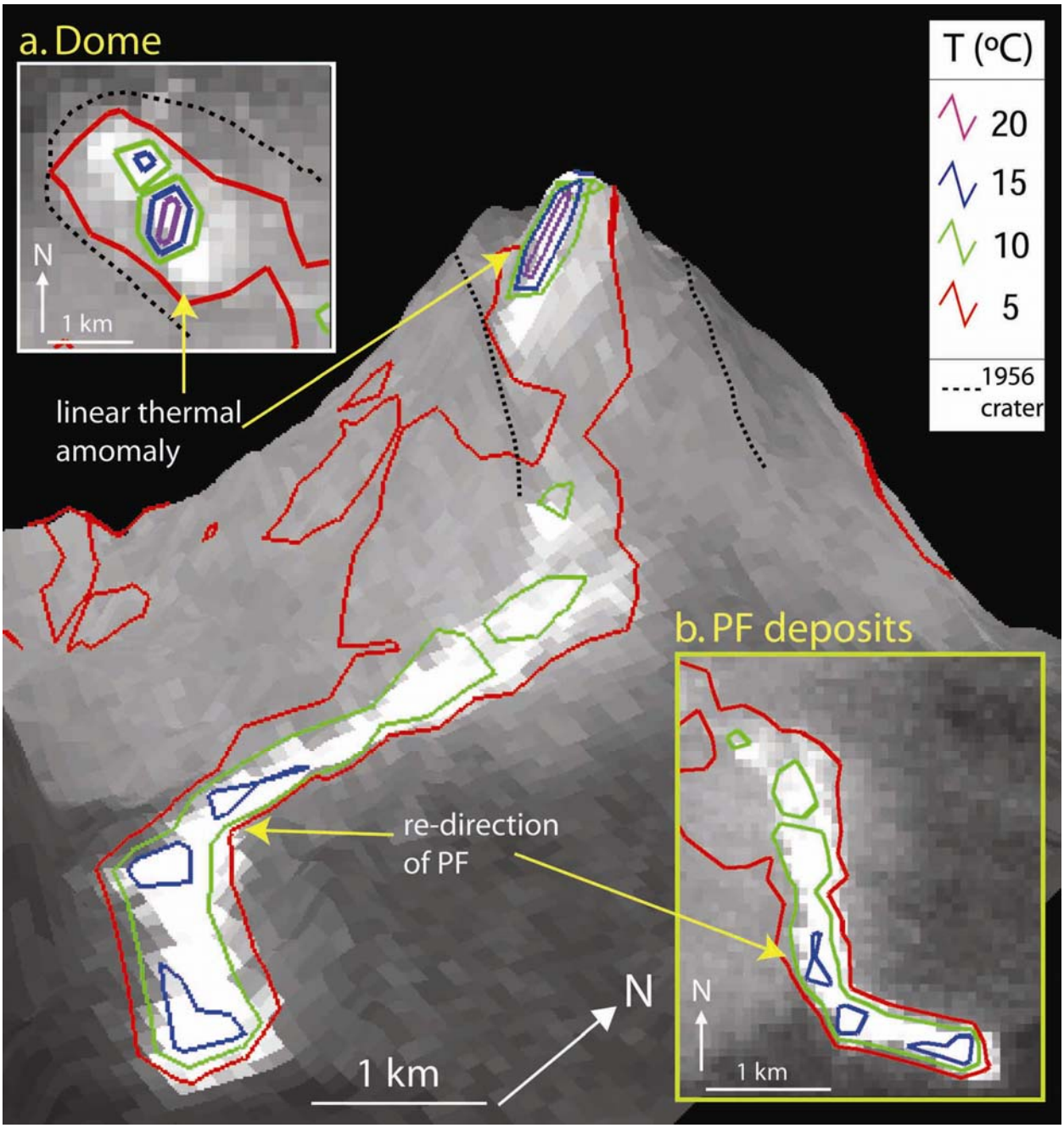

Figure 12 ASTER TIR data from 4 January 2007 draped on an ASTER-derived Digital Elevation Model (DEM) from 18 March 2007 with 3× vertical exaggeration. Temperature contours are ºC above background. (a) Dome region in plan view showing a SE-NW trending warm region extending from the centre of the dome, which is the location of the new lava lobe. Maximum SWIR-derived temperatures were 181 ºC in this area on the same date. (b) Main deposit region in plan-view showing warmest regions in the area where the deposit was redirected to the east-southeast and the deposit terminus (blue contours).

Also observed in the ASTER VNIR data was a large low-albedo PF deposit approximately 6.5 km in length and up to 425 m in width, which travelled from the south portion of the dome and into the south-southeast branching valley. The PF deposit filled the width of the upper valley and contained several lobes that diverged from the main flow. At a distance of 5 km from the vent, the flow was redirected approximately 90º to the east-southeast (Figure 12). The total PF deposit areas that were 10 ºC and 15 ºC above the TIR background temperature were 2.04 km^2 and 0.17 km^2, respectively. The maximum recorded surface temperature above background was 18 ºC, located at the terminus of the deposit and 15 ºC above background where the PF was redirected from the south to the east-southeast. However, all areas of the PF that were greater than 15 ºC above background were found over 4.5 km from the central dome region.

TIR emissivity spectra of the deposit had a noted negative slope at wavelengths longer than 10 μm (bands 13 and 14), suggesting that sub-pixel temperature mixing is occurring within the 90 m pixels (Ramsey and Kuhn, 2004). This may be due to multiple surface components such as surface snow, fine ash, and larger blocks all radiating at different temperatures. The night-time image from 21 January 2007 contained a very weak thermal anomaly on the dome, possibly due to clouds obscuring the surface. However, the entire newly-emplaced PF deposit remained elevated approximately 10 ºC above background, with the warmest being 22 ºC (above a background of -31 ºC). This pixel was located within the central part of the deposit where the flow became redirected towards the east-southeast (Figure 12). After emplacement of the PF deposit, the maximum recorded temperature increased slightly from 18 ºC to 22 ºC between 4 January and 21 January. This minor change is close to the accuracy of the TIR data and could be due to either incomplete atmospheric correction, for

example, or increased emitted heat from large buried blocks with higher thermal inertia values. Following this, the maximum PF temperature stabilised at 15 ºC above background during February and March. During the study period, the background temperature increased from -33 ºC to -4 ºC due to seasonal effects. However, between 15 February and 18 March, the temperature above background for the deposit remained stable. This suggests that the deposit cooled as the background temperature increased from -28 ºC to -4 ºC. During the entire study period, no SWIR thermal anomalies were recorded over the PF deposit region, suggesting that surface temperatures had cooled to below the detectable range for the SWIR.

4.3.5. Time series of ASTER-derived temperatures

TIR data of the lava dome showed a gradual reduction in the maximum temperature above background from 45 ºC to 8 ºC over the December 2006-March 2007 time period (Figure 13, Table 4). However, the SWIR-derived temperature increased from 128 °C on 20 December 2006 to 181 °C on 4 January 2007 (Figure 13, Table 4). This likely indicates either an increase in the thermal flux from fumaroles and/or the presence of high temperature cracks in the newly extruded lobe on the dome. By 11 April 2007, the SWIR temperature decreased to below the detection limit, indicating that surface magmatic activity had also decreased at this time.

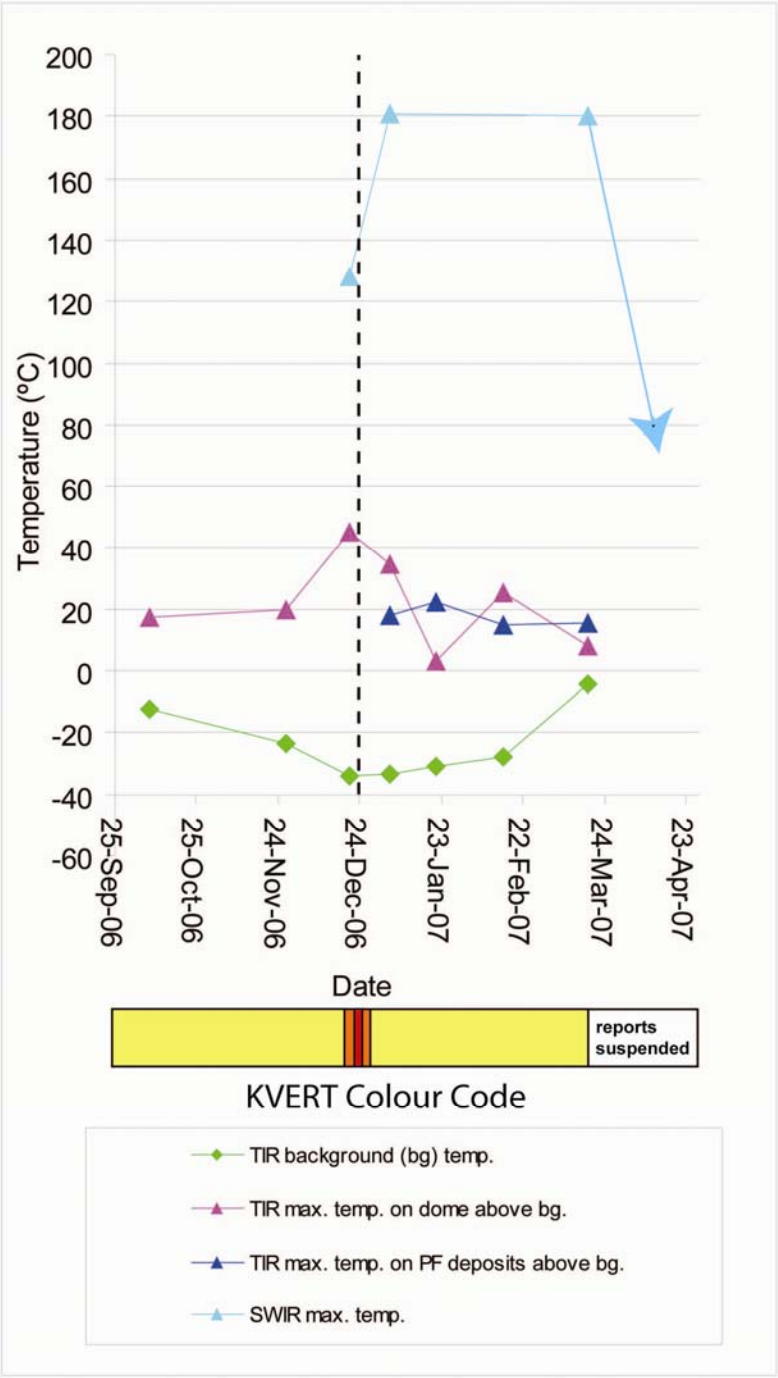

Figure 13 ASTER-derived TIR temperatures (T) in °C for the average background (green), the maximum temperature on the lava dome (pink), and the maximum temperature on the PF deposit (blue) shown from 20 December 2006 to 18 March 2007 (displayed as day/month/year). The start of the eruption on 24 December 2006 (marked as a dashed vertical line) is indicated. SWIR temperatures are also shown from 20 December 2006 to 11 April 2007 (turquoise). KVERT colour codes are displayed below the graph.

One disadvantage of using only the maximum temperature in a remote sensing data set to describe the volcanic activity is that the areal influence of warm pixels is ignored. For example, on 20 December 2006 several thermally elevated SWIR pixels were within the spatial footprint of one thermally-elevated TIR pixel. Therefore, direct comparison of ASTER TIR and SWIR temperatures is challenging and requires modelling of thermal data to estimate the warm fraction of the pixel that may be producing the thermal signal.

The hottest 30 m SWIR pixel on the dome on 4 January 2007 was subjected to the dual band method of sub-pixel temperature extraction (Dozier, 1981; Matson and Dozer, 1981; Rothery et al., 1988; Harris et al., 1997; Ramsey and Dehn, 2004). This simple methodology assumes that for the thermally-elevated pixel there are two radiant temperatures present at the surface: a cooler background and a warmer volcanic temperature (*e.g.* lava flow, PF deposits, or gas/steam, for example). Also assumed is a linear relationship between the ratio of hot to cool fractions of the pixel and the ratio of the hot and cold components of the total radiance. If an assumption is made for the emissivity of the pixel's surface at two wavelengths, then there will remain three unknowns: the hot and cold temperatures and the areal fraction of hot temperature. With two equations and three unknowns, a further assumption (*e.g.*, the temperature of the hot fraction or the area of the hot fraction) is made and the remaining unknowns can be solved.

Using corrected SWIR radiance values at 1.656 μm and 2.4 μm (bands 4 and 9, respectively) and an assumed background temperature of 0 °C, the mathematically-feasible temperature range for the hot fraction can be solved. The high accuracy of the SWIR data leads to the possibility of detection for an area as small as 0.001 % (~1 m^2) of the 30 m pixel. This assumption produces a range of temperatures from 300 to 700 °C for the hot fraction. If this hot fraction is increased to 0.011% (10 m^2), the range of hot temperatures is decreased (180 °C to

500 °C). Based on the range of plausible temperatures and direct field-based FLIR observations of the lava lobes at the dome in 2004 and 2005, it is unlikely that fumarolic activity was responsible for the SWIR anomalies on the 4 January 2007. Surface lava temperatures were most likely responsible, which is consistent with a short lobe being emplaced at the summit. Clearly, the two temperature model is simplified as demonstrated by Wright and Flynn (2003). A multiple component (up to the number of ASTER SWIR bands) calculation could also be carried out to further refine the number and temperature of several different thermal anomalies. However, this level of detail is beyond the scope of this study, which sought only to discriminate between high temperature fumarolic activity and lava on the surface.

4.3.6. March 2007 field observations

IVS FED and KB GS RAS scientists revisited the volcano on 2-3 March 2007 and observed that the PF deposits were almost snow-free (Figure 10 b). On the surface of the deposits, a few weak fumaroles were also observed. Fresh volcanic bread-crust bombs surrounded by an icy crust were found approximately 2.5 km from the pass separating Bezymianny and Kamen (Figure 10 c). This ice rind was formed as the hot bombs fell on snow, causing rapid melting and refreezing. It was also observed that the central dome craters initially formed on 9 May 2006 were now filled with lava. The lava lobe continued to fill the southern part of the dome and over-spilled to the south (see Figure 10 d).

4.4 DISCUSSION

The derived above background brightness temperatures for the dome of 45 ºC and 128 ºC (TIR and SWIR, respectively), relative to lower temperatures observed in October and November 2006, clearly indicate that activity was considerably elevated on 20 December 2006. High temperatures were present at the dome surface four days prior to the eruption, possibly due to vigorous degassing, or the emplacement of a lava spine (Belousov et al., 2002). On 4 January 2007, 11 days after the eruption, a thermally-elevated SWIR region was observed at the dome. Based on modelling using the dual band technique, we demonstrate how this may have been caused by a small fraction of the pixel emitting at magmatic temperatures. Visual observations at Bezymianny on 2 March 2007 by IVS/KB GS RAS scientists later confirmed the presence of a viscous lava lobe emplaced on the southern portion of the upper dome in the location of the thermally-elevated SWIR pixel (Figure 10 d).

A PF was concentrated within the south-southeast branching valley and emplaced over fresh snow to produce a distinct colour contrast (Figure 11). Lower temperatures of the deposit were recorded near to the dome where the high slopes prevented the accumulation of material, relative to the area lower down to the southeast. The thickest deposits occurred on the lower, less steep slopes. Two areas of interest were identified using satellite and ground-based data: 1) the region where the PF was redirected to the east-southeast; and 2) the terminus of the flow deposit (Figure 12). Data from 4 January 2007 showed the first area was warmer on average (15 ºC above background) than the rest of the deposit (See Figure 12 b). If a levee was formed where the flow changed direction and decelerated, the larger and denser blocks would have been deposited. These blocks would likely retain heat longer due to their higher thermal inertia. The granular flow would also likely form a thicker terminus on the lower slopes (~ 4.5 km from the

central dome), which would also retain heat longer. Later field observations confirmed the terminus was ~ 1.5 m thick and contained a higher concentration of blocks. Furthermore, the pixel temperatures of this region remained elevated for 2-3 months after the eruption. The pixel directly down slope of the terminus remained at the background temperature, which implies the flow did not spread diffusely as it came to rest, further validating that the deposit was a thicker, coherent block and ash flow-type PF rather than a pyroclastic surge.

4.5 CONCLUSIONS

Based on seismic and field-based observations, an explosive eruption occurred at Bezymianny from 09:17 until 10:20 UTC on 24 December (21:17 to 22:20 local time), generating an ash cloud estimated to be 12-15 km in height. Four days prior to the eruption a distinct increase in TIR temperatures was noted in combination with a signal from SWIR data, indicating higher temperatures at the dome. We interpret that this provided a precursory signal prior to the large eruption.

Following the eruption, modelling of SWIR data from 4 January 2007 showed that a small fraction (~1m^2) of a SWIR pixel on the dome could have contained temperatures ranging from 300 °C to 700 °C. Even if the area was as large as 10 m^2, the hot fraction would range from 180 °C to 500 °C, suggesting the thermal activity was caused by hot cracks in a lava lobe surface and not fumaroles. Field observations in March 2007 confirmed the presence of the still-warm PF deposit and a new summit lava lobe that in-filled the 9 May 2006 crater, in accordance with ASTER observations. A large, 6.5 km long PF deposit was emplaced on the southeast flank of

the volcano, concentrated in the south-southeast branching valley, and remained at elevated temperatures for over 4 months. The warmest areas on the deposit corresponded to regions where a block-rich natural levee occurred during a change in flow direction as well as at the terminus, which was thicker than the main body of the deposit. This was caused by an increased concentration of blocks with higher thermal inertia values, thereby keeping the temperatures elevated. These observations were derived using ASTER SWIR and TIR products and later confirmed by field observations.

ASTER day- and night-time observations were used to supplement local monitoring data. The December 2006 eruption occurred in a remote location of Russia at -30 ºC and in near-total darkness, negating the possibility of visual observations until after the deposit was formed. To compliment this data set, a thermal infrared study using FLIR data was carried out in August 2007 and will be incorporated in to future work to calibrate derived temperatures with spaceborne data over the dome and particularly the warm PF deposits. Presently, ASTER is the only high spatial resolution, multispectral TIR imaging system available for this style of detailed thermal volcanic studies and monitoring and is adding to a global volcanic archive of thermal data for similar future studies.

5 14 MONTHS OF ASTER- AND FIELD-BASED OBSERVATIONS AT BEZYMIANNY VOLCANO: FOCUS ON THE 11 MAY 2007 PYROCLASTIC FLOW DEPOSIT

5.1 CHAPTER SUMMARY

Bezymianny (Kamchatka Peninsula, Russia) is an active stratovolcano, characterised by a summit lava dome and overlapping PF deposits to the southeast. Three explosive eruptions (24 December 2006, 11 May 2007, and 14 October 2007) and a collapse event (5 November 2007) generated pyroclastic flows and dome activity in each case. High spatial resolution data from the ASTER instrument was collected between October 2006 and December 2007 to assist in post-eruption monitoring and the interpretation of volcanological events. Based on ASTER TIR data, three periods of increased activity were observed that coincided with each eruption and subsequent activity. During August 2007, the May 2007 PF deposit was investigated in the field. Eight ASTER TIR pixels (90 m spatial resolution) were selected from the ASTER data acquired on 30 June 2007, seven of which were accessible in the field. ASTER temperature data were compared to FLIR and direct thermocouple data. Steam fumaroles were found to be still present on the May 2007 deposit, three months after the event. The maximum fumarole temperature was measured at 377 °C using a thermocouple and was easily detected using aerial FLIR data from a helicopter. The PF terminus region was observed to be cooler from all thermal data and also

contained a lower proportion of surface blocks. It was also emplaced on to a layer of snow which may have promoted cooling and the formation of phreatic explosion craters due to vigorous degassing. We present 14 months of ASTER and field data from Bezymianny volcano in order to assess the eruptive and non-eruptive phases at the volcano, focusing on the May 2007 PF emplacement on the southeast flank.

5.2 INTRODUCTION

5.2.1. Bezymianny Volcano

Bezymianny (55.98º N, 160.59º E, ~2900 m altitude) is an andesitic composition volcano located 350 km north of Petropavlovsk-Kamchatsky (Bogoyavlenskaya et al., 1991. Figure 14). The volcano was inactive for about one thousand years before reactivating in 1955, resulting in a cataclysmic eruption on 30 March 1956 (Gorshkov 1959; Belousov 1996; Belousov et al., 2007). This generated a 1.3 km (north-south) by 2.8 km (east-west) horseshoe-shaped crater opening to the south east. Subsequently, a long-term phase of lava dome growth began in the crater, which was mostly endogenous prior to 1969 (Bogoyavlenskaya and Kirsanov, 1981). Exogenous activity became more common after 1977 (Alidibirov et al., 1990; Bogoyavlenskaya and Kirsanov, 1981). During the last 30 years, Bezymianny has been regularly active, erupting one to two times per year on average (Belousov et al., 2002; Ramsey and Dehn, 2004; Carter et al., 2007a, 2007b, 2007c, Carter and Ramsey, 2008a).

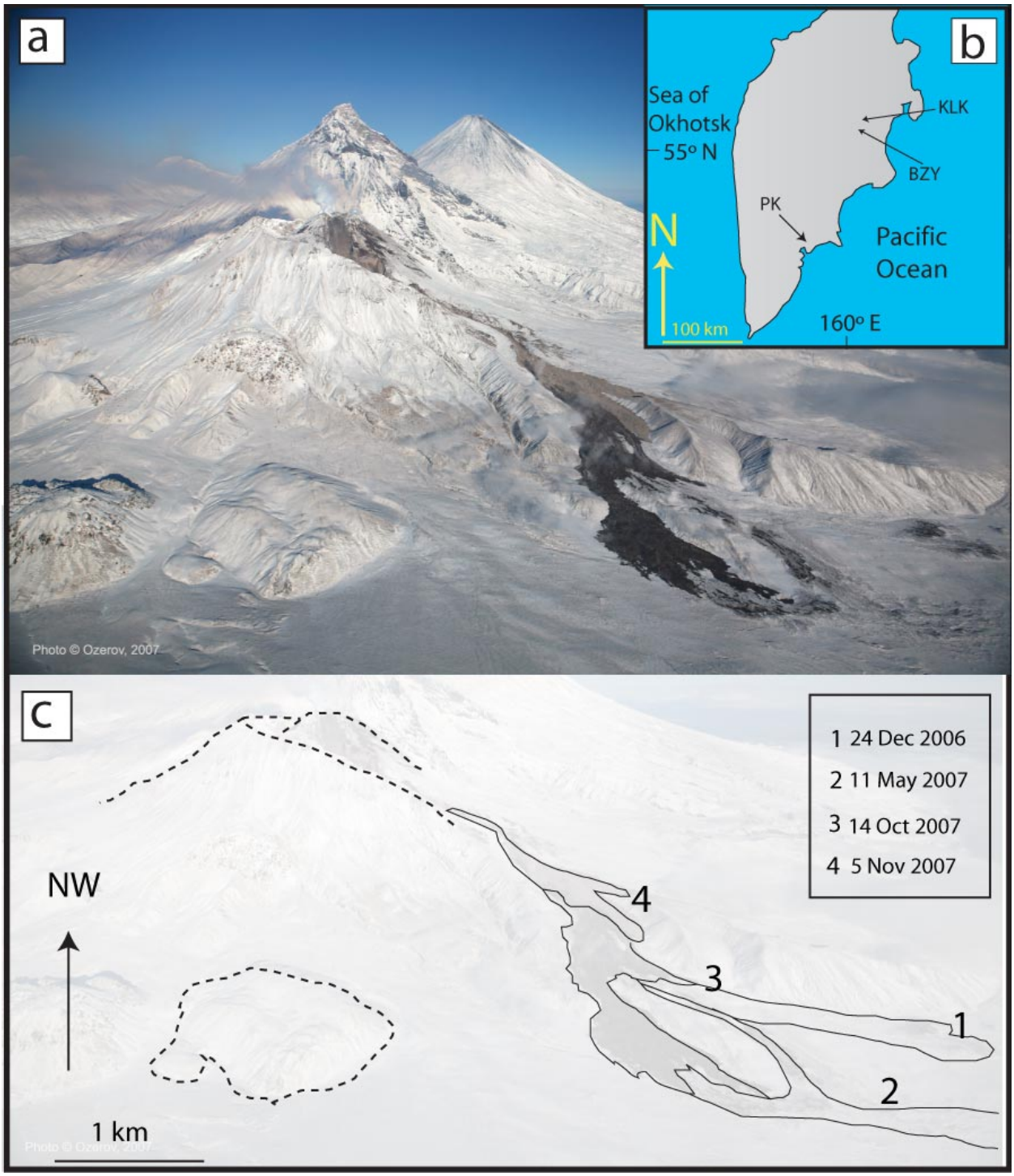

Figure 14 (a) Aerial photo taken from a helicopter facing to the northwest. Pyroclastic flow deposits from the three eruptions (24 December 2006, 11 May 2007, and 14 October 2007) can be seen overlapping on the south-southeast flank. Following the October eruption, a deposit dominantly of collapse origin was emplaced on 5 November 2007. (b) Location map. (c) Traced outline of each PF deposit.

However, this activity has been punctuated by much larger eruptions such as the sub-Plinian events of 1985 and 1997 (Alidibirov et al., 1990; Belousov et al., 2002) and the more recent 9 May 2006 eruption (KVERT, 2007). As such, Bezymianny is an important volcano to monitor because it is not only a threat to the sparse local population but is also capable of producing ash-rich plumes that can drift into North Pacific air traffic routes (Miller and Casadevall, 2000; Papp et al., 2005).

5.2.2. Purpose

Within this article, we build on recent work that looked at individual eruptions (Carter et al. 2007a; 2007b, 2007c; Carter and Ramsey, 2008a) by analyzing ASTER data from October 2006 to December 2007 due to the collection of new data over this area. The 2006-7 time period encompassed three discrete eruptions at Bezymianny. We also present ground-based thermocouple (*e.g.* Harris and Maciejewski, 2000) and FLIR data (*e.g.* Patrick et al., 2007) for comparison to ASTER-derived measurements. Together, these data provide supplementary high spatial resolution validation for lower spatial resolution/ higher temporal resolution AVHRR data (*e.g.* Dehn et al., 2000) which is used in monitoring of North Pacific volcanoes, studied by the Alaska Volcano Observatory (AVO).

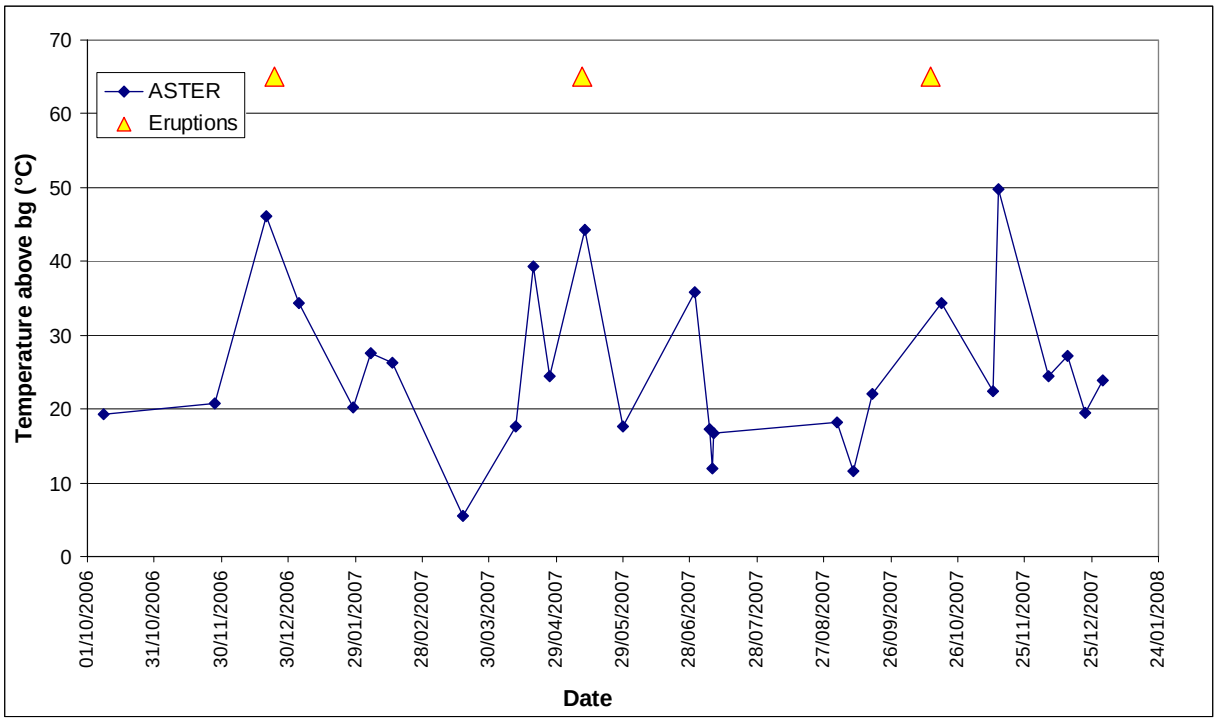

Figure 15 TIR-derived maximum temperature over the lava dome using ASTER data from October 2006 to December 2007, with the three eruption events marked with triangles. Three groups of thermally elevated values occurred around the eruption dates. High temperatures were recorded for the December 2006 and May 2007 events; however they were not detected prior to the October 2007 events which may have been due to the dome being obscured by clouds.

5.3 METHODS

5.3.1. ASTER data acquisition and processing

ASTER is a spaceborne sensor containing three spectral subsystems: VNIR, SWIR, and TIR (Yamaguchi et al., 1998). All three datasets can be used in combination to look at, for example, visual 2D and 3D changes (VNIR, *e.g.* Stevens et al., 2004), high-temperature magmatic and fumarolic events (SWIR, *e.g.* Pieri and Abrams, 2004), and lower-temperature fumarolic, degassing, and PF events (TIR, e.g. Ramsey and Dehn, 2004). ASTER has been used in several cases to interpret volcanic events at Bezymianny since its launch in 1999 (Ramsey and Dehn, 2004; Carter et al., 2007a, 2007b, 2007c; Carter et al., 2008). From October 2006 to December 2007, 30 ASTER level 2 (L2) Surface Kinetic Temperature images were collected. The number of clear images in this area is limited due to heavy winter snow cover and north pacific cloud cover in summers. An automated atmospheric correction was already applied to the L2 dataset using the National Centers for Environmental Protection (NCEP) atmospheric transmission data and the temperature product was derived by separation from the radiance product using a Temperature-Emissivity Separation (TES) algorithm (Gillespie et al., 1998). For emissivity data, the AST_05 L2 Surface Emissivity data product was used (Gillespie et al., 1998).

5.3.2. Field methods

A base map of the May 2007 deposits was created using a night time ASTER image from 30 June 2007. ASTER images over Bezymianny acquired after this date were obscured by cloud cover. Errors in geo-location are common in ASTER night time data. To correct for this, an orthorectified daytime TIR image from 8 July 2007 was used to shift the 30 June 2007 image 440 m east and 90 m north. Eight pixels were selected over the May 2007 PF based on the criteria of being: (a) relatively high temperatures and (b) of approximately equal spacing along the PF deposit. Seven were accessible in the field (pixels 1-7) and were investigated in August 2007. The co-ordinates of the corners of each ASTER 90 m pixel were precisely located in the field. FLIR images were collected at a distance of 1 m from the surface facing vertically downwards for each pixel corner and pixel centre and all five values were averaged. An Omega HH509 thermocouple was used to measure the surface kinetic temperature of the PF deposit in each pixel corner and the centre and these data were also averaged. ASTER temperature data were collected for all pixels, corresponding thermocouple data were collected for pixels 1 – 7, and corresponding FLIR data were collected for pixels 4, 5, and 6. The latter was most dependent on field assistance, logistics, weather conditions, and FLIR camera availability. Pixels 1 – 7 were also assessed for surface land cover type by estimating the percentage of blocks, relative to ash on the surface. This was assessed using transects where measurements were made approximately every 3 m, running diagonally from corner to corner over each 90 m pixel.

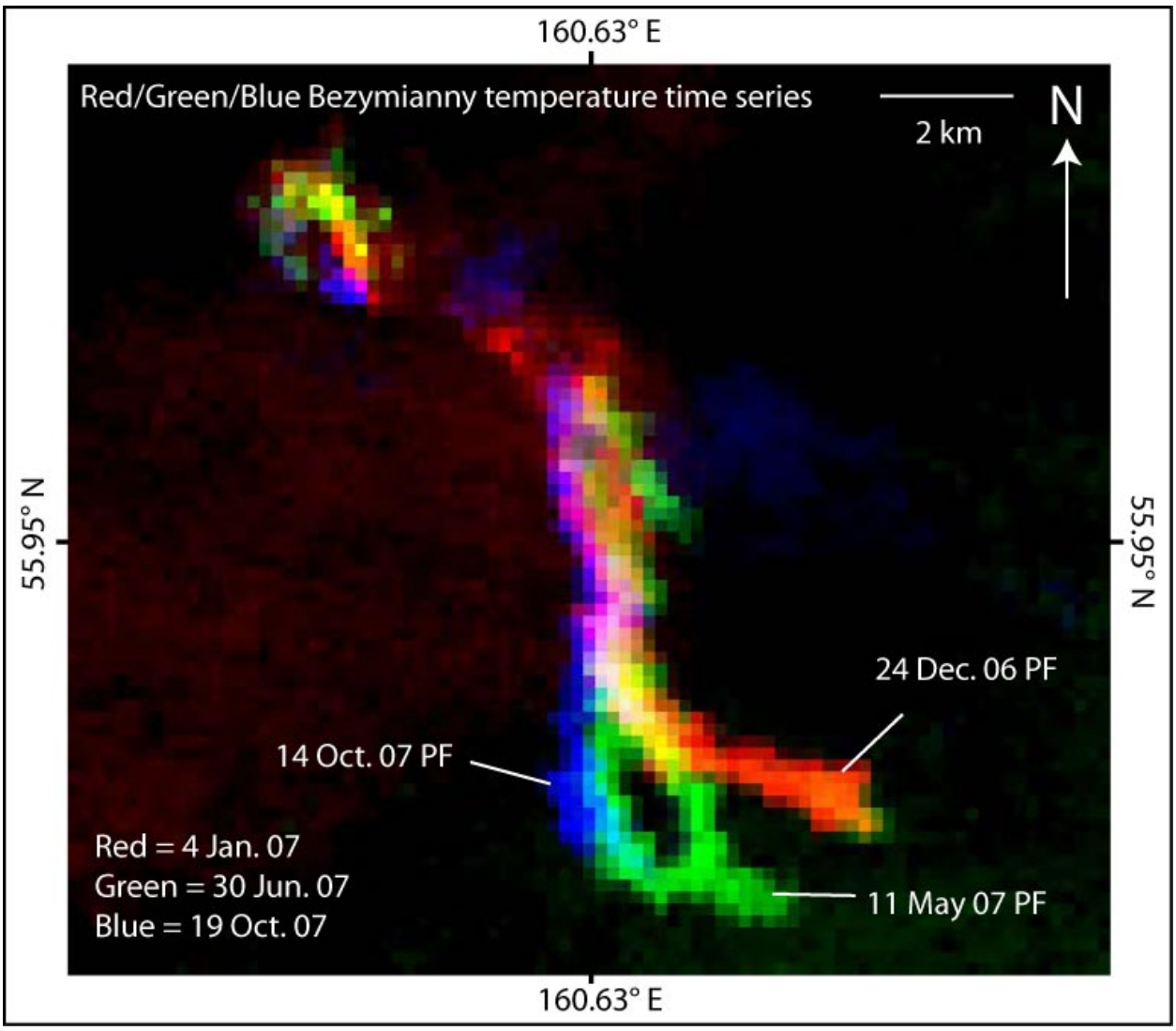

Figure 16 Composite, three colour (red, green, blue) ASTER TIR temperature data from 4 January, 30 June, and 19 October 2007. The dome region (upper left) was thermally elevated in the northwest region of the dome on 4 January and 30 June 2007 (yellow), but by 19 October, this elevated region was more located on the south portion of the dome. Three pyroclastic flows were accurately located from 24 December 2006 (red), 11 May 2007 (green), and 14 October 2007 (blue), each with a unique spatial footprint.

5.4 ERUPTION DESCRIPTIONS

5.4.1. The 24 December 2006 eruption

On December 24 at 02:40 UTC, the colour code for Bezymianny volcano was raised from Orange to Red (KVERT, 2007). A KVERT level of concern Red colour code indicates that a major explosive eruption is expected within 24 hours (AVO, 2008). This can be accompanied by ash plumes reaching at least 7.5 km ASL. As predicted by this colour code upgrade, Bezymianny volcano erupted explosively at 09:17 UTC, 24 December 2006, generating an ash plume that rose to approximately 10 km above sea level (Girina et al., 2006). This produced a fresh PF deposit extending 7.2 km to the southeast as well as a short lava lobe that was concentrated in a depression that extended to the southwest from the central crater on the lava dome (Carter et al., 2008a).

5.4.2. The 11 May 2007 eruption

Bezymianny volcano's alert colour code was raised from Yellow to Orange on 10 May 2007 (KVERT, 2007). An Orange colour code implies that an explosive eruption is possible within a few days and may occur with little or no warning. In this case, ash plumes would not be expected to exceed 7.5 km a.s.l., although dome growth and the extrusion of lava is possible. On

12 May 2007, KVERT released a status report stating that, based on seismic data, an explosive eruption had occurred at Bezymianny on 11 May from 14:30 to 15:00 UTC (KVERT, 2007). Interpretation of seismic data from this event was complicated by seismic noise from nearby Klyuchevskoy volcano, which was erupting at the same time. Multiple ash plumes were visible by residents over northern Kamchatka, which may have originated from both Bezymianny and Klyuchevskoy. According to visual data (web camera) from Kozyrevsk village, 50 km west of the volcano, a hot avalanche occurred at Bezymianny at 22:30 UTC, May 11 and on the same day an ash plume rose to 4 km ASL Using MODIS data, a thermal anomaly was observed extending several km to the southeast, which was inferred to be due to the emplacement of a PF deposit (KVERT, 2007).

5.4.3. The 14 October 2007 eruption and 5 November 2007 collapse

A high-intensity MODIS thermal anomaly was observed over the lava dome in the days preceding the eruption (KVERT, 2007). On 14 October 2007, KVERT raised the concern colour code from Yellow to Red. KVERT announced that, based on MODIS data, a small eruption of the volcano had occurred. According to seismic data, two eruptive events occurred from 14:27 - 14:48 UTC and from 15:10 - 16:30 UTC on October 14. Activity continued until 15 October around 14:00 UTC. Ash plumes extended more than 100 km to the south-east from the volcano. In the following days a new viscous lava flow was observed on the dome. On 5 November 2007, according to seismic data there was a series of small explosive events or collapses from the frontal part of a lava flow from 08:43 till 10:10 UTC with two additional avalanches occurring at 15:45 UTC and 18:07 UTC (KVERT, 2007). We interpret the 5 November 2007 event as

predominantly of collapse origin, and therefore do no include it as an explosive eruption event during the 2006 to 2007 study period.

5.4 AERIAL PHOTOGRAPHY, ASTER- AND LABORATORY DATA INTERPRETATION

Observations of the 24 December 2006 and 11 May 2007 eruptions are summarised in Carter et al. (2008a) and Carter et al. (2007c), respectively. However there has been far less research on the October 2007 eruption. Aerial photographs from November 2007 showed clear evidence of each PF produced from each eruption, and confirmed the presence of the latest PF from October 2007. The latter can clearly be separated into two distinct units (Figure 14 c): (1) a dark, low albedo unit that travelled a maximum of 6.4 km from the dome and separated in two directions around a topographic barrier in a similar manner to the May 2007 PF; and (2) a brighter, high albedo unit (or series of units) emplaced by a flow which travelled less far (3.6 km) than the others. It was noted by KVERT scientists that for the second and smaller event, the deposits appeared to contain predominantly dome-derived, non-juvenile material. The second deposit was a result of a collapse event which was generated later from dome instability and/or a collapsing lava lobe front on 5 November 2007. A remote sensing study of these varied deposits is planned for future work.

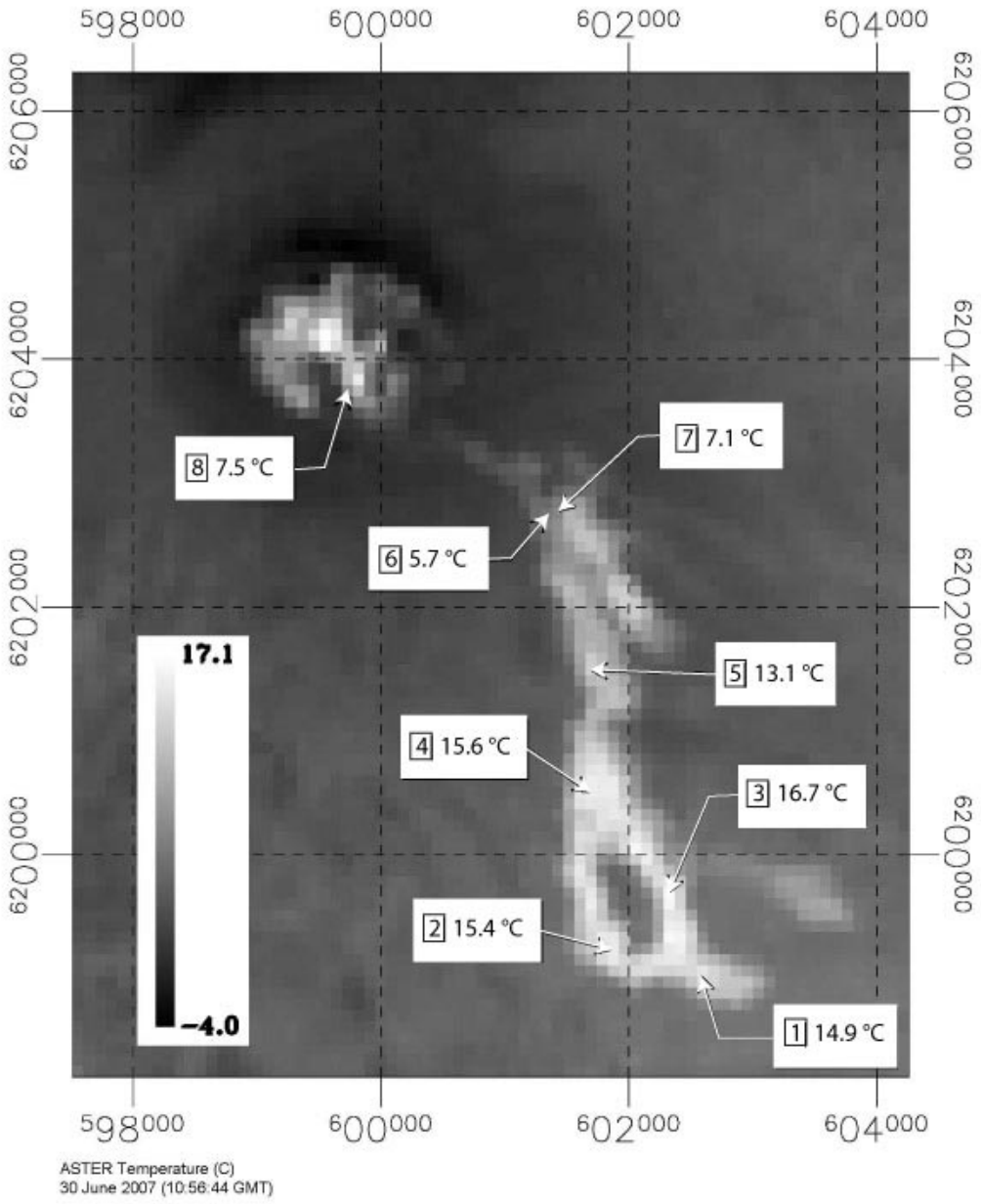

Figure 17 ASTER night time image from 30 June 2007 with eight TIR pixels, seven of which (all except pixel 8) were visited in the field. The warm temperatures from the May 2007 PF deposit can be clearly seen.

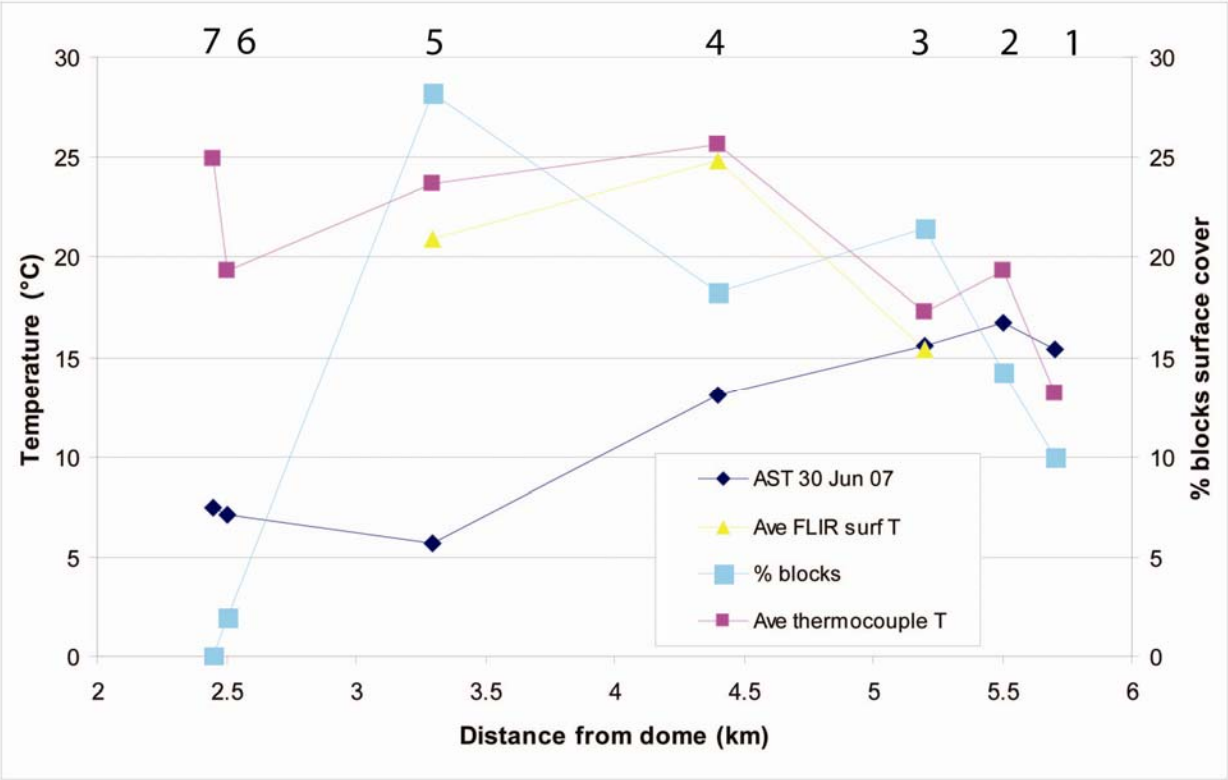

Figure 18 Temperature profiles over the May 2007 PF deposit from ASTER temperature above background data from 30 June 2007, averaged FLIR ground-based images, and averaged thermocouple temperatures. FLIR and thermocouple data were collected in August 2007. In addition the surface % of blocks was estimated in the field and recorded (second y-axis). Each ASTER pixel is marked at the top of the graph.

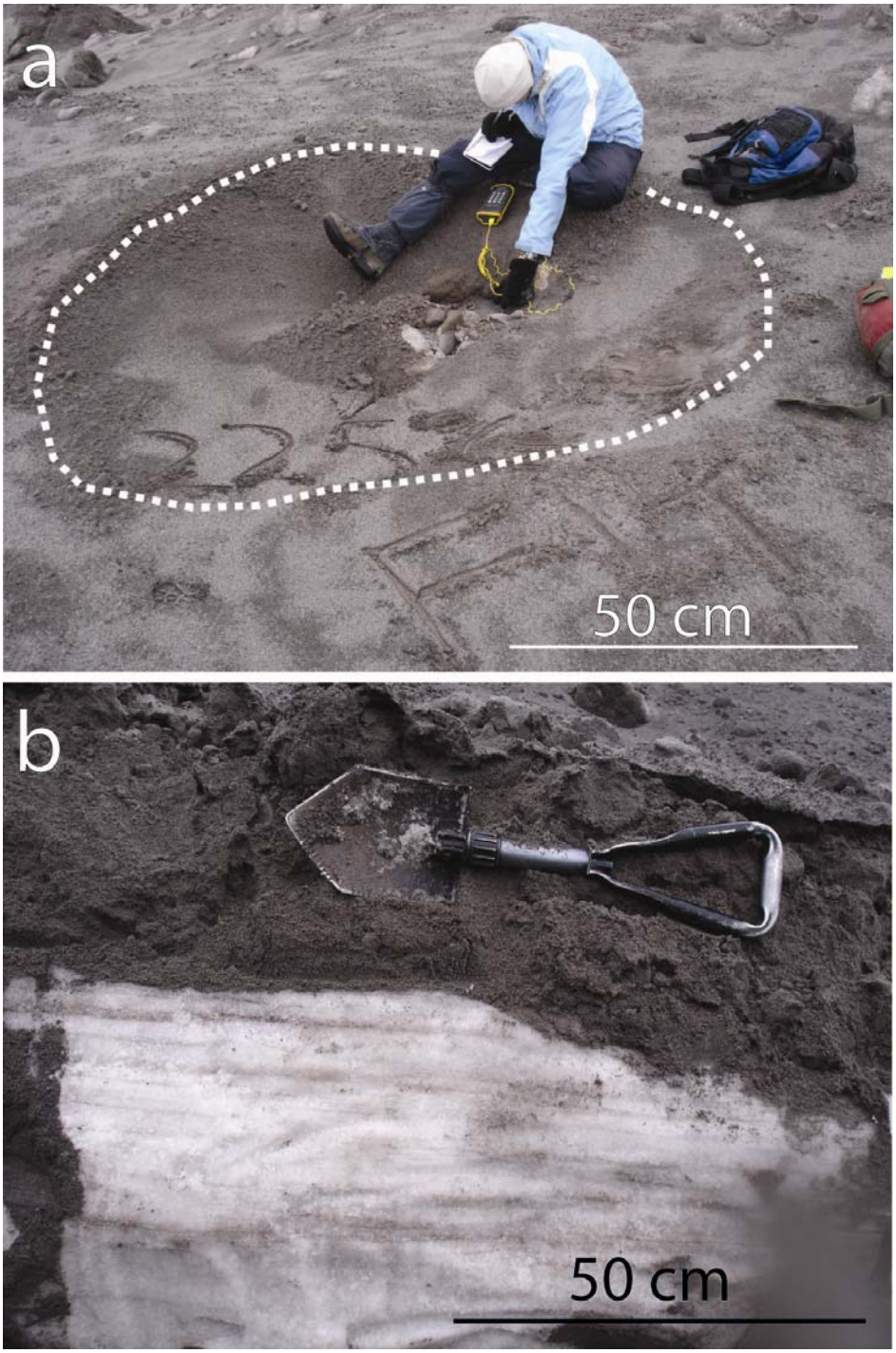

Figure 19 Field photographs near the PF terminus. (a) Steam explosion crater, over 1 m in diameter. The maximum temperature recorded was 225 °C. (b) Snow layer underneath the May 2007 PF deposit. Flow direction was to the right (southeast).

Carter et al. (2008a) analyzed the December 2006 eruption using ASTER data and showed a distinct thermal precursory signal in SWIR and TIR data four days prior to the eruption and increased thermal activity in the following four months. Subsequently, 14 months of ASTER temperature data were collected from October 2006 to December 2007 (Figure 15). Three peaks were noted in the data around the three eruptions, although precursory signals were not detected for the May and October 2007 events. This may have been due to frequent cloud cover in the region over the summer/ autumn months, or that the lower temporal resolution (due to image acquisition priorites on other projects) of ASTER may have missed the thermal signal. A composite of three of these ASTER TIR images (acquired on 4 January, 30 June, and 19 October 2007) shows the overlapping PF deposits (Figure 16). Statistics on the general properties of the three PFs were collected (Table 6). The area covered for the December 2006, May 2007, and October 2007 eruptions were 1.8, 3.1 and 1.7 km^2, respectively, with run out distances of 7.2 km, 7 km, and 6.4 km. Thus, the May 2007 PF was over 1.5 times larger in surface area than the other deposits, based on ASTER observations.

Over the summit, an ASTER image from 19 October showed a distinct thermal TIR thermal anomaly over the southern part of the lava dome. This was due to the emplacement of a lava lobe that later partially collapsed on 5 November 2007. Thus, ASTER observations detected another post-eruption lava lobe emplacement, in agreement with activity previously described by Belousov et al. (2002), Ramsey and Dehn (2004), Carter et al. (2007a), and Carter et al. (2008a).

Five band TIR emissivity data were collected for the three dates after each eruption (Table 1). A region of interest was selected over the spatial footprint of each PF deposit and the data were clipped to within this footprint.

Table 6 Pyroclastic flow results from each eruption using ASTER data.

PF date	**24-Dec-06**	**11-May-07**	**14-Oct-07**
PF perimeter distance (km)	13.24	13.71	10.63
PF area (sq. km)	1.81	3.09	1.73
PF run out distance from dome summit (km)	7.20	7.00	6.40
ASTER image used	04-Jan-07	30-Jun-07	19-Oct-07
Number of days after eruption	11 days	50 days	5 days
Day/night	day	night	day
Averaged PF emissivity (ASTER bands 10-14)	0.936	0.972	0.944

Statistics were calculated for each band and then averaged to give a broadband emissivity value for each deposit (0.936, 0.972, and 0.944, for December 2006, May 2007, and October 2007, respectively). Twelve block-sized and ash samples were also collected from the May 2007 deposit and analyzed using a Fourier-Transform Infrared (FTIR) spectrometer at the University of Pittsburgh, following the preparation methods of Ruff et al. (1997). To compare results to the ASTER broadband emissivity values, the thermal emission spectral data was averaged over the same spectral region (8.29 – 11.32 micrometers). Averaging all samples gave a bulk emissivity of 0.953 for the May 2007 deposit, compared to 0.972 based on ASTER TIR data, a difference of 1.9%. This information can be helpful in thermal models of pyroclastic flows when looking at thermal cooling over deposits with time, for example, textural or vesicularity effects, or the density/ thermal inertia information that relates to the proportion of blocks to ash within the PF.

5.5 FIELD-BASED AND SATELLITE DATA OF THE MAY 2007 PYROCLASTIC FLOW DEPOSIT

An ASTER thermal infrared night time image from 30 June 2007 was used to locate pixels 1 – 7 in the field (pixels 1-7, Figure 17). For the dome pixel (8), only ASTER data was available and direct field measurement and comparison was not possible due to activity at the dome. ASTER temperatures were compared to the available FLIR and thermocouple data (Figure 18). ASTER-derived temperatures from June 2007 were generally lower than the FLIR and thermocouple temperatures that were measured in August 2007, despite the field

measurements being over one month after the ASTER image. Several factors may account for this: (1) the spatial averaging of multiple thermal sources over 90 m ASTER pixels, which would typically dilute any high-temperature features, (2) the ASTER image was night time, however the FLIR and thermocouple data was collected during the day which would have had additional solar heating, (3) a slight seasonal difference as the field data was collected in August when the surface and atmospheric temperatures were higher than in June, (4) a possible over-correction in the atmospheric correction algorithm that was used which would lower the temperatures retrieved.

The thermal data were in good agreement over pixels 4, 5, 6, and 7 (Figure 18). The warmest pixel from ASTER data was pixel 3 and the warmest averaged FLIR and thermocouple pixel was pixel 4. A steady increase in temperature was observed between pixels 6 to 3, moving away from the dome. This suggests an increase in thickness and/or bulk density in the PF deposit around pixel 3, which was the point at which the PF branched in to two sections and moved around a topographic high point. In addition, the percentage of surface blocks covering each pixel was assessed and added to the thermal data (Figure 18). These data showed that the percentage of blocks was low with proximity to the dome (pixels 6 and 7), higher in the main body of the PF (> 15% blocks, pixels 3 -5), and was low at the PF terminus area (pixels 1 and 2). Logically, it is possible that as the PF split in two (south of pixel 4), larger blocks were channelled in to the two surrounding valleys. Such a block-rich area would then have a higher bulk thermal inertia and bulk density relative to more ash-rich regions. In addition, slopes decrease away from the volcano summit which would also encourage the thickening of the PF deposit in this area.

The data retrieved over pixels 1, 2, and 3, were much more correlated. The averaged thermocouple temperature for pixel 2 appeared to be anomalously higher than pixels 3 and 1. The temperature range from measurements within pixel 2 was 34 °C, the greatest range within all pixels. The pixel 2 centre temperature was taken over a fumarole area which increased the average pixel value over the five points, without which the average would have been 14 °C, significantly lower. Thus, the trend from pixel 3 to pixel 1 was more likely a gradual negative slope towards the PF terminus in the thermocouple data.

At the PF terminus, steam explosion/ vigorous degassing craters were observed which must have occurred after the PF was emplaced (Carter et al., 2007c. Figure 19 a). Temperatures up to 225 °C were recorded from thermocouple data inside the fumarole centres. The PF terminus was relatively abrupt (over 5- 10 m) and was emplaced in this area on to a dominantly fluvially- deposited, outwash plain. On the southern border of the PF between pixels 1 and 2, a snow layer was observed directly beneath the PF deposit that contained incised tunnels created by melt water (Figure 19 b).

We interpret that the terminus area underwent more rapid cooling (relative to pixels 4 to 7) between the ASTER image date (30 June) and the fieldwork (August) based on the following: (a) the proportion of blocks (and bulk density) of the PF was found to be lower in this area and contained a higher proportion of ash (Figure 17). This would have a lower bulk thermal inertia and density and would lose heat more rapidly. (b) Secondly, it was noted that the lower portion of the PF (between pixels 2 and 1) was emplaced on to a snow layer that was found beneath the deposit. Over a time scale of weeks to months, the lower temperatures in the snow layer may have promoted heat loss on the PF. (c) Thirdly, pixels 3 up to 7 were located in areas that were emplaced on top of the still-warm December 2006 PF deposits and thus the derived temperatures

may have been influenced by this, whereas pixels 1 and 2 were emplaced on ambient temperature, cooler deposits and on to a fluvial outwash plain with dispersed snow layers. This may account for the ASTER temperature increase up to pixel 3 followed by a slight decrease in temperatures around pixels 2 and 1. All factors may have contributed to the much lower range (8 °C) of temperatures observed between ASTER, FLIR and thermocouple measurements.

Several fumaroles were observed over the entire PF deposit that were warmer than the majority of the PF surface. The warmest fumarole found on the ground was measured at 377 °C using the thermocouple on 18 August 2007 and was located on the southeast branch of the PF. It was within 5 m from the edge of one of the PF lobes and was 5 km from the dome summit (Figure 20). It was also detected in aerial FLIR data as a clear thermal anomaly, relative to the rest of the deposit (Figure 21). Such high temperatures from the deposit, three months after the event, suggest that the deposit must have been of sufficient thickness and/or bulk density to retain large amounts of heat. This suggests, in combination with the fact that the May 2007 PF covered a larger surface area than the other two deposits, that the deposit was also of greater thickness and larger in total volume.

5.6 DISCUSSION/CONCLUSIONS

Fourteen months of ASTER data were used to produce a moderate spatial resolution, moderate resolution dataset.

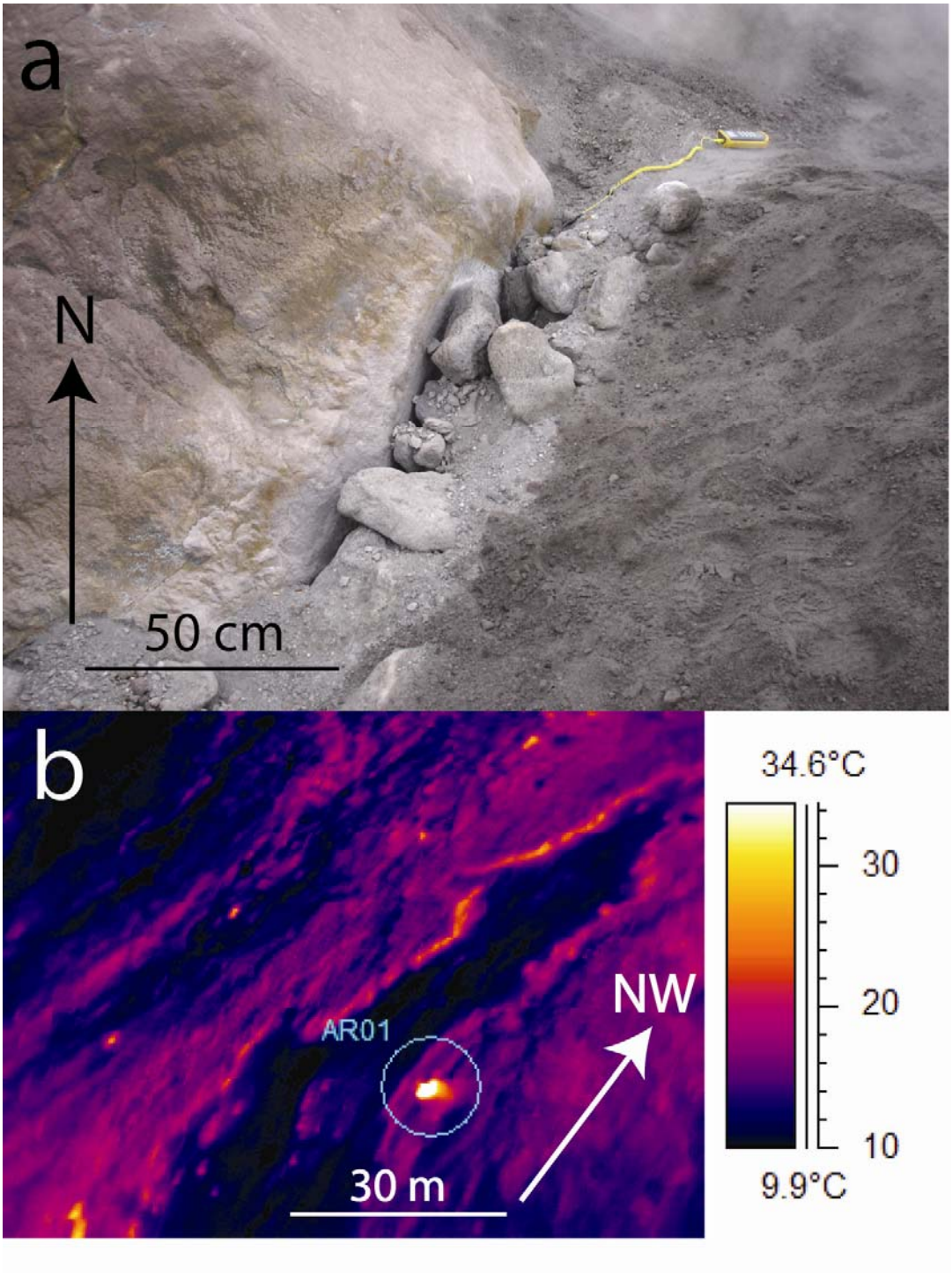

Figure 20 (a) Field photo graph of the maximum temperature fumarole on the May 2007 PF deposit, 5 km from the dome summit. The maximum temperature recorded was 377 °C with a thermocouple. (b) Aerial, near-vertical FLIR image over the May 2007 PF deposit with the fumarole circled in blue.

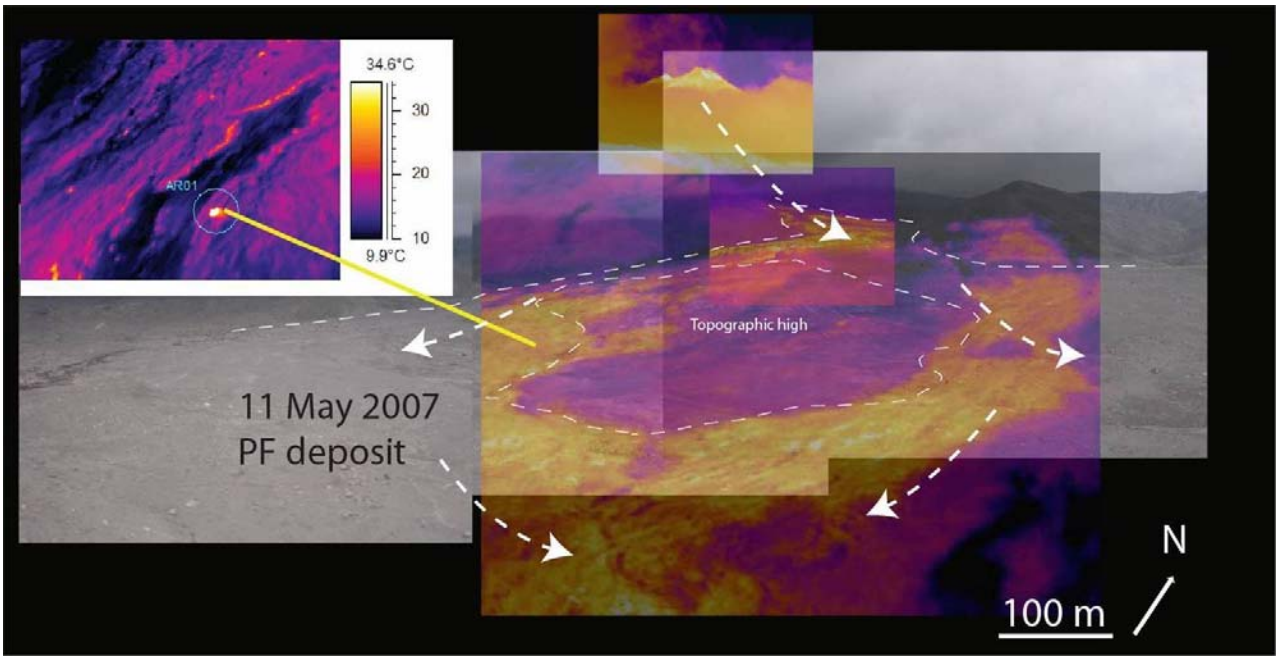

Figure 21 Oblique aerial photograph composite taken from the southeast flank facing northwest towards the dome. FLIR image of the dome region and May 2007 PF deposit is overlain to show the topographic high region. Inset: aerial FLIR image of the May 2007 PF deposit. Circled area represents the warmest fumarole (see Figure 20) that was detected from aerial data.

Three explosive eruptions were detected and ASTER multi-temporal TIR image composite was used to provide an accurate geospatial footprint for each PF deposit.

The May 2007 PF covered an area of over 3 km^2 and was over 1.5 times larger in area than the December 2006 and October 2007 PF deposits. ASTER emissivity data were collected over the three PF deposits and differed by only 1.9% with laboratory-derived data, suggesting a relatively good agreement between the datasets. This provided an opportunity to validate ASTER-derived surface emissivity values and compare them to spectra from samples collected on the ground. Based on all thermal data, and surface land cover to estimate the percentage of blocks to ash (Figure 18), we interpret that the PF deposit was more block-rich in the main body of the flow, but had a more ash dominated region behind the main flow where slopes were higher and also at the PF terminus area. More rapid cooling would occur in the lower bulk density, ash-rich areas found at the high slope angles and, in this case, at the PF terminus. Compared to the December 2006 deposit (Carter et al., 2008a), we interpret that the May 2007 PF deposit had a more gradational, ash-dominated terminus, rather than a more block-rich terminus. This may have been caused by the topographic high point that separated the PF and forced the emplacement of blocks around this area (*i.e.* pixels 3 and 4).

At the PF terminus, several explosion/ vigorous degassing craters were found on the surface (Figure 19 a) in the same area as a snow layer beneath the PF in this area (Figure 19 b). We interpret that phreatic explosions generated the craters as the PF encountered the snow layer. In addition, the snow base layer would have promoted more rapid heat loss after emplacement which may explain the lower temperature range between the ASTER, FLIR, and thermocouple

datasets. Unfortunately, all ASTER image acquisitions synchronous with the field investigation were cloud-covered, so the 30 June 2007 image was used. This does not allow for the

All of the available information suggests the deposit contained: (1) a block-rich and thicker part in the centre of the flow at around 5 km distance, (2) and ash-rich area close to the lava dome where slopes were high (3) an area upslope and around the topographic high point that separated the PF into two branches that contained the most blocks/ greatest thickness, and (4) the PF terminus area where the two branches joined back together where steam explosion craters were seen and the PF was emplaced on to snow.

Combined field-based and satellite data have proven to be a highly valuable resource for interpreting repeated volcanic events at Bezymianny since the launch of ASTER. ASTER data provides quantitative volcanological data on the scale of several days to weeks and can be used, as presented here, to consider over a year of data to look for variations in activity levels. There is a continued need to monitor volcanoes in the North Pacific, many of which are difficult or impossible to access and have very limited or no ground-based observations. This must be carried out in conjunction with local Russian (KVERT) and Alaskan (AVO) groups to facilitate information transfer between agencies, government bodies, and the aviation industry.

6 MICRON-SCALE ROUGHNESS OF VOLCANIC SURFACES FROM THERMAL INFRARED SPECTROCSCOPY AND SCANNING ELECTRON MICROSCOPY

6.1 CHAPTER SUMMARY

Textural characteristics of recently-emplaced volcanic materials provide information on the degassing history, volatile content, and future explosive activity. Thermal infrared (TIR) remote sensing has previously been used to derive the micron-scale roughness (*i.e.*, vesicularity) of lavas using a two-component (glass plus blackbody) spectral deconvolution model. We apply and test this approach on data from recently-emplaced pyroclastic flow (PF) deposits for the first time. Samples from two PF deposit areas (January 2005: block-rich and March 2000: ash-rich) were collected at Bezymianny Volcano (Russia) and analyzed using: (1) TIR emission spectroscopy; (2) Scanning Electron Microscope (SEM)-derived roughness (profiles); (3) SEM-derived surface vesicularity (imaging); and (4) traditional thin sections. Results from SEM roughness (0.9-2.8 μm) and SEM vesicularity (18-26%) showed a positive correlation. These were compared to the deconvolution results from the laboratory and spaceborne spectra, as well as to field-derived percentages of block and ash. The spaceborne and laboratory spectral results were consistent with each other and showed a positive correlation to within 1%. However, a negative correlation between the SEM and spectral results was observed and is likely due to a combination of an incorrect glass end-member as well as particle size effects and subsequent

weathering of the ash particles. Despite these differences, this work does show that microscopic textural heterogeneities on PF deposits can be detected with TIR remote sensing in a similar way to lavas, but the results must be carefully interpreted. If applied correctly, such an approach is an important tool to map recent PF deposits and infer the responsible eruption style at any active/dangerous volcano.

6.2 INTRODUCTION

6.2.1. Vesicularity and surface change detection

Changes in the vesicularity of active lava domes and flows can provide useful information on degassing and volatile content for example, which can be used to infer the risk of impending explosive activity (Anderson and Fink, 1990). Calculating vesicularity on in-situ samples is commonly difficult and dangerous on active volcanoes. However, a collected sample can be analyzed using several techniques: optical microscopy (*e.g.* Sarda and Graham, 1990), application of Archimedes' principle (Houghton and Wilson, 1989), and analysis of digital images collected by Scanning Electron Microscope **(**SEM) (*e.g.* Heiken and Wohletz, 1985; Klug and Cashman, 1994). In addition, modern three-dimensional imaging techniques such as Synchrotron X-ray microtomography have been used to generate accurate volume estimates for

vesicular particles (*e.g.* Song et al., 2001). This technique has also been applied in other disciplines to quantify the surface characteristics of various substances at the micron scale (*e.g.*, Minnich et al., 2001; Podsiadlo and Stachowiak, 1997). However, few studies have concentrated on the use of stereo images to analyze both two and three dimensional (3-D) samples of volcanic materials.

The surfaces of eruptive products can undergo rapid textural changes during active volcanism due to degassing, explosions, erosion/weathering, and the emplacement of new deposits. For example, pyroclastic density currents, lahars, and lava dome building and destruction phases have been observed at Soufrière Hills Volcano Montserrat (Watts et al., 2002), Mt. Unzen, Japan (Nakada et al., 1995) and Mount Saint Helens, USA (Anderson and Fink, 1990; Vaughan et al., 2005). At all of these volcanoes the deposits underwent rapid surface change during activity. Macro-scale (*i.e.* meter scale and above) changes can be easily observed and analyzed using higher-resolution aerial and satellite images in order to monitor the emplacement of new deposits, secondary reworking, and larger scale topographic changes such as dome collapse (*e.g.* Francis et al., 1996). However, microscopic-scale detection and change require analysis at a resolution several orders of magnitude greater than what is available from satellites and aerial images. Of particular interest is the micrometer (micron)-scale (1 – 100 μm) because it can alter and affect thermal infrared (TIR) energy, which is emitted at the same scale. For example, particle size effects and surface textures such as vesicularity and micron-scale roughness can all be derived from morphological changes in the emitted TIR spectra (Moersch and Christensen, 1995; Ramsey and Fink, 1999; Kirkland et al., 2002).

For the work presented here, we compare the merits and limitations of several different datasets to estimate the surface vesicularity and micron-scale roughness (a proxy for vesicularity)

in samples of PF deposits from Bezymianny Volcano, Russia. The primary goal was to assess how accurately satellite-derived thermal emission spectra could be modeled in order to extract micron-scale roughness and map the percentages of blocks and ash, all of which relay important clues about the eruption style that produced the deposit. Here, we compare the laboratory- and satellite-based TIR model results to: (1) field-based mapping of the percentages of blocks and ash on two different PF deposits, (2) the surface vesicularity of samples collected in the field derived from SEM images, and (3) SEM surface roughness derived from the profiling measurements of these same samples. This work tests the TIR remote sensing technique described in Ramsey and Fink (1999) and Ramsey and Dehn (2004), applying it for the first time to PF deposits. The information extracted from such an approach using is critical for any active volcano where field mapping is too dangerous or for any remote volcano where the actual eruption responsible for the PF deposit was not observed.

6.2.2. The eruptive products of Bezymianny Volcano

Bezymianny (55.98º N, 160.58ºE, ~2900 m altitude) is an active composite volcano on the Kamchatka Peninsula, Russia (Bogoyavlenskaya et al., 1991), with one to two eruptions per year (Belousov et al., 2002; Ramsey and Dehn, 2004). Its name ("no name" in Russian) was given by scientists during visits prior to 1955 because of its assumed insignificance and inactivity compared to its much larger neighbor, Klyuchevskoy Volcano. Bezymianny became well-known after its March 1956 eruption that created a directed blast and sector collapse during a large Plinian eruption (Gorshkov, 1959). Volcanic products are typically basaltic-andesites and andesites with a SiO_2 range of 52.5% to 65.5% (Bogoyavlenskaya et al., 1991). Since 1956, a

new lava dome has grown within the collapse crater (Bogoyavlenskaya and Kirsanov, 1981), and currently exceeds the height of the 1956 collapse scar to ~2,900 m elevation.

On 14 March 2000, the Kamchatka Volcanic Eruption Response Team (KVERT) reported continuous volcanic tremor, indicating an eruption was in progress (KVERT, 2007). An ash cloud traveled ~8 km above sea level (ASL) and a sizeable ash-rich PF traveled east into both branching valleys on the volcano. Nearly five years later (11 January 2005), another explosive eruption occurred and was recorded by seismic data (KVERT, 2005). An ash plume rose 8-10 km ASL and block-rich PF deposits were later observed to have traveled up to 3 km from the vent. This was a typical run out distance for the numerous small eruptions within the last seven years (Ramsey and Dehn, 2004; Carter et al., 2007; Carter et al., 2008).

6.3 BACKGROUND AND METHODS

6.3.1. Bezymianny sample descriptions

We surveyed the recent PF deposits in August 2005 along the eastern flank and into the southeast branching valley (Figure 22 a – 22 d). The PF deposits were mapped using Global Positioning System (GPS) data and surveyed to assess the percentages of block and ash.

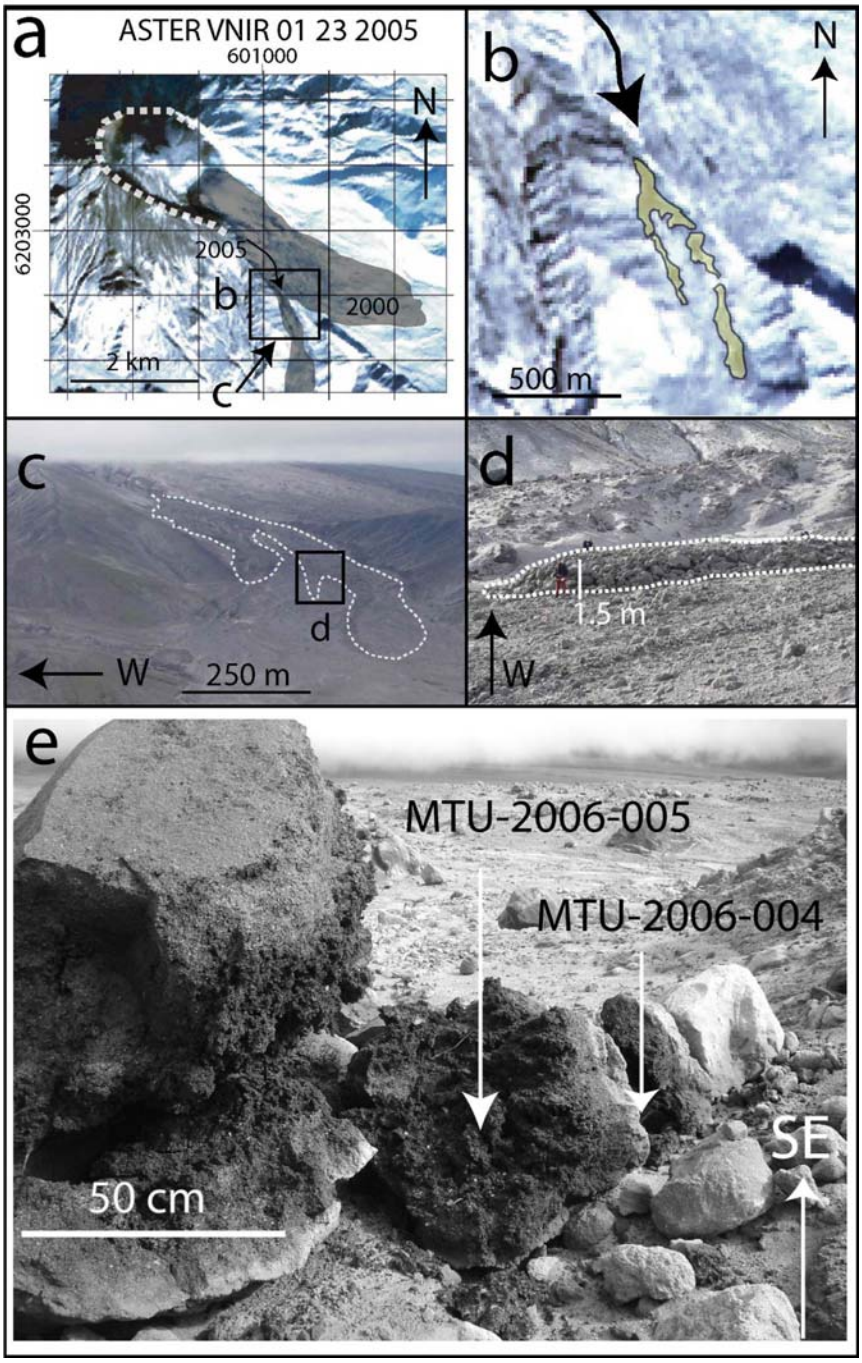

Figure 22 ASTER image taken on 23 January 2005 to show the Bezymianny lava dome surrounded by the c-shaped 1956 crater (white dashed lines) and pyroclastic flow sheet to the southeast. The March 2000 PF is shown as a shaded area and the direction of the January 2005 PF is shown entering the southeast branching valley. (b) Outline of the January 2005 PF within the valley. (c) Aerial image taken in August 2005 to show the outline of the January 2005 PF. (d) Field image to show block-rich lobes within the January 2005 PF. (e) Blocks from the January 2005 PF deposit in the southeast branching valley. Two distinct textures were observed: a grey surface rind (MTU-2006-004), and a black interior (MTU-2006-005).

These surveys were carried out over 90 square meters corresponding to the corners of one Advanced Spaceborne Thermal Emission and Reflection Radiometer (ASTER) TIR pixel, which were chosen prior to the field campaign based on the ASTER data. The aim was to characterize the two different PF deposits and assess surface types. Therefore, although several pixels were surveyed in the field, only two were selected for this study. The first was on the 11 January 2005 deposit (area 1) and the second was on the March 2000 deposit (area 2). Both deposits were unconsolidated and non-vegetated. Numerous samples were collected randomly within each pixel, comprising blocks and ash from the PF deposits. Four SEM images were chosen for detailed analyses described in the sections below (Table 7). Two samples were from the 11 January 2005 PF deposit (area 1, sample MTU-2006-004 and -005, referred to as -004 and -005 from here on). Further down slope, on the 14 March 2000 deposit, two ash particles were imaged (area 2, sample MTU-2006-001, referred to as -001-P1 and -001-P4 from here on) within the sample -001. TIR emission spectra were collected for samples -004, -005, and from 2 grams of ash sample -001, within which images of individual particles -001-P1 and -001-P4 were collected.

The surface of area 1 was covered with approximately 30 % blocks and 70 % ash from the January 2005 eruption. Samples -004 and -005 were taken from a random representative pyroclastic block within this region (Figure 22 e). The block measured 1.5 m high and was rounded by abrasion during transport within the PF. Sample -004 was taken from the exterior surface and was considered the dominating block type within this area. Sample -005 was taken from the interior, which was partially exposed. This sample was not as a major end-member for surface cover, but was chosen in order to examine any textural heterogeneity within the blocks and to assess the degree of vesiculation during eruption.

Table 7 Description of SEM images of samples collected from the 14 March 2000 and January 2005 pyroclastic flow deposits at Bezymianny.

Sample number	Eruption Date	Location (UTM, WGS-84)	Block/ particulate	Average vesicle diameter (μm)	Brief description
MTU-2006-001-P1	Mar-00	6199981.77 m N, 602378.80 m E	particulate	<80	Single image of a lapillus 5 mm wide from within sample MTU-2006-001.
MTU-2006-001-P4	Mar-00	6199981.77 m N, 602378.80 m E	particulate	~30	Single image of an ash particle 300 μm long, 150 μm wide from within sample MTU-2006-001.
MTU-2006-004	Jan-05	6200261.35 m N, 601986.869 m E	block	<100	Taken from the outer surface of a rounded pyroclastic block within the January 2005 PF deposit. Grey in color, visibly rough.
MTU-2006-005	Jan-05	6200261.35 m N, 601986.869 m E	block	<80	Taken from the interior of a rounded pyroclastic block that had fragmented during emplacement within the January 2005 PF deposit. Black in color and less visibly rough than sample -004.

This block, and others in the deposit, were mechanically fragmented during emplacement, occasionally exposing a darker black interior (sample -005) relative to the lighter grey outer surface (sample -004). The March 2000 deposit (area 2) was far more ash-rich (10 % blocks and 90 % ash) and was further weathered compared to the more recent January 2005 deposit.

6.3.2. SEM-derived surface roughness background

Roughness (or rugosity) can be described as a measurement of the small-scale variations in the height of a physical surface, or its lack of order (Thomas, 1999). Each measured roughness profile is described by a waveform that has a range of frequency components: high frequency or short wavelength components are assumed to describe the *roughness* of the sample; low frequency or long wavelength components are related to more gradual changes and describe *waviness* or *form* of the profile (Thomas, 1999). The roughness can be considered to be superimposed on the waviness of a given surface. There are several methods for calculating the roughness. For engineering applications, a rapid, averaging method is commonly used to classify entire surfaces. The surface average roughness (R_a) is the integral of the absolute value of the roughness profile (the roughness value along a given line) relative to a mean line (*e.g.*, Figure 23 a), divided by the evaluation length (ISO, 1997). It is calculated relative to a mean reference line, which is created after filtering roughness and waviness components from the profile under investigation. The filter uses a least-squares fit to determine the reference mean line, followed by separation of the short-wave component from the long-wave component. R_a is defined as:

$$R_a = \frac{1}{L} \cdot \int_0^L |r(x)| d(x) \qquad [1]$$

Where, r is the 2-D vertical cross-sectional area along incremental distance x of the measured profile of total length L; r is calculated by integrating the absolute value of the profile height (z-axis direction) as a function of distance along the profile (x-axis or y-axis direction) relative to the mean profile height. Here, R_a was calculated from digital elevation models (DEMs) generated using SEM stereology.

6.3.3. SEM imaging and stereogrammetry methods

SEM imaging was carried out on several samples from the Bezymianny PF deposits including both ash and blocks. The exact samples and sample orientations had been first measured in the TIR prior to their preparation for the SEM analysis. A small portion of each sample was prepared with lateral dimensions of ≤10 mm diameter and a height of 7-8 mm. All samples were fixed to aluminum stubs using a wax adhesive and coated using a gold sputter coater to a thickness of 15 nm. Image quality was enhanced through the application of silver paint between the sample and stub to improve the electrical ground. Homogenous ash particle dispersions for SEM analysis were prepared following a simple approach (O.P. Mills, personal communication, 2006). A small amount of ash was placed adjacent to an aluminum sample stub in a sealed plastic container; each stub had an electrically conductive adhesive coating on its upper surface.

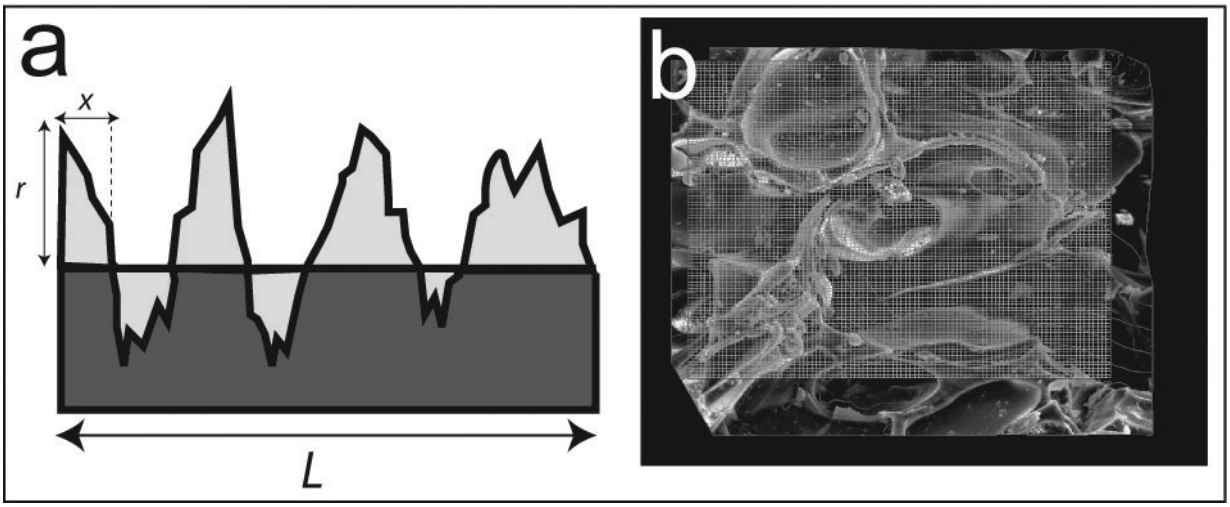

Figure 23 (a) The average surface roughness R_a, is an integral of the absolute value of the roughness profile of length *L*, where *r* is the 2-D vertical cross-sectional area along incremental distance *x* of the measured profile; *r* is calculated by integrating the absolute value of the profile height (z-axis direction) as a function of distance along the profile (x-axis or y-axis direction), relative to the mean profile height. (b) Example of image MTU-2006-004, with 200 horizontal and 200 vertical profile lines overlain (fine lines) to calculate R_a for each sample.

Several short bursts of pressurized gas were aimed at the ash sample through an opening in the top of the container, which dispersed ash particles over the sample stub.

Digital images acquired on a JEOL JSM-6400 SEM at Michigan Technological University were transferred and processed using Alicona Imaging MeX software. Magnification ranging from 12 to 3000 produced horizontal spatial resolutions from 0.009 to 22 μm. The final image magnification of 400 was optimized according to time and hardware constraints, and provided a resolution of 0.183 μm, which was adequate for analyzing the 1-100 μm scale surfaces. Three dimensional characteristics were measured using a stereo-pair of secondary electron images (*e.g.* Podsiadlo and Stachowiak, 1997). Goldstein et al. (1981) provided a detailed explanation of the SEM image retrieval method. SEM images of the sample were captured at a separation angle of 6º (3º from either side of vertical), ensuring that magnification and working distance were held constant. The smallest aperture setting on the instrument (50 μm) was used to create a low convergence angle and the greatest depth of field. Imaging was conducted rapidly to limit sample coating degradation by the electron beam. A DEM was generated from these images and the morphology and surface area were analyzed to quantitatively measure the surface characteristics of each sample.

We analyzed 200 horizontal and 200 vertical profiles to investigate the variation in surface morphology (Figure 23 b) and generated a single numerical R_a value for each sample. The National Institutes of Health freeware/software application *ImageJ* was used to process SEM images (Rasband, 1997). We created binary images that highlighted the vesicles/voids in black (DN = 0) and the glassy sample in white (DN = 255). A threshold level was manually set for each image to highlight the vesicular regions only. To ascertain the uncertainty associated with the manual threshold approach, three images were selected and the threshold was varied to give a

range of reasonable vesicularity estimates for each image. The error margin for this technique was calculated (± 6%), taken from the range between maximum and minimum vesicularity estimates.

A further capability of the SEM image processing software is the creation of DEMs of individual vesicles in order to image their surfaces in 3D. A vesicle edge can be highlighted and the volume measured beneath an artificial plane that connects the edges. To demonstrate this technique, a stereo image pair was acquired from a sample (MTU 2006-008) collected from the January 2005 deposit. This sample consisted of vesicular ash and lapilli, from which a randomly selected single ash particle was imaged (Figure 24). One isolated vesicle measuring ~50 μm in diameter was selected (Figure 24 b). The volume calculated beneath the plane was 12.9 x 10^3 μm^3. Although this specific technique was not used for further analysis in this study, it does present a novel approach to mapping the sub-micron scale topography of vesicle interiors. It also highlights the use of extremely high spatial resolution (nm to μm) DEMs to observe and characterize surface textures on glassy volcanic products. Future work will use these surface maps of individual vesicles together with photon ray-tracing to model the number of wall-photon interactions and the actual emission from an individual vesicle. Such a quantitative model could determine the threshold at which TIR emission spectroscopy becomes significantly impacted by micron-scale roughness.

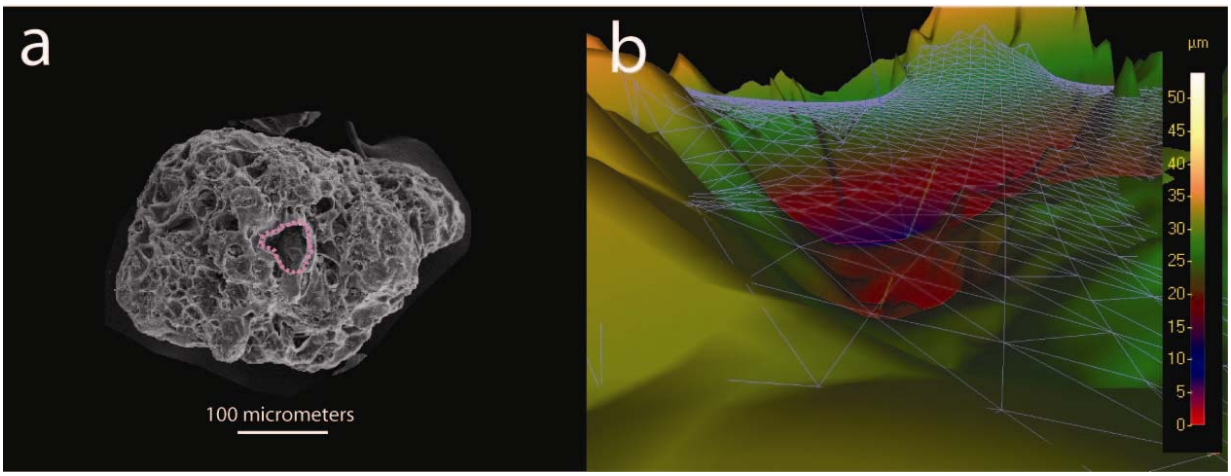

Figure 24 (a) SEM image of a single ash particle taken from sample MTU-2006-008. Pink dashed line delineates a single vesicle on the surface. (b) High magnification view of vesicle interior with blue mesh lines showing the upper plane of the vesicle.

6.3.4. TIR emission spectroscopy background

TIR remote sensing and laboratory spectroscopy provides a non-destructive, quantitative means to collect information on the temperature, chemistry, and texture of a surface/sample. The TIR radiance of a sample/surface is a function of the wavelength-dependent emissivity (ε) and the brightness temperature of that surface. These must be separated in order to analyze the emissivity spectrum (*e.g.* Realmuto, 1990). In a five band image (*e.g.* ASTER TIR) for example, there will be six unknowns: five emissivity values and one brightness temperature. Thus, an under-determined set of equations is produced making an assumption necessary (*e.g.*, the emissivity in one of the wavelength bands) in order to solve the set of Planck equations (*e.g.* King et al., 2004). The derived emissivity spectrum can be used to determine: (1) the material composition (*e.g.* Lyon, 1965; Christensen et al., 2000) or (2) the surface textures such as roughness and degree of glassiness (Crisp et al., 1990; Ramsey and Fink, 1999; Byrnes et al., 2004; King et al., 2004; Carter et al., 2006).

The spectral features of most mixtures are assumed to be linearly proportional to the areal abundance of the mixed end-members (*e.g.* Adams et al., 1986; Thomson and Salisbury, 1993). Following this assumption, a linear, least-squares algorithm, in combination with a library of likely end-member spectra generally can be used to identify the spectral components of a mixture and derive their abundances, hence the deconvolution or unmixing of spectra. This approach has been widely-used for compositional analysis both in the laboratory and from space (Ramsey and Christensen, 1998; Christensen et al., 2000; Hamilton and Christensen, 2000). However, a potential complication to this approach using laboratory-derived end-members applied to satellite-based remote sensing is common reduction in spectral contrast of the latter as compared to the same linear mixture of end-members from the laboratory. This phenomena has been

studied by several authors and is caused by a combination of factors including incomplete atmospheric correction for the direct (up-welling) energy; the reflected (down-welling) energy; scattering of emitted energy from smaller (< 50 μm) particles on the surface; the "cavity effect" of surface micron-scale roughness; and/or reflected side-welling energy from other surface features/particles. To first order all these processes result in an additive effect of some percentage of featureless blackbody energy, which can be simply modeled and removed in the deconvolution approach (Hamilton and Christensen, 2000; Kirkland et al., 2002; Moersch et al., 2002).

Previous studies have also applied this approach using only obsidian glass and a blackbody as end-members. Vesicles on glassy lava flows act as near-blackbody emitters, because emitted photons within these cavities commonly undergo multiple interactions with the vesicle walls before reaching the detector (Ondrusek et al. 1993; Ramsey and Fink, 1999; Ramsey and Dehn, 2004). The combined emitted and reflected components of these multiple interactions serve to reduce the spectral contrast in a linear manner proportional to the micron-scale roughness (Ramsey and Fink, 1999). Thus, the spectral contrast was used to define a quantitative estimate of the percentage of surface vesicularity (*i.e.*, a smaller contrast suggesting a greater vesicularity and vice versa). Ramsey and Fink (1999) constructed an algorithm capable of creating a map-based estimate of surface vesicularity, which was validated with field maps and SEM images of cross-sectional cuts through the surface of the various pumice textures.

This was documented by Ondrusek et al. (1993) and expanded into a viable, quantitative modeling approach for the glassy lava flows and domes of Medicine Lake Caldera, CA (Donnelly-Nolan, 1988; Ramsey and Fink; 1999). Samples studied included an obsidian, finely vesicular pumice and coarsely vesicular pumice. The absorption depth (or spectral contrast) of

the primary Si-O Restrahlen band decreased with increasing vesicularity and is detectable in the relatively clear 8-12 μm region corresponding to the Earth's TIR atmospheric window.

Ramsey and Dehn (2004) expanded the same approach to space-based TIR data collected over an active lava dome (Bezymianny). However, complications arose on the dome due to small-scale (sub-pixel) thermal heterogeneities, surface mineral deposits, and fumarolic degassing, all of which have effects on the integrated TIR emission spectrum from any given pixel on the domes surface. They did show that the technique was still a valid approach to map detectable changes in surface roughness of the lava dome. For this work, we use the same binary modeling approach previously used for lava flows and domes, and test the hypothesis that it also could be used on ash-rich pyroclastic flow (PF).

6.3.5. Laboratory TIR spectroscopy methods

Bezymianny samples were prepared for Fourier-Transform Infrared (FTIR) thermal emission spectroscopy (Christensen et al., 2000; King et al., 2004), following the approach used in Ruff et al. (1997). Emission spectra of the samples were collected at the Thermal Emission Spectroscopy (TES) Laboratory at Arizona State University and Image Visualization and Infrared Spectroscopy (IVIS) Laboratory at the University of Pittsburgh. At both laboratories a Thermo-Nicolet Nexus 670 FTIR spectrometer with a temperature stabilized Deuterated Triglycine Sulfate (DTGS) detector was uses to collect the TIR spectra. The spot size for each spectrometer was approximately 2 cm. However, the IVIS Laboratory uses a potassium bromide (XT-KBr) beamsplitter with a spectral range of 5-25 μm, whereas the TES Laboratory uses a Caesium Iodide (CsI) beamsplitter extending the range to 50 μm. The spectra of temperature-

stabilized precision blackbodies were first acquired and used to calibrated the instrument response function (Ruff et al., 1997). The blackbodies and subsequent samples are placed in an environmental chamber is purged with air, which is scrubbed of water vapor and carbon dioxide in order to minimize spectral features from this TIR-active gases.

Prior to analysis, each sample was heated to 80 ºC in order to provide adequate thermal energy above the background energy of the laboratory. The warm samples were placed in the chamber and data collected for 256 scans (~ 9 minutes), which averaged for higher signal to noise. For the coherent, lithic block samples (-004 and -005), small sample surfaces measuring approximately 40 mm wide by 20 mm thick were carefully chipped from a larger block. For the ash–lapilli grade sample (-001), approximately 2 g of ash filled one sample cup.

6.3.6. ASTER data collection

ASTER acquires image-based data of reflected and emitted energy in the visible/near infrared (VNIR) region in three wavelength channels (0.56 – 0.81 μm) at 15 m/pixel spatial resolution, in the SWIR region in six wavelength channels (1.65 – 2.40 μm) at 30 m/pixel spatial resolution, and in the TIR region in five wavelength channels (8.29 –11.32 μm) at 90 m/pixel spatial resolution (Yamaguchi et al., 1998). The raw image data are corrected for geometry and image registration and later processed in on-demand, level 2 (L2) products such at-ground TIR radiance, brightness temperature, and surface emissivity (Abrams, 2000). For this study, the ASTER TIR L2 emissivity product was used and spectra extracted from an image acquired on 20 August 2005 at night (local time). The emissivity spectra from the pixels that corresponded to the location of the field samples and surveys were used for this analysis.

6.4 RESULTS

6.4.1. Thin section analyses

The mineralogy and surface texture was investigated using standard petrographic thin sections for samples -004, and -005. For sample -001, ash was impregnated with a resin before being prepared for thin section analysis. The primary aim was to assess the sub-millimeter-scale mineralogy and analyze the surface texture and vesicularity.

Sample -001 was hypocrystalline and glomeroporphyritic, with crystals of plagioclase, hornblende (Hb), and clinopyroxene (CPX), including iron-rich alteration products, set in a glassy matrix that was prevalent throughout the samples. Crystals were inequigranular, present as phenocrysts and within crystal aggregates that displayed reaction textures, such as coronae and alteration products. Many Hb crystals could also be seen embedded within plagioclase laths and crystals. CPX (11%) crystals were mostly inequigranular, anhedral and degraded, some showing skeletal textures. Spherical vesicles were visible, commonly occupying the space between crystals. Sample -004 was hypocrystalline and porphyritic in thin section. The sample was highly vesicular and composed of discrete phenocrysts of plagioclase, Hb, and CPX was set in a glassy matrix. Qualitatively, sample -004 displayed a far higher vesicularity than sample -001 visible at this resolution. Sample -005 was similar in texture, mineralogy, and vesicularity to sample -004 as they were from the exterior and interior of the same pyroclastic block, respectively. At the magnification available, micrometer-scale vesicles were too small to be investigated, calling for the use of SEM images at a much higher magnification.

6.4.2. SEM image-derived vesicularity and R_a results

After averaging the surface roughness profiles of 200 horizontal and 200 vertical profiles, a single R_a value was derived for each sample (Figure 25, Table 8). A range of R_a values from 0.9 to 2.8 μm were measured. The highest surface roughness value (2.8 μm) was associated with sample -004 and agreed with visual estimates. The least rough surface (0.9 μm) was from sample -001-P4, which contained a small (300 μm long) ash particle. The particulate ash and lapilli samples revealed textural heterogeneities in the 14 March 2000 deposit ranging from 0.9 to 1.3 μm, whereas the coherent block samples from the 11 January 2005 eruption produced R_a values of 1.6 to 2.8 μm for the block interior and surface, respectively.

The range of R_a values correlated well with SEM image-derived vesicularity values, which were calculated by using an average of both SEM binary image pairs (acquired at -3° and +3° off nadir). The percentage surface vesicularity was calculated for each sample and ranged from 18 % to 26 % (Figure 26). The particulate ash and lapilli samples from the 14 March 2000 deposit had a vesicularity range of 18 to 20 %. Comparison of the image-derived vesicularity results to those of the R_a results produced correlation value (R^2) of 0.979 for all samples.

Table 8 Image-derived surface vesicularity and R_a values.

Sample number	SEM image resolution (μm)	Magnification	Image-derived vesicularity (%)	R_a (μm)
MTU-2006-001-P1	0.1833	400×	20	1.3
MTU-2006-001-P4	0.1833	400×	18	0.9
MTU-2006-004	0.1833	400×	26	2.8
MTU-2006-005	0.1833	400×	22	1.6

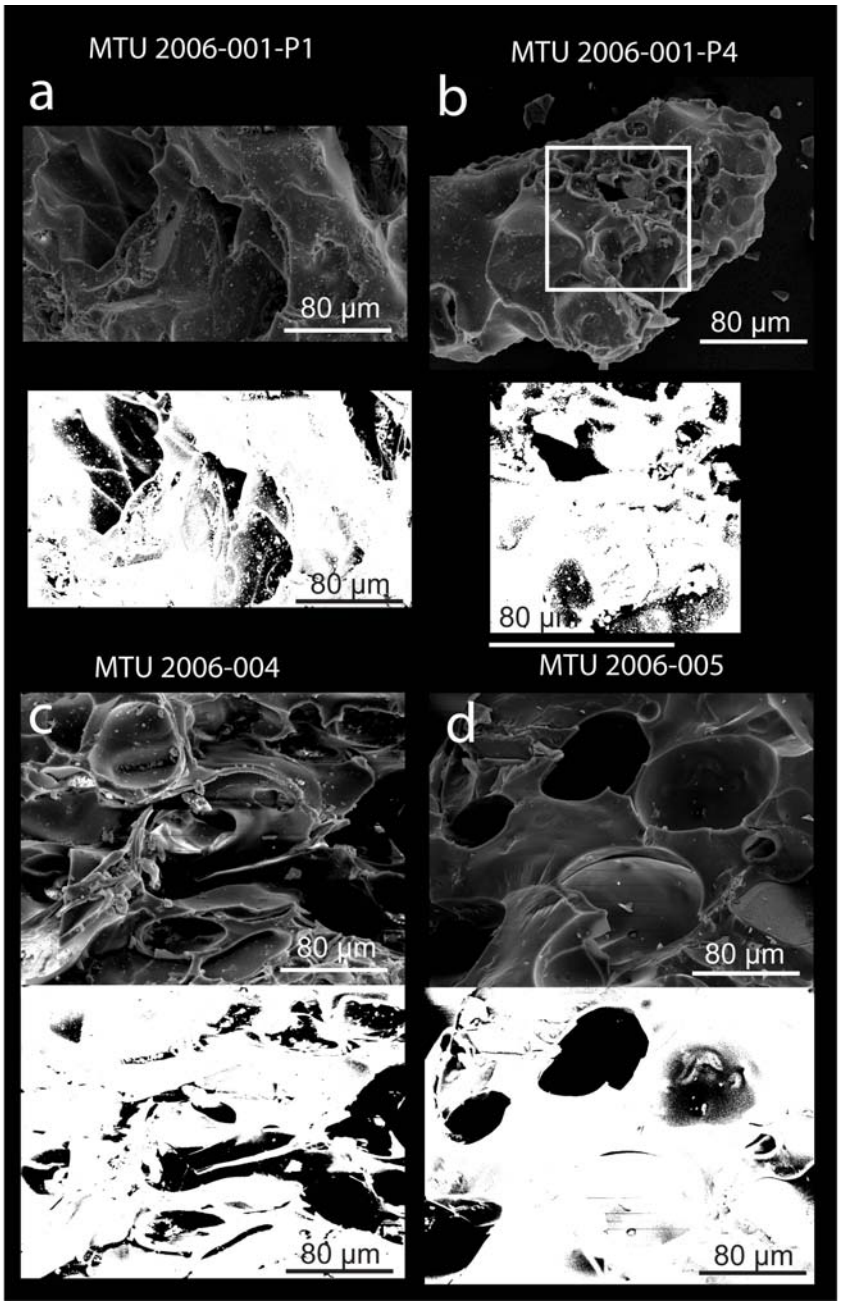

Figure 25 SEM images of the Bezymianny samples and binary (black and white) image below each sample. All images were taken at 400× magnification and scale bars are 80 µm wide (horizontal white lines on SEM images). (a) MTU-2006-001-P1. (b) MTU-2006-P4. (c) MTU-2006-004. (d) MTU-2006-005.

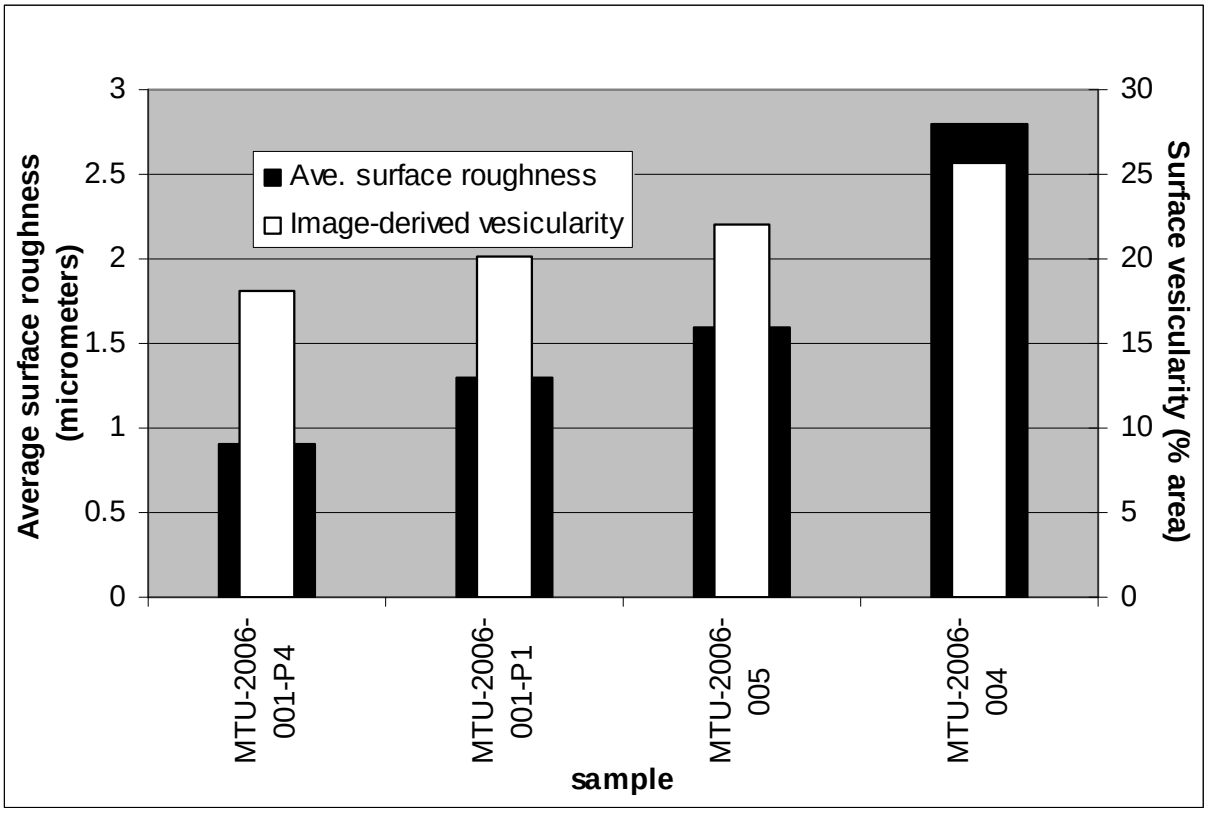

Figure 26 Image-derived surface vesicularity values calculated using image processing software for the Bezymianny samples (see Figure 25 for SEM and binary images) compared to average surface roughness (R_a) values for each sample derived from averaging 400 roughness profiles. A positive correlation between the (R_a) values and image-derived surface vesicularity can be seen.

If sample -005 (the block interior, which was not a dominant surface component) were removed from the analysis, the correlation value increases to 0.998. Using the terminology of Houghton and Wilson (1989), image-derived vesicularity estimates showed that samples -001-P1 and -001-P4 were incipiently vesicular (5-20%), whereas the other two samples (-004, and -005) were poorly vesicular (20-40%).

6.4.3. TIR spectroscopy results

We used the two end-member approach of Ramsey and Fink (1999) to deconvolve the TIR emission spectra of each sample. The two end-members were a high-SiO_2 obsidian and an artificial blackbody (Figure 27). All the laboratory spectra of the samples had a similar morphology to the obsidian spectrum and fell within the range of the two end-member spectra indicating that they were likely a linear construct of the two end-members. Thermal emission spectroscopy data were collected for the coherent block particles -004 (Figure 28), -005 (Figure 5), and particulate sample -001 (Figure 29).

The samples in order of smallest spectral contrast and therefore those predicted to be the most vesicular (*i.e.* have the most blackbody component) were -001, -004 and -005, respectively. The deconvolution-derived vesicularity estimates for these samples were 77%, 73% and 54% (Table 9). A similar laboratory-derived vesicularity estimate was observed between the ash (-001) and exterior block sample (-004).

Table 9 Laboratory spectral deconvolution results.

Sample number	Block/ particulate	% blackbody (surface vesicularity)	Total % summation	Root mean squared (RMS) error
MTU-2006-001-P1	Particulate	77	99.38	0.0087
MTU-2006-001-P4	Particulate	77	99.38	0.0087
MTU-20006-004	Block	73	99.6	0.0049
MTU-2006-005	Block	54	99.61	0.0059

The error of this approach for deconvolving laboratory emission spectra is approximately 5% (Ramsey and Christensen, 1998; Ramsey and Fink, 1999). However, in order to assess the accuracy of fit of the two end-members, two related statistical errors can be examined. The first is the wavelength-dependant residual error (the measured spectrum minus the modeled spectrum), which shows regions of the spectrum that are not well-modeled (Figure 28 and Figure 29). The root mean squared (RMS) error is a single value for each model result and is in effect an average of the residual error over the entire wavelength. The RMS error is an accepted value for any least-squares modeling approach and has been well-used for the last two decades where reporting the results of spectral deconvolution models. It is true that there can be situations where the RMS error is affected by large changes in spectral contrast. One could be mislead for example where comparing a laboratory-derived RMS error to that of a satellite-based RMS. However, for the case where all samples have similar spectral contrast, as well as for a binary end-member system (both of which apply here), the RMS and the residual errors correlate. In other words, either of these errors are valid in assessing the goodness-of-fit of a particular model result. For the samples analyzed here the RMS errors were all <0.01, suggesting a generally-good model fit. We also show the best (Figure 28) and worst (Figure 29) case residual error results, which range from 0 to 2.5% within the residual error results.

6.4.4. Satellite-based TIR spectra of the surfaces sampled

Although the remote sensing data is not a major focus of the work presented here, the larger ultimate goal is to be able to place accuracy assessments on the use of ASTER data (or another future TIR instrument) to map recently-emplaced PF deposits at volcanoes around the world.

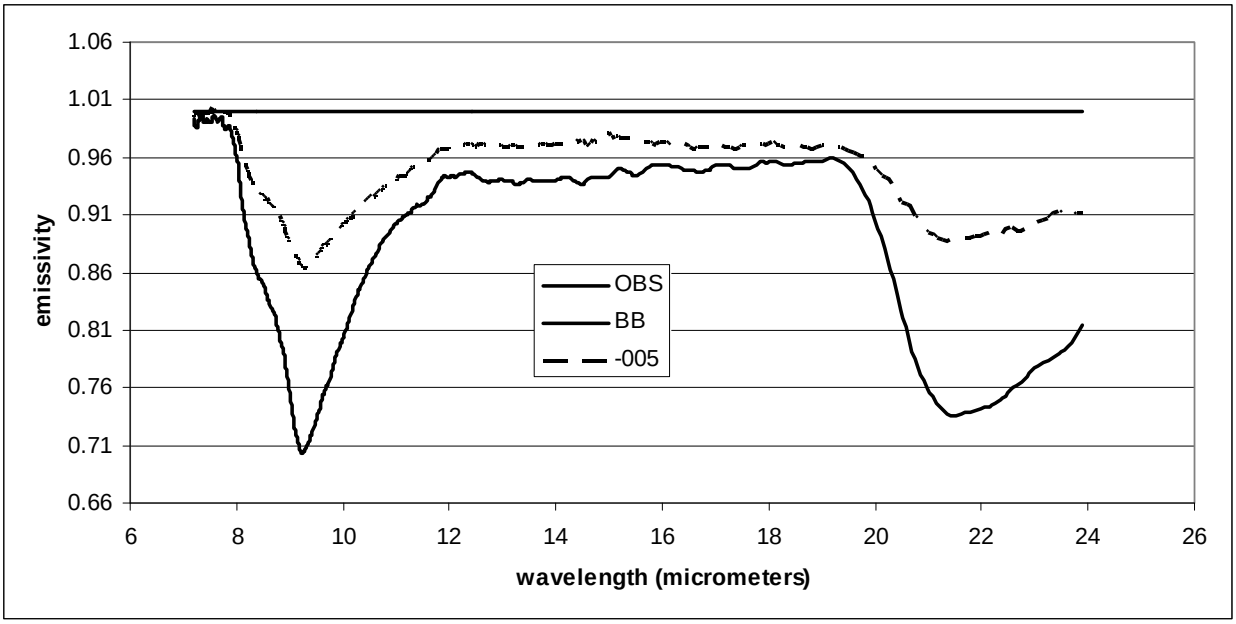

Figure 27 Laboratory thermal infrared (TIR) emission spectra of the two end-members used in this study: an obsidian (OBS) and blackbody (BB). Sample -005 is displayed as an example, fitting between the two end-members.

Five-point ASTER emissivity spectra were extracted for two pixels: area 1 from which samples -004 and -005 were taken (dominantly block-covered) and area 2 from which sample -001 was taken (dominantly ash-covered). A spectral emissivity contrast of 0.02 was noted between the two locations, with a greater contrast in area 1 that was dominated by blocks (Figure 30).

Within the ASTER data, radiant energy from the surface was from a mixture of blocks and ash on the surface. In order to compensate for these effects and try to correlate laboratory spectral results with those derived from ASTER, we modified the laboratory spectra of the samples based on the estimates of ground cover. For area 1 and 2 (Table 10) a mixed end-member laboratory spectrum was created using the mapped percentage of blocks and ash. For area 1, a mixed spectrum of 70% of the -004 block spectrum and 30% the -001 ash spectrum was created. Similarly, for area 2, a mixed spectrum of 10 % blocks to 90 % ash was created, again using samples -004 and -001, respectively. Using these end-members as a laboratory-based comparison to the ground cover for areas 1 and 2, the spectral deconvolution model produced vesicularity estimates of 74 % and 77 %, respectively.

6.4.5. Comparison of ASTER-derived and laboratory spectra

Satellite-based (ASTER) TIR data at 90 m/pixel spatial resolution were collected on 20 August 2005 (coincident with the field data collection). The data were atmospherically-corrected and automatically separated into brightness temperature and surface emissivity.

Table 10 Comparison of ASTER deconvolution-derived vesicularity estimates (taken from 20 August 2005) and laboratory- derived estimates over area 1 and area 2.

Area	**1**	**2**
Eruption date	Jan-05	Mar-00
Location (UTM, WGS-84)	6200261.35 m N, 601986.869 m E	6199981.77 m N, 602378.80 m E
Laboratory -derived vesicularity	74	77
ASTER-derived vesicularity	49	62
Surface % blocks	70	10
Surface % ash	30	90

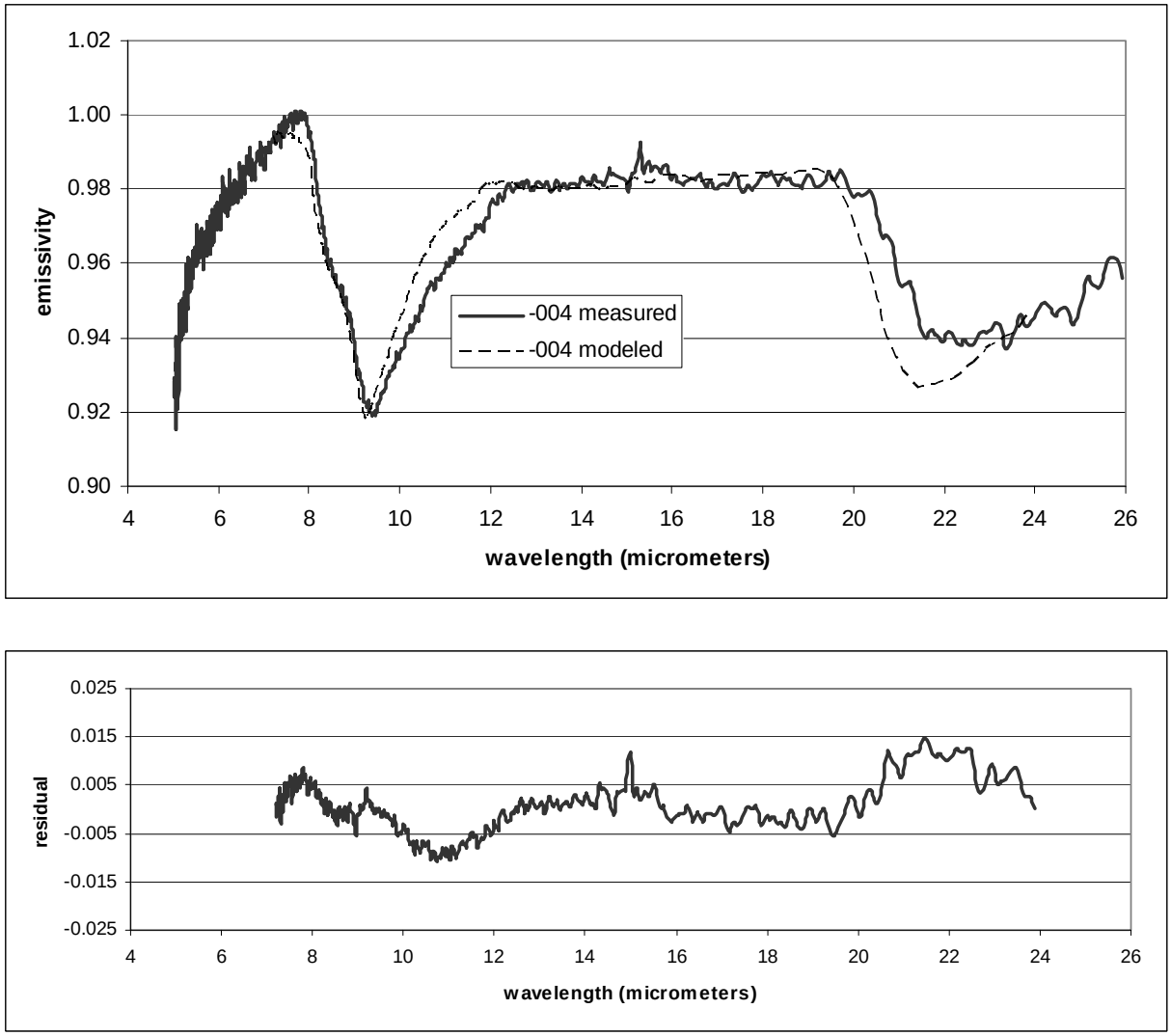

Figure 28 Laboratory emissivity spectra of sample -004, showing the measured spectrum (solid line from 5 - 25 µm) and modeled spectrum (dashed line from 7 – 25 µm). Below is the residual (measured-modeled) error from 7 – 25 µm. Most of the discrepancies are due to noise in the spectrometer and incomplete removal of atmospheric water vapor and carbon dioxide. From 5 – 7 µm, an increased slope in the measured spectrum was observed, indicating particle size effects, likely due to adhered fine particles (< 50 µm) from within the PF deposit on the block surface.

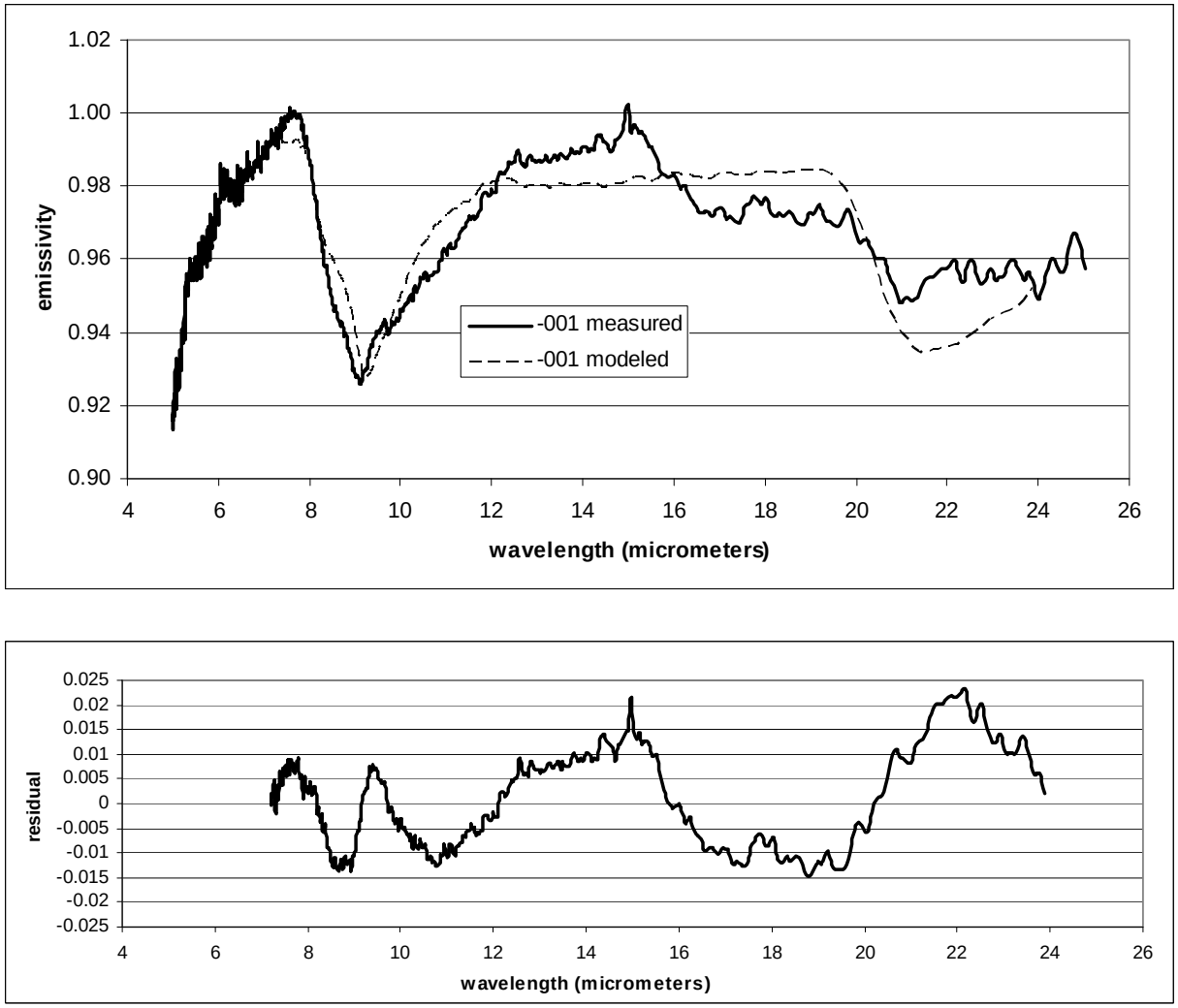

Figure 29 Laboratory emissivity spectra of sample -001, showing the measured spectrum (solid line from 5 - 25 µm) and modeled spectrum (dashed line from 7 – 25 µm). Below is the residual (measured-modeled) error. Compared to sample -001, there are larger discrepancies throughout the residual spectrum although the overall average difference is still very small. As with sample -004, from 5 – 7 µm, an increased slope in the measured spectrum was observed, indicating particle size effects, likely due to fine particles (< 50 µm) in this region.

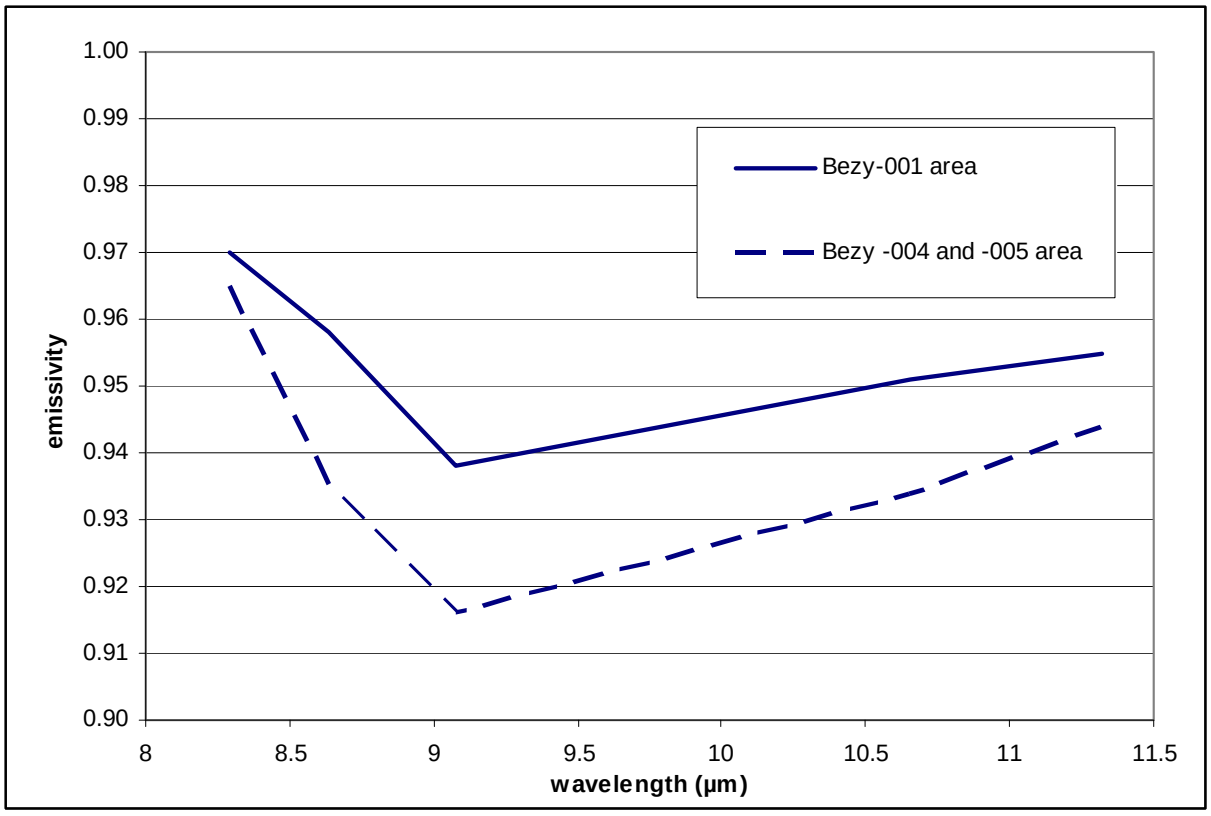

Figure 30 ASTER TIR emissivity spectra for the 90 m pixel taken from the 20 August 2005 ASTER image that contained the ash sample MTU 2006-001 (area 2, solid line) and the 90 m pixel that contained the block samples MTU 2006-004 and -005 (area 1, dashed line). The slight reduction in spectral contrast is expected for fine grained particulate surfaces (as compared to more block-rich surfaces).

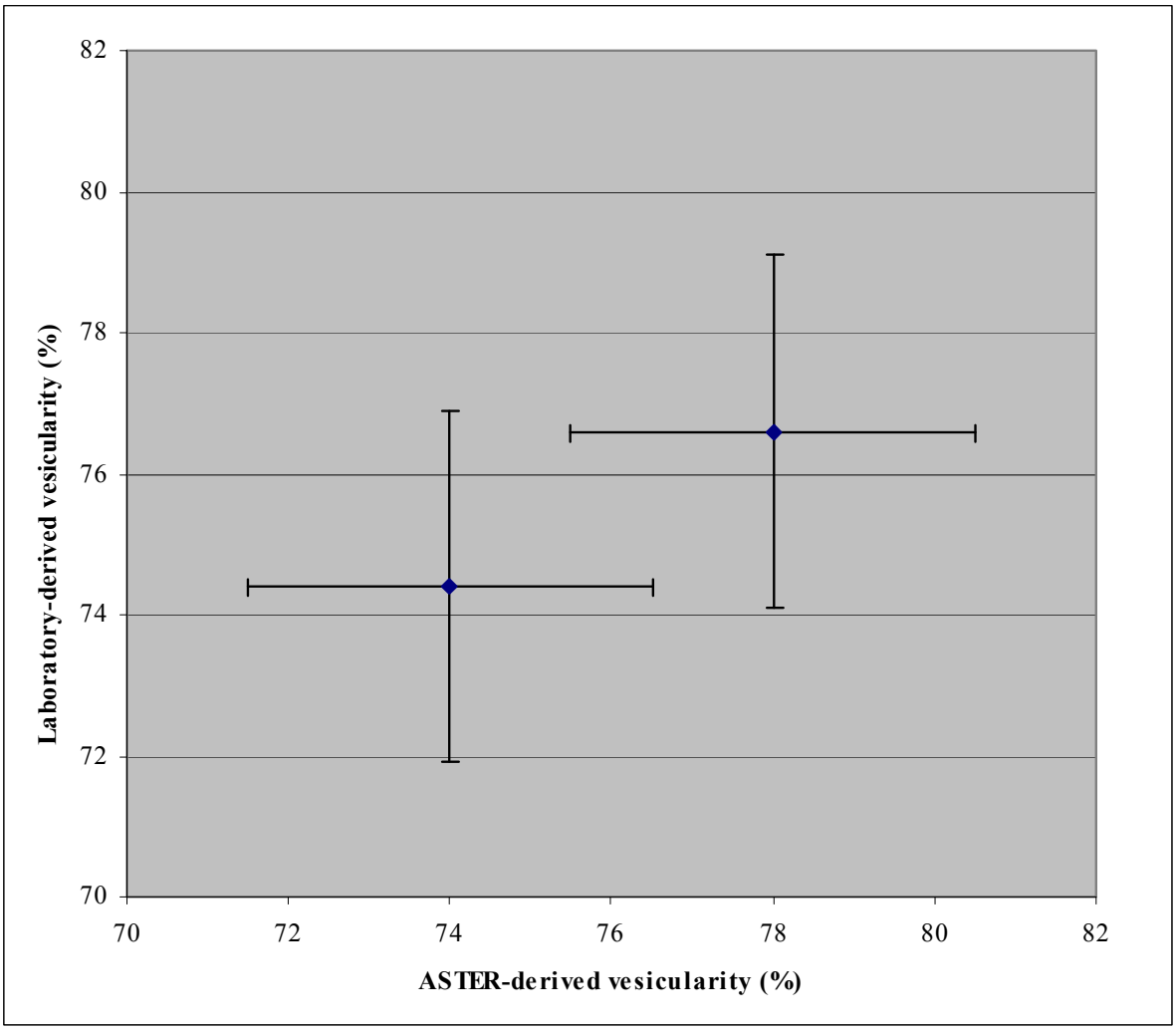

Figure 31 Comparison of ASTER-derived vesicularity results to laboratory-derived vesicularity estimates for area 1 (lower left point) and area 2 (upper right point). To test the effects of the lower resolution ASTER data, the laboratory spectra were degraded to ASTER 5-point resolution. The 5-point spectra were then run through the deconvolution algorithm, producing a maximum difference of 5% with the laboratory-derived results. Thus, an error bar of ± 2.5 % were placed on the ASTER-derived modeled vesicularity results. Based on prior spectral test work (Ramsey and Christensen, 1998), error bars of ± 5% were given for the laboratory thermal emission spectra. A positive correlation was observed between both datasets.

The emissivity spectra for the two field locations were extracted (Figure 30) and visually compared to laboratory-derived spectra over the 8-12 μm region. ASTER-derived emissivity spectra were run through the model and produced vesicularity estimates of 74% and 78% for areas 1 and 2, respectively. This showed a near-perfect (maximum difference of 1%) correlation with the laboratory-derived results (Figure 31, Table 10).

To test the effects ASTER's lower spectral resolution on the deconvolution model, the laboratory spectra of the field samples and end-members were degraded to that of ASTER and the deconvolution model re-applied. The average difference between the laboratory and the ASTER resolution was 2% with the maximum being 5% (Table 11). There was no difference between the laboratory-derived and spectrally degraded data for sample -005, an exact match (54%). Therefore, for the binary deconvolution approach, an error of ± 2.5 % is assumed as the limit for ASTER-derived modeled vesicularity. This value is nearly identical to the results of Ramsey and Christensen (1998). The laboratory-derived and ASTER-derived vesicularity estimates showed a positive correlation when comparing the two datasets (Figure 31).

6.5 DISCUSSION

Thin section analyses were used to assess the general mineralogy and the vesicularity of the samples at that magnification. All samples were characterized by glass and micron-scale roughness elements. The phenocrysts were generally below the areal percentage to be detected by laboratory emission spectroscopy.

Table 11 Comparison of laboratory-derived spectral deconvolution results (in %) to the same spectra that were resampled to ASTER 5 point data and then run through the model. A maximum difference of 5% total was observed (± 2.5%), providing an error bar for the ASTER-derived results.

Sample	Laboratory-derived vesicularity	Laboratory spectra degraded to ASTER 5-point result
MTU-2006-001-P4	77	72
MTU-2006-001-P1	77	72
MTU-2006-004	73	72
MTU-2006-005	54	54

Therefore, although the petrologic information did not have a direct bearing on the TIR or SEM results, it does provide insight into the Bezymianny magma system and the processes ongoing during eruption of the pyroclastic material. The higher magnification SEM data provided a positive correlation between the image-derived vesicularity and R_a roughness values, which must be further tested with larger datasets in the future. Although assumed to be true in past studies (*e.g.*, Ramsey and Fink, 1999), our results confirm the hypothesis that vesicularity increases as micron-scale roughness increases. This was further investigated using 14 more Bezymianny samples in addition to the 4 described here and a positive correlation was observed (Appendix D). These two parameters are linked together as causes of TIR spectral contrast reduction. The spectroscopy results from areas 1 and 2 derived from both ASTER and the laboratory show a positive correlation. In both datasets the more ash-rich area is modeled as being more vesicular. However, the difference between the two field areas was much less for the ASTER data (3%) as compared to the laboratory data (13%). Of importance is that both techniques show the same general trend and that the values are close to the associated uncertainty for each method. The difference in absolute numbers is not surprising considering that that laboratory data were of small areal spot sizes, acquired at high spectral resolution, and collected in an atmospherically-controlled environment. The five-point ASTER data acquired over a 90 m pixel with a model atmospheric correction will always have lower spectral contrast and hence less variation between pixels with variations in ground cover.

The image-derived vesicularity results from the SEM analysis for samples -004 and 005 (26% and 22%, respectively) were substantially lower than the TIR-derived spectroscopy estimates (*e.g.*, 73% and 54%, respectively for the laboratory data). We interpret this discrepancy as being caused be several factors. First and most significantly, the spectroscopy-derived results

were over-estimated due to the high spectral contrast of the obsidian end-member, relative to the spectra of the samples collected. This end-member has a deep (emissivity minimum of 0.68) spectral band at 9 μm (Figure 27) compared to any spectrum from the Bezymianny samples. In a binary deconvolution model, this has the effect of over-estimating the blackbody results and hence the TIR-derived vesicularity values. Secondly, using pure rock or mineral spectra as end-members can be problematic for modeling particulate or fine-grained samples, such as the ash-dominated PF surfaces. In studies where spectral contrast is not as critical (*e.g.*, compositional as opposed to textural mapping), a blackbody end-member is commonly added as another end-member to account for spectral contrast differences between the library end-members and the mixed spectrum. The resulting blackbody end-member percentage can be used as a proxy as to the amount of spectral contrast reduction in the mixed spectrum perhaps indicating the level of atmospheric contamination, the particle size on the surface, or the degree to which "self shadowing and re-emission" is present from rough surfaces. However, in most cases this blackbody end-member is removed and the results of the other end-members corrected by normalizing their values so their new totals will sum to 100%. This has worked well for TIR compositional mapping on Mars using a deconvolution approach and a spectral library of mineral end-members with deep spectral contrasts (Bandfield, 2002; Hamilton et al., 2003).

However, this approach is clearly impossible for a study where the blackbody end-member is the key result being the proxy for surface roughness. For previous studies, the glass end-member used was being compared to similar glass dome rocks and therefore the spectral contrast differences between library and mixed data were negligible. Because the spectral depth of the glass end-member is critical to results of such a modeling approach, ash-rich particulate surfaces are always going to be overestimated in their TIR-derived vesicularity. Thus, future

work would benefit from the selection of a glassy end-member for PF deposits that can be used to produce more realistic vesicularity estimates. To first order, the current glass end-member could be reduced in spectral contrast artificially to more closely match the results of the SEM data. However, this ad-hoc approach was not presented here as the authors feel those results, while being more in line with the SEM results, need to be further validated on other PF surfaces with a much larger array of field samples.

The laboratory TIR spectral data (see section 6.4.3.) showed a similar spectral morphology and contrast between the ash sample (-004) and the PF block exterior (-004). This was not expected as the block interior (-005) had a much glass-dominated spectral signature (i.e. a greater spectral contrast and therefore a lower vesicularity). We interpret the spectral-similarity of the ash and the exterior of the block as being due to fine particulates adhering to the block surface and in-filling some of the voids. These small fragments were also seen in the SEM images of sample (-004). These fines were likely produced during transport down slope, subsequent eolian transport of the ash onto the block, and/or minor contamination during transport of the block from the field to the laboratory. This contamination by fines has the effect of lowering the spectral contrast and thus increasing the estimated vesicularity results. Therefore, although the sample -005 was not a dominant surface type, it may provide a more realistic end-member for future investigations of block-rich PF deposits.

These data, in combination with field investigations from August 2004 and August 2005, provide information on the possible eruption style of the March 2000 and January 2005 eruptions. The March 2000 PF deposit was ash-dominated and deposited over a greater area and longer distance than the January 2005 deposit (Ramsey and Dehn, 2004). Although the March 2000 eruption column was reported to be relatively low (~8 km), based on analysis of the deposit

we interpret the column as having been relatively gas-depleted, and the PF deposits having been formed by a boil-over style column collapse. In contrast, the January 2005 deposit surface was composed of almost entirely blocks (e.g. Figure 22). The travel distance was shorter and the areal extent smaller than the March 2000 deposit. Based on this and in combination with additional TIR data (Carter et al., 2007a), we interpret the eruption style was different than in 2000, with the 2005 PF deposit being created primarily from a partial dome collapse and would therefore be termed a block and ash flow.

6.6 CONCLUSIONS

A clear positive correlation was demonstrated between image-derived vesicularity and R_a values in PF deposit samples from Bezymianny. Using the image-derived vesicularity estimates as the predicted ground-truth, we interpret that the block samples (-004 and -005) were the most vesicular, relative to the ash sample (-001). Therefore, a PF deposit covered entirely with blocks would produce a more realistic set of laboratory- and satellite-derived results for the reasons explained above and an ash-dominated deposit must be more carefully analyzed. Micron-scale roughness that is not attributed to vesicularity, combined with particle size effects, may be a key factor in ash samples, hence reducing the spectral contrast (and increasing the vesicularity), while image derived estimates predicted lower surface vesicularities in the ash sample. Care must therefore be taken when interpreting spectral contrast reduction using satellite- and laboratory-derived data.

We have shown spectral deconvolution-derived vesicularity estimates using PF deposit samples for the first time and interpreted that a column-collapse produced the ash rich PF deposit from March 2000 and that a dome collapse generated a block and ash flow deposit in January 2005. A greater number of samples are required to build on these initial results. However, we clearly demonstrated the utility of comparing multiple datasets and their inter-relationships from the micron- to the tens of meters-scale. This work can now be further tested and refined in future work using samples from the 2005-2007 PF deposits at Bezymianny volcano (Carter et al., 2007; Carter et al., 2008) or other volcanic systems. This work outlines the factors that must be considered when analyzing quantitative remote sensing-derived datasets over PF deposits and provides a framework for future investigations at other rapidly changing, active volcanic surfaces.

7 CONCLUDING REMARKS AND FUTURE DIRECTIONS

TIR data have been collected and interpreted over scales of several orders of magnitude. Carter et al. (2007a. Chapter 3) demonstrated the use of 17 ASTER images combined with FLIR and field data to analyse the 11 January 2005 eruption. From these data, the post-eruption emplacement of a PF deposit was observed and two short lava lobes at the summit. Following this, a collapse crater was created, with a DEM-derived volume estimated at between 2.6 x 10^6 $m^3$and 10.7 x 10^6 m^3 formed. The hypothesis that the collapse crater may have partially blocked the upper conduit (promoting a pressure build up) was potentially validated when a larger than normal (15 km altitude ash column) eruption occurred in May 2006. This provides an example of the direct use of TIR observations in eruption monitoring and prediction of future events, especially in an area where, during winter, access to the field area is extremely challenging.

Carter et al. (2008a. Chapter 4) provided a comprehensive account of the 24 December 2006 eruption at Bezymianny, using field-based, SWIR, and TIR observations. A PF deposit was emplaced that was 6.5 km long, observed by photographs, VNIR, and TIR data. A clear pre-cursory signal was detected in SWIR and TIR data four days prior to the eruption, which was the first ASTER-based data to show a thermal increase prior to an eruption at Bezymnianny. In addition, high temperatures were detected where the PF changed direction (building a levee of blocks) and at the PF terminus where blocks accumulated. TIR data was used to make a pre-field investigation hypothesis that the blocks would be concentrated in these areas, due to high

thermal inertias (relative to the surrounding ash-grade material), which was later confirmed in the field. Simple modelling of the a thermal anomaly on the lava dome estimated temperatures of 300 – 700 °C for the magmatic fraction of a SWIR pixel, if it covered $1m^2$ of a 30 m resolution SWIR pixel. Even if the area was as large as 10 m^2, the hot fraction would range from 180 °C to 500 °C, suggesting the thermal activity was caused by hot cracks in a lava lobe surface and not fumaroles. Thus, thermal modelling using SWIR data assisted in the prediction of summit magmatic temperatures following an explosive eruption, which was consistent with past observations of the emplacement of a lava lobe following the eruption. This was later confirmed by field observations. Carter et al. (2007a; 2008a) provided accounts of explosive eruptions that occurred in sub-zero temperatures, and in the case of December 2006, at night. Such conditions are conducive to remote sensing-based investigations followed by limited field work, where available.

Carter and Ramsey (2008a. Chapter 5), and Carter and Ramsey (2008b) analysed a large ASTER dataset (14 months) to consider eruptions over the 2006-7 period. Three explosive eruptions (24 December 2006, 11 May 2007, and 14 October 2007) created three overlapping PF deposits on the southeastern flank, which was mapped using photographs, but an enhanced image of their spatial footprint and internal heterogeneity was observed using a composite TIR image. The 11 May 2007 PF deposit was mapped in detail in the field in August 2007, with seven ASTER TIR (90 m) pixels investigated from 2 – 6 km from the summit. High temperatures were observed in thermocouple, ground-based FLIR, and ASTER data, at 4.5 – 5.5 km from the summit. In addition, analysis of the proportion of blocks relative to ash in each pixel showed an increase in the concentration of blocks in the main body of the PF deposit, (3 -5 km from the summit). This, combined with the thermal data, suggested that the main body of the PF

deposit was of greatest thickness in this area, and of a higher block concentration, relative to the proximal and terminus parts of the PF deposit. FLIR and thermocouple data was used to suggest that post-emplacement cooling had occurred at the PF terminus, as temperatures decreased with distance from the dome. However, ASTER temperatures from 30 June 2007 showed a slight increase with distance from the dome. The PF was emplaced on to snow in the terminus region, suggesting progressive cooling may have occurred in this area. Thus, combined TIR and field-based observations were used to argue that the 11 May 2007 PF had a thicker, block-rich centre, followed by a more gradational, ash-rich terminus, when compared to other PF deposits (*e.g.* 24 December 2006 PF).

Carter et al. (2008b. Chapter 6) compared thin sections, SEM-derived image data, average surface roughness (R_a) values, and laboratory- and ASTER-derived TIR spectra using samples from the March 2000 and January 2005 PF deposits at Bezymianny. This was the first recorded study of TIR spectral deconvolution results over PF deposits. Although assumed to be true in past studies (*e.g.*, Ramsey and Fink, 1999), the results confirm the hypothesis that vesicularity increases as micron-scale roughness increases. Image-derived estimates showed the block samples to be the most vesicular, which was considered to be correct. However, spectroscopy results predicted that the ash had the highest vesicularity. This was attributed to an increase in non-vesicular micron-scale roughness that predominantly affects unconsolidated ash, and particle size effects that dominated the ash and ash-covered PF blocks. Based on field data and the acquired results, it was interpreted that the March 2000 PF deposit was produced as a result of a boil-over style column collapse that was dominantly ash-rich. The January 2005 deposit was interpreted to originate from a dome collapse event that produced a block-dominated block and ash flow. Therefore, this comparative study of multiple datasets was used to interpret

two distinctly different eruption mechanisms, based on a detailed analysis of the emplaced PF deposits.

This work demonstrates the utility of integrating remote sensing observations at multiple wavelengths (VNIR, SWIR, TIR regions) with field observations at several scales. Specifically, it is of use to: (1) hazard mappers studying volcanic regions who want to characterize surface types and the emplacement of pyroclastic flows; (2) field volcanologists looking at PDC deposits (cooling times, mixing with other deposits, distribution of blocks) from dangerous dome collapses that are difficult to access in the field and collect samples from; and (3) remote sensing scientists who may not have access to field data and are attempting to verify satellite- or airborne-derived data. Therefore, this work provides a platform for future remote sensing / field studies for active volcanic targets.

Future work will be carried out to build on this investigation. In particular: (1) a continued collection of ASTER data over Bezymianny, and other volcanoes in the North Pacific region, will assist in providing a comprehensive archive of multispectral, moderate resolution data. Rapid response data will also be used in combination with AVHRR to predict and monitor future events. Bezymianny, at the time of writing (July 2008), may be preparing for another explosive eruption (O. Girina, personal communication, 2008). Each eruption is capable of producing an ash cloud up to 15 km in altitude which can pose a threat to trans-Pacific air traffic, therefore KVERT, AVO, and the University of Pittsburgh must continue to provide timely information on possible events. (2) Future field work to investigate recent (*e.g.* 14 October 2007) PF deposits, with a focus on the difference between the more juvenile, fresh PF that travelled 6.4 km from the dome, and the collapsed dome material deposit that travelled 3.6 km, the latest deposit on the southeast flank. (3) A comparative study with lower spatial resolution, higher

temporal resolution satellite-based data (*e.g.* AVHRR, and MODIS) could be used to investigate the onset of eruptive events, with a much greater number of images available (*i.e.* several per day). (4) Continued testing of the interaction between SEM image-derived vesicularity, average surface roughness on the micrometer scale, and TIR spectroscopy, using a larger data set, is planned. This work may elucidate further information on the micrometer-scale roughness of vesicular materials. (5) Expansion of the project to other target volcanoes, such as Colima (Mexico), or Mount Saint Helens (USA), the latter of which sharing many similarities with Bezymianny. Future work may provide important information on the build up to explosive eruptions, or the post emplacement characteristic of fresh pyroclastic flow deposits, both of which are important factors for the aviation industry, government agencies, and the volcanological community worldwide.

APPENDIX A

ASTER DATA PRODUCTS

Level	Product	Description
1A	Radiance at sensor	Image data plus radiometric and geometric coefficients. Data are separated by telescope
1B	Registered radiance at sensor	1A data with radiometric and geometric coefficients applied
1AE	Radiance at sensor	Expedited L1AE data product created from ASTER Expedited Level-0. Image data plus radiometric and geometric coefficients. Data are separated by telescope
1BE	Registered radiance at sensor	Expedited L1BE data product created from ASTER Expedited Level-1AE. 1AE data with radiometric and geometric coefficients applied
2	AST06 Decorrelation stretch	Enhanced colour composites for each telescope
2	AST04 Brightness temperature	Radiance at the sensor converted to temperature
2	AST09 Surface radiance-VNIR, SWIR	Radiance corrected for atmospheric effects
2	AST09T Surface radiance-TIR	Radiance corrected for atmospheric effects
2	AST07 Surface reflectance-VNIR, SWIR	Derived from surface radiance with topographic corrections
2	AST08 Surface kinetic temperature	Temperature-emissivity separation algorithm applied to atmospherically corrected surface radiance data.
2	AST05 Surface emissivity	Temperature-emissivity separation algorithm applied to atmospherically corrected surface radiance data.
2	AST13. Polar Surface and Cloud Classification	Classifies each pixel of polar scenes into one of eight classes: water cloud, ice cloud, aerosol/dust, water, land, snow/ice, slush ice, and shadow.
3	AST14 Digital elevation model	DEM produced by stereo correlation of nadir and aft Band 3 data
	- Relative DEM	Created only from 3N and 3B data

APPENDIX B

ASTER TIR BAND SCALE FACTORS USED

Band	Scale factor
10	0.006882
11	0.00678
12	0.00659
13	0.005693
14	0.005225

URL:

http://asterweb.jpl.nasa.gov/content/03_data/01_Data_Products/RN_surface_leaving_radiance-TIR.htm

APPENDIX C

ABSTRACTS REFERENCED FROM PROFESSIONAL MEETINGS

Carter, A.J., Ramsey, M.S., Belousov, A., Wessels, R.L., Dehn J (2005). *The January 2005 eruption of Bezymianny Volcano, Russia: Comparing ground and airborne thermal camera images to rapid-response ASTER satellite data.* American Geophysical Union Fall Meeting (abs. V31A-0604).

Based on seismic observations, a large explosion occurred at the summit of Bezymianny Volcano, Kamchatka, Russia on 11 January 2005. This prompted the acquisition of fifteen (four day and eleven night) Advanced Spaceborne Thermal Emission and Reflection Radiometer (ASTER) satellite images of the area over the next eight months. These data provided an unprecedented time series of high-resolution thermal infrared (TIR) data of the volcano and its deposits, as an initial test of the new ASTER rapid-response program (in conjunction with the Alaska Volcano Observatory). A field campaign was undertaken in August 2005 to monitor and interpret recent activity using both ground and airborne Forward Looking Infrared Radiometers (FLIR) surveys. Airborne visual and FLIR observations revealed that the morphology of the summit lava dome had changed significantly since August 2004. The dome currently contains a collapse crater roughly 200 m in diameter and a small viscous lava lobe that drapes the crater

rim. Stepped scarps within the new summit crater suggest a partial collapse mechanism of formation rather than a purely explosion-related origin. Activity in 2005 also created a v-shaped notch in the southern part of the dome, which had observable high temperature fumarolic activity and may be an area of future structural weakness. The January explosion produced a plan-view mushroom shaped deposit branching from the summit that pooled against the 1956 crater wall, with some material travelling up to 3 km to the southeast away from the horseshoe-shaped crater. The FLIR acquisitions detected temperatures above 120° C within these summit deposits, particularly within oval-shaped collapse pits, likely created from deposition of the hot material onto snow and ice. The slow cooling rate is most likely a function of the deposit thickness by the crater rim and the thermal insulation of the surrounding rocks. Observed ASTER thermal anomalies in combination with FLIR and standard photography suggest the events beginning 11 January resulted in the formation of a summit collapse crater, a small viscous lava flow, and a dense block and ash flow that moved initially to the northwest, and then spread out, following the lowest elevation areas within the crater rim. The sequence of these events is still under study using scientific observations made from FLIR and ASTER data.

Carter, A.J., Ramsey, M.S., Durant, A.J., & Skilling, I.P. (2006). *Multitemporal three dimensional imaging of volcanic products on the macro- and micro- scale*. American Geophysical Union Fall Meeting (abs. V53B-1752).

Satellite data from the Advanced Spaceborne Thermal Emission and Reflection Radiometer (ASTER) can be processed using a nadir- and backward-viewing band at the same wavelength to generate a Digital Elevation Model (DEM) at a maximum spatial resolution of 15 metres. Bezymianny Volcano (Kamchatka Peninsula, Russia) was chosen as a test target for multitemporal DEM generation. DEMs were used to generate a layer stack and calculate coarse topographic changes from 2000 to 2006, the most significant of which was a new crater that formed in spring 2005. The eruption that occurred on 11 January 2005 produced a pyroclastic deposit on the east flank, which was mapped and from which samples were collected in August 2005. A comparison was made between field-based observations of the deposit and micron-scale roughness (analogous to vesicularity) derived from ASTER thermal infrared data following the model described in Ramsey and Fink (1999) on lava domes. In order to investigate applying this technique to the pyroclastic deposits, 18 small samples from Bezymianny were selected for Scanning Electron Microscope (SEM) micron-scale analysis. The SEM image data were processed using software capable of calculating surface roughness and vesicle volume from stereo pairs: a statistical analysis of samples is presented using a high resolution grid of surface profiles. The results allow for a direct comparison to field, laboratory, and satellite-based estimates of micron-scale roughness. Prior to SEM processing, laboratory thermal emission spectra of the microsamples were collected and modelled to estimate vesicularity. Each data set was compared and assessed for coherence within the limitations of each technique. This study outlines the value of initially imaging at the macro-scale to assess major topographic changes

over time at the volcano. This is followed by an example of the application of micro-scale SEM imaging and spectral deconvolution, highlighting the advantages of using multiple resolutions to analyse frequently overlapping products at Bezymianny.

Carter, A.J., Ramsey, M.S., & Girina, O.A. (2007b). *Explosive eruption at Bezymianny Volcano, Russia, captured by satellite data.* American Geophysical Union Meeting Joint Assembly (abs. V23A-11).

Bezymianny (55.9º N, 160.6º E, ~2900 m elevation) is an active, explosive volcano within the Central Kamchatka Depression (CKD), Kamchatka Peninsula, Russia. Based on information from the Kamchatka Volcanic Eruption Response Team (KVERT 2006), an explosive eruption occurred at Bezymianny Volcano, Kamchatka, Russia at 09:17 UTC on 24 December 2006. This produced an ash cloud up to ~10 km ASL. We investigate the 24 December 2006 eruption using rapid-response data from the Advanced Spaceborne Thermal Emission and Reflection Radiometer (ASTER), combined with field photographs of the deposit. Furthermore we consider thermal and textural observations on the deposits. Satellite images agreed with aerial photographs taken on 27 December 2006 showing the warm deposit (relative to the snow) concentrated in the south-eastern channel. We present data from rapid response images collected in conjunction to the Alaska Volcano Observatory (AVO) and suggest inferences toward future activity.

Carter, A.J., Ramsey, M.S., & van Manen, S.M. (2007c). *Thermal infrared investigation of the pyroclastic flow deposits and dome region of Bezymianny volcano, Kamchatka, Russia*. American Geophysical Union Fall Meeting (abs. V21A-0386).

Bezymianny (Kamchatka, Russia) is an active stratovolcano that contains a summit lava dome and pyroclastic flow (PF) sheet to the southeast. Two recent eruptions (24 December 2006 and 11 May 2007) generated fresh pyroclastic flows on the southeastern flank. During the winter of 2006, the Advanced Spaceborne Thermal Emission and Reflection Radiometer (ASTER) collected several day- and night-time images to monitor the December eruption deposits and subsequent events. A field campaign in August 2007 was conducted to investigate recent changes at the lava dome and to map the new PF deposits. Within the cloud-free night time ASTER image from 30 June 2007, seven ASTER thermal infrared (TIR) 90 m pixels were identified as being thermally-anomalous and were investigated in the field. Both handheld Forward Looking Infrared Radiometer (FLIR) and thermocouple probe data were obtained and compared to the satellite TIR data. Helicopter- and ground-based FLIR surveys revealed thermally-elevated PF deposits that contained warm blocks and fumaroles. The maximum fumarole temperature within the December 2006 PF deposit was 377C at a distance of five kilometers from the lava dome. At the terminus of the 24 December 2006 PF, seven kilometers from the dome, the maximum temperature recorded was 228C. This suggests that eight months after the December 2006 eruption, the deposit was of a sufficient thickness in this area to retain heat. In addition, the thickness of the deposit probably increased as the slope angle decreased approximately 4 kilometers from dome, which may explain the high temperatures observed. We present spaceborne, airborne and ground-based thermal data in order to compare direct and

remote thermal observations of ongoing activity and provide the first ground-based TIR data of actively cooling PF deposits at Bezymianny.

Carter, A.J., & Ramsey, M.S. (2008b). *Thermal infrared observations of activity at Bezymianny Volcano, Kamchatka, Russia: 14 months of data. IAVCEI General Assembly*. Iceland 2008.

Bezymianny (Kamchatka, Russia) is an active stratovolcano that contains a summit lava dome and pyroclastic flow (PF) sheet to the southeast. Three recent eruptions (24 December 2006, 11 May 2007, and 14 October 2007) generated fresh pyroclastic flows on the south-eastern flank. For each event, the Advanced Spaceborne Thermal Emission and Reflection Radiometer (ASTER) collected several day- and night-time images to monitor the eruptions, pyroclastic deposits and subsequent events. A field campaign in August 2007 was carried out to investigate recent changes at the lava dome and to map the December 2006 and May 2007 PF deposits. Within a cloud-free night time ASTER image from 30 June 2007, seven ASTER thermal infrared (TIR) 90 m pixels were identified as being thermally-anomalous and were investigated in the field. Both handheld Forward Looking Infrared Radiometer (FLIR) and thermocouple probe data were obtained and compared to the satellite TIR data. Helicopter- and ground-based FLIR surveys revealed thermally-elevated PF deposits that contained warm blocks and fumaroles. ASTER TIR data were used to monitor and interpret the three eruptions, with the creation of a geo-located TIR image time series, clearly showing each pyroclastic flow deposit in red, green, and blue. Furthermore, we interpret periods of quiescence, pre-cursory thermal activity, explosive eruption, and post-eruption lava lobe emplacement using ASTER- and ground-based data. We present integrated field-, aerial-, and satellite-derived datasets focussed over the October 2006 to December 2007 time period and provide geological interpretations for activity at the lava dome and deposits in this region.

APPENDIX D

ADDITIONAL SAMPLE DATA COMPARING IMAGE-DERIVED VESICULARITY TO AVERAGE SURFACE ROUGHNESS

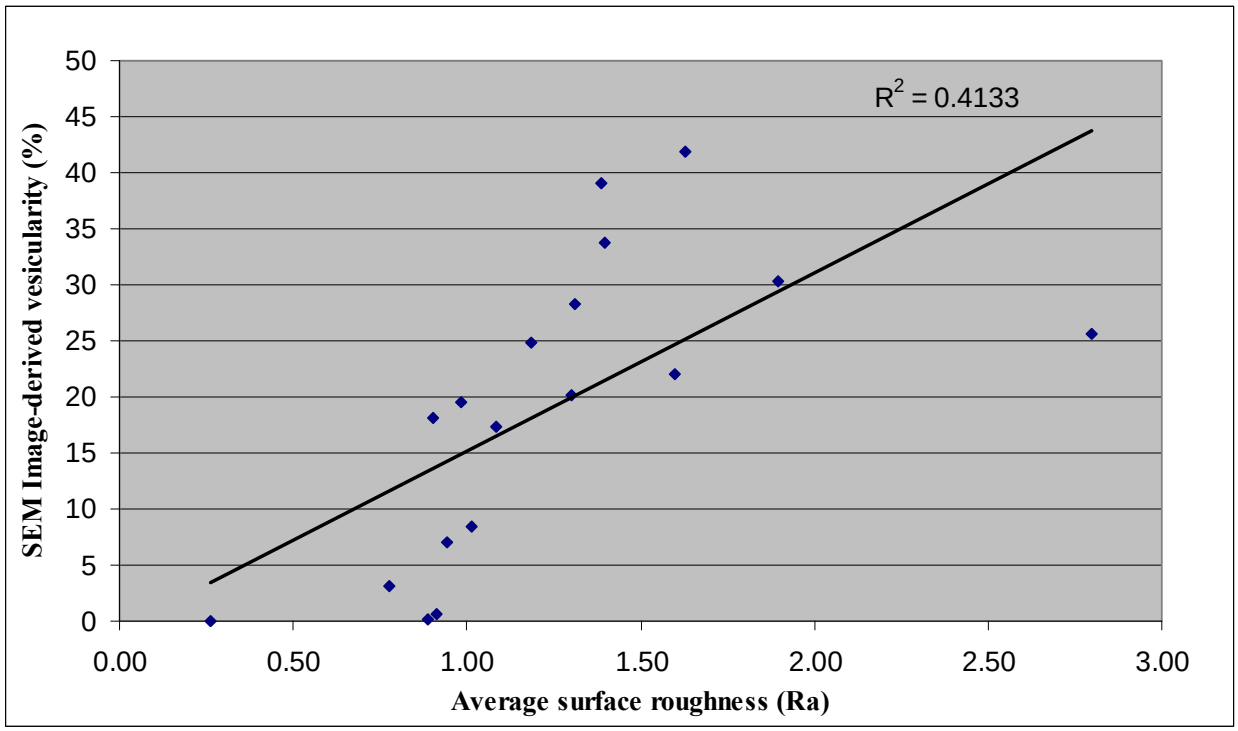

Sample	Description	Ra (μm)	Image-derived vesicularity (%)
MTU-2008-014	Library Obsidian (OBS)	0.26	0.00
MTU-2008-009	2007 batch- sample 014 from May 2007 PF	0.78	3.20
MTU-2008-008	2007 batch- sample 013 from May 2007 PF	0.89	0.15
MTU-2008-001	2003 bezy leveee more dense 8-22-05	0.91	0.70
MTU-2008-006	2007 batch- sample 009 from May 2007 PF	0.94	7.00
MTU-2008-012	2007 batch- sample 024 from May 2007 PF	0.99	19.55
MTU-2008-010	2007 batch- sample 021 from May 2007 PF	1.01	8.45
MTU-2008-007	2007 batch- sample 010 from May 2007 PF	1.08	17.30
MTU-2008-003	2005 PF block 8-19-05 interior	1.19	24.85
MTU-2008-013	Lascar 1993 Plinian eruption pumice	1.31	28.30
MTU-2008-011	2007 batch- sample 023 from May 2007 PF	1.39	39.10
MTU-2008-005	2007 batch- sample 003 from May 2007 PF	1.39	33.70
MTU-2008-004	2005 PF block 8-19-05 exterior	1.63	41.90
MTU-2008-002	2003 bezy levee more vesicular 8-22 -05	1.89	30.35
MTU-2006-001-P4	Carter et al. 2008b	0.90	18.10
MTU-2006-001-P1	Carter et al. 2008b	1.30	20.10
MTU-2006-005	Carter et al. 2008b	1.60	22.00
MTU-2006-004	Carter et al. 2008b	2.80	25.70

BIBLIOGRAPHY

Abrams, M. (2000). The Advanced Spaceborne Thermal Emission and Reflectance Radiometer (ASTER): data products for the high spatial resolution imager on NASA's Terra platform. *International Journal of Remote Sensing*, *21*, 847−859.

Adams, J. B., Smith, M. O., & Johnson, P. E. (1986). Spectral mixture modeling: A new analysis of rock and soil types at the Viking Lander I site, *Journal of Geophysical Research*, *91*, 8098-8112.

Alaska Volcano Observatory (AVO) colour code website (2008). (http://www.avo.alaska.edu/color_codes.php)

Alidibirov, M. A., Bogoyavlenskaya, G. E., Kirsanov, I. T., Firstov, P. P., Girina, O. A., Belousov, A. B., Zhdanova, E. Yu., & Malyshev, A. I. (1990). The 1985 eruption of Bezymianny. *Volcanology and Seismology*, *10*, 839-863.

Anderson, S. W., & Fink, J. H. (1990). The development and distribution of lava textures at the Mount St. Helens dome. In J. H. Fink, (Ed.), *Lava Flows and Domes: Emplacement Mechanisms and Hazard Implications*, *2*, (pp. 25-46). Springer, Berlin.

Arai K, Tonooka, H. (2004). Radiometric performance evaluation of ASTER VNIR, SWIR and TIR. *IEEE Transactions on Geoscience and Remote Sensing*, *43*, 2725-2732.

Bandfield, J. (2002). Global mineral distributions on Mars, *Journal of Geophysical Research, 107,* 5042, doi:10.1029/2001JE001510.

Belousov, A. B. (1996). Deposits of the 30 March 1956 directed blast at Bezymianny volcano, Kamchatka, Russia. *Bulletin of Volcanology*, *57*, 649-662.

Belousov, A. B., & Belousova, M. G. (1998). Bezymyannyi eruption on March 30, 1956 (Kamchatka): Sequence of events and debris-avalanche deposits. *Volcanology and Seismology*, *20*, 29-47.

Belousov, A., Voight, B., Belousova, M., & Petukhin, A. (2002). Pyroclastic surges and flows from the 8–10 May 1997 explosive eruption of Bezymianny Volcano, Kamchatka, Russia. *Bulletin of Volcanology, 64,* 455−471.

Belousov, A., Voight, B., & Belousova, M. (2007). Directed blasts and blast-generated pyroclastic density currents: a comparison of the Bezymianny 1956, Mount St Helens 1980, and Soufrière Hills, Montserrat 1997 eruptions and deposits. *Bulletin of Volcanology, 69,* 701-740.

Blake, S. (1990). Viscoplastic models of lava domes. In J.H. Fink (Ed.), *Lava flows and domes: Emplacement mechanisms and hazard implications*, *Vol. 2* (pp. 88-128). Berlin: Springer.

Bogoyavlenskaya, G. E., & Kirsanov, I. T. (1981). Twenty five years of volcanic activity of Bezymianny. *Volcanology and Seismology, 2,* 3-13 (in Russian).

Bogoyavlenskaya, G. E., Braitseva, O. A., Melekestsev, I. V., Maksimov, A. P., & Ivanov, B. V. (1991). Bezymianny Volcano. In S. A. Fedotov, & Yu. P. Masurenkov (Eds.), *Active volcanoes of Kamchatka, Vol. 1* (pp. 195–197). Moscow: Nauka.

Branney, M. J., & Gilbert, J. S. (1995). Ice-melt collapse pits and associated features in the 1991 lahar deposits of Volcán Hudson, Chile: criteria to distinguish eruption-induced glacier melt. *Bulletin of Volcanology*, *57*, 293-302.

Brantley, S. R., McGimsey, R. G., & Neal, C. A. (2004). The Alaska Volcano Observatory-Expanded Monitoring of Volcanoes Yields Results. *USGS Fact Sheet* 2004-3084:2.

Byrnes, J. M., Ramsey, M. S., & Crown, D. A. (2004). Surface unit characterization of the Mauna Ulu flow field, Kilauea Volcano, Hawai'I, using integrated field and remote sensing analyses, *Journal of Volcanology and Geothermal Research*, *135*, 169-193.

Byrnes, J. M., Ramsey, M. S., King, P. L., & Lee, R. J. (2007). Thermal infrared reflectance and emission spectroscopy of quartzofeldspathic glasses. *Geophysical Research Letters*, *34*, L01306. doi 10.1029/2006GLO27893

Breton González, M., Ramírez, J. J., & Navarro, C. (2002). Summary of the historical eruptive activity of Volcán de Colima, Mexico 1519–2000. *Journal of Volcanology and Geothermal Research*, *117*, 21–46.

Calder, E. S., Luckett, R., Sparks, R. S. J., & Voight, B. (2002). Mechanisms of lava dome instability and generation of rockfalls and pyroclastic flows at Soufrière Hills Volcano,

Montserrat. In T. H. Druitt & P. Kokelaar (Eds.), *The eruption of Soufrière Hills Volcano, Montserrat, from 1995 to 1999* (pp. 173-190). London: Geological Society.

Carter, A. J., Ramsey, M. S., Belousov, A., Wessels, R. L., & Dehn J. (2005). *The January 2005 eruption of Bezymianny Volcano, Russia: Comparing ground and airborne thermal camera images to rapid-response ASTER satellite data.* American Geophysical Union Fall Meeting (abs. V31A-0604).

Carter, A. J., Ramsey, M. S., Durant, A. J., & Skilling, I. P. (2006). *Multitemporal three dimensional imaging of volcanic products on the macro- and micro- scale*. American Geophysical Union Fall Meeting (abs. V53B-1752).

Carter, A. J., Ramsey, M. S., & Belousov, A. B. (2007a). Detection of a new summit crater on Bezymianny Volcano lava dome: satellite and field-based thermal data. *Bulletin of Volcanology*, *69*, 811-815.

Carter, A. J., Ramsey, M. S., & Girina, O. A. (2007b). *Explosive eruption at Bezymianny Volcano, Russia, captured by satellite data.* American Geophysical Union Meeting Joint Assembly (abs. V23A-11).

Carter, A. J., Ramsey, M. S., & van Manen, S. M. (2007c). *Thermal infrared investigation of the pyroclastic flow deposits and dome region of Bezymianny volcano, Kamchatka, Russia*. American Geophysical Union Fall Meeting (abs. V21A-0386).

Carter, A. J., Girina, O. A., Ramsey, M. S., & Demyanchuk, Yu. V. (2008a). ASTER and field observations of the 24 December 2006 eruption of Bezymianny Volcano, Russia. *Remote Sensing of Environment*, *112*, 2569 – 2577.

Carter, A. J., Ramsey, M. S., Durant, A. J., Skilling, I. P., & Wolfe, A. L. (2008b). Micron-scale roughness of volcanic surfaces from thermal infrared spectroscopy and scanning electron microscopy. *Journal of Geophysical Research* (in review).

Carter, A. J., & Ramsey, M. S. (2008a). 14 months of ASTER- and field-based observations at Bezymianny Volcano: focus on the 11 May 2007 pyroclastic flow deposit. *Remote Sensing of Environment* (in review).

Carter, A. J., & Ramsey, M. S. (2008b). *Thermal infrared observations of activity at Bezymianny Volcano, Kamchatka, Russia: 14 months of data. IAVCEI General Assembly*. Iceland 2008.

Christensen, P. R., Bandfield, J. L., Hamilton, V. E., Howard, D. A., Lane, M. D., Piatek, J. L., Ruff, S. W., & Stefanov, W. L. (2000). A thermal emission spectral library of rock-forming minerals. *Journal of Geophysical Research*, *105*, 9735-9739.

Clark, R. N. (2004). Spectroscopy of rocks and minerals, and principles of spectroscopy. In P. L. King, M. S. Ramsey, & G. A Swayze (Eds.), *An Introduction to infrared spectroscopy for geochemistry and remote sensing* (pp 17-55). London, Ontario, Canada: Mineralogical Association of Canada.

Crisp, J., Kahle, A. B., & Abbott, E. A. (1990). Thermal infrared spectral character of Hawaiian basaltic glasses. *Journal of Geophysical Research*, *95*, 21,657–21,669.

Dehn, J., Dean, K. G., & Engle, K. (2000). Thermal monitoring of North Pacific volcanoes from Space. *Geology*, *28*, 755-758.

Donnelly-Nolan, J. M. (1988). A magmatic model of Medicine Lake Volcano, California. *Journal of Geophysical Research*, *93*, 4412-4420.

Druitt, T. H. (1992). Emplacement of the 18 May 1980 lateral blast deposit ENE of Mt St Helens, Washington. *Bulletin of Volcanology*, *54*, 554-572.

Druitt, T. H., Young, S. R., Baptie, B., Bonadonna, C., Calder, E. S., Clarke, A. B., Cole, P. D., Harford, C. L., Herd, R. A., Luckett, R., Ryan, G., & Voight, B. (2002). Episodes of cyclic Vulcanian explosive activity with fountain collapse at Soufrière Hills Volcano. In T. H. Druitt & P. Kokelaar (Eds.), *The eruption of Soufrière Hills Volcano, Montserrat, from 1995 to 1999* (pp. 281-306). London: Geological Society.

Fedotov, S. A., Masurenkov, Yu. P., & Svyatlovsky, A. E. (1991). Foreword. In S.A. Fedotov & Yu. P. Masurenkov (Eds.), *Active Volcanoes of Kamchatka* (pp. 301). Moscow: Nauka.

Feely, K. C., & Christensen, P. R. (1999). Quantitative compositional analysis using thermal emission spectroscopy: Application to igneous and metamorphic rocks. *Journal of Geophysical Research*, *104*, 24195-24210.

Fink, J. H. & Anderson, S. W. (2000). Lava domes and coulees. In H. Sigurdsson, B. F. Houghton, S. McNutt, H. Rymer, & J. Stix (Eds.), *Encyclopedia of Volcanoes* (pp. 307 -319). San Diego: Academic Press.

FLIR ThermaCAM S40 manual (2007). http://www.flirthermography.com/media/S40_datasheet.pdf . Cited February 2007.

Francis, P. (1993). *Volcanoes: A planetary perspective*. New York: Oxford University Press.

Francis, P. W., Wadge, G., & Mouginis-Mark, P. J. (1996). Satellite Monitoring of Volcanoes. In R. Scarpa & R. Tilling (Eds.), *Monitoring and Mitigation of Volcano Hazards* (pp 257-298). New York: Springer-Verlag.

Gillespie, A., Rokugawa, S., Matsunaga, T., Cotherm, J. S., Hook, S., & Kahle, A. B. (1998). A temperature and emissivity separation algorithm for Advanced Spaceborne Thermal Emission and Reflection Radiometer (ASTER) images. *IEEE Transactions on Geoscience and Remote Sensing, 36,* 1113-1126.

Girina, O. A., Senyukov, S. L., Malik, N. A., Manevich, A. G., Ushakov, S. V., Mel'nikov, D. V., et al. (2006). Activity of Kamchatkan and Northern Kuriles (Paramushir Island) volcanoes, Vestnik KRAUNC. *Sciences of the Earth, Vol. 2,* 151−157. http://www.kscnet.ru/kraesc/2006/2006_8/art13.pdf

Goldstein, J. I., Newbury, D. E., Echlin, P., Joy, D. C., Fiori, C., & Lifshin, E. (1981). *Scanning Electron Microscopy and X-Ray Microanalysis*. New York and London: Plenum.

Gorbatov, A., Widiyantoro, S., Fukao, Y., & Gordeev, E. (2000). Signature of remnant slabs in the North Pacific from P-wave tomography. *Geophysical Journal International*, *142*, 27-36.

Gorshkov, G. S. (1959). Gigantic eruption of the Bezymianny volcano. *Bulletin of Volcanology*, *20*, 77-109.

Hamilton, V. E., Christensen, P. R., & McSween, H. Y. (1997). Determination of Martian meteorite lithologies and mineralogies using vibrational spectroscopy. *Journal of Geophysical Research*, *102*, 25,593–25,603.

Hamilton, V. E., & Christensen, P. R. (2000). Determining the modal mineralogy of mafic and ultramafic igneous rocks using thermal emission spectroscopy. *Journal of Geophysical Research*, *105*, 9717-9733.

Hamilton, V. E., & Christensen, P. R. (2005). Evidence for extensive, olivine-rich bedrock on Mars. *Geology, 30*, 433-436.

Hamilton, V. E., Christensen, P. R. McSween Jr., H. Y. & Bandfield, J. L. (2003). Searching for the source regions of Martian meteorites using MGS TES: Integrating Martian meteorites into the global distribution of volcanic materials on Mars. *Meteoritics and Planetary Science*, *38*, 871-885.

Hapke, B. (1993). *Theory of reflectance and emittance spectroscopy*. Ney York: Cambridge University Press.

Harbert, W. (1992). Geological interpretation of northern Kamchatka, Russia. EOS (September), 45-47.

Harbert, W., Kepezhinskas, P, Krylov, K., Grigoriev, V., Sokolov, S., Aleksutin, M., Heiphetz, A., & Layer, P. (1998). Paleomagnetism and tectonics of the Kamchatka region, northeastern Russia: Implications for the development and evolution of the northwest Pacific basin. *Polarforschung*, *68*, 297-308.

Harris, A. J. L., & Maciejewski, A. J. H. (2000). Thermal survey's of the Vulcano Fossa fumarole field 1994-1999: evidence for fumarole migration and sealing. *Journal of Volcanology and Geothermal Research, 102*, 119-147.

Harris, A. J. H., Dehn, J., Patrick, M., Calvari, S., Ripepe, M., & Lodato, L. (2005). Lava effusion rates from hand-held thermal infrared imagery: An example from the June 2003 effusive activity at Stromboli. *Bulletin of Volcanology*, *68*, 107-117.

Heiken, G., & Wohletz, K. H. (1985). *Volcanic Ash*. Berkeley: University of California Press.

Houghton, B. F., & Wilson, C. J. N. (1989). A vesicularity index for pyroclastic deposits. *Bulletin of Volcanology*, *51*, 451-462.

Hunt, G. R. (1976). Infrared spectral behavior of fine particulate solids. *Journal of Physical Chemistry*, *80*, 1195-1198.

International Standard Norme Internationale (1997). *Geometrical Product Specifications (GPS)-Surface texture: Profile method – Terms, definitions and surface texture parameters*. Global Engineering Documents, ISO document 4287.

James, M. R., Robson, S., Pinkerton, H., & Ball, M. (2006). Oblique photogrammetry with visible and thermal images of active lava flows. *Bulletin of Volcanology*, *69*, 105-108.

Jensen, J. R. (2006). *Remote Sensing of the Environment: An Earth Resource Perspective*. Upper Saddle River, New Jersey: Prentice Hall.

Kamchatka Volcanic Eruption Response Team (KVERT) Report (2005). Bezymianny Volcano, 11 January 2005. http://www.avo.alaska.edu/activity/avoreport.php?view=kaminfo&id=47&type=kaminfo&month=January&year=2005. Cited January 2005.

Kamchatka Volcanic Eruption Response Team (KVERT) Report (2006). Bezymianny Volcano, 9 May 2006. http://www.avo.alaska.edu/activity/avoreport.php?view=kaminfo&id=172&type=kaminfo&month=May&year=2006. Cited May 2006.

Kamchatka Volcanic Eruption Response Team (KVERT) Report (2007). Bezymianny Volcano. (http://www.avo.alaska.edu/activity/avoreport.php).

King, P. L., Ramsey, M. S., McMillan, P. F., & Swayze, G. (2004). Laboratory fourier transform infrared spectroscopy methods for geologic samples. In P. L. King, M. S. Ramsey, & G. A. Swayze (Eds.), *Infrared Spectroscopy in Geochemistry, Exploration Geochemistry, and Remote Sensing*, *Vol. 33* (pp. 57-91). London, Ontario: Mineralogical Association of Canada.

Kirianov, V. Y., Neal, C. A., Gordeev, E. I., & Miller, T. P. (2002). The Kamchatkan Volcanic Eruption Response Team (KVERT). *USGS Fact Sheet*, 2002-064-02.

Kirkland, L. E., Herr, K. C., Keim, E. R., Adams, P. M., Salisbury, J. W., Hackwell, J. A., & Treiman, A. (2002). First use of a Thermal Infrared hyperspectral scanner for compositional mapping. *Remote Sensing of Environment*, *80*, 447-459.

Klug, C., & Cashman, K. V. (1994). Vesiculation of the May 18, 1980, Mount St. Helens magma, *Geology*, *22*, 468-472.

Levin, V., Shapiro, N., Park, J., & Ritzwoller, M. (2002). Seismic evidence for catastrophic slab loss beneath Kamchatka. *Nature*, *418*, 763-767.

Lodato, L., Spampinato, L., Harris, A., Calvari, S., Dehn, J., & Patrick, M. (2007). The morphology and evolution of the Stromboli 2002-2003 lava flow field: an example of a basaltic flow field emplaced on a steep slope. *Bulletin of Volcanology*, *69*, 661-679.

Lyon, R. J. P. (1965). Analysis of rocks by spectral infrared emission (8-25 microns). *Economic Geology*, *60*, 715-736.

Mackey, K. G., Fujita, K., Gunbina, L. V., Kovalev, V. N., Imaev, V. S., Koz'min, B. M., & Imaeva, L. P. (1997). Seismicity of the Bering Strait region; evidence for a Bering Block. *Geology*, *25*, 979-982.

Matthews, S. J., Gardeweg, M. C., & Sparks, R. S. J. (1997). The 1984 to 1996 cyclic activity of Láscar Volcano, northern Chile: cycles of dome growth, dome subsidence, degassing and explosive eruptions. *Bulletin of Volcanology*, *59*, 72-82.

Maxwell, J. C. (1991). *A Treatise on Electricity and Magnetism*. New York: Dover.

McCormick, M., Thomason, L. W., & Trepte, C. R. (1995). Atmospheric effects of the Mt Pinatubo eruption. *Nature*, *373*, 399-404.

Miller, T. P., & Casadevall, T. J. (2000). Volcanic Ash Hazards to Aviation. In H. Sigurdsson, B.F. Houghton, S. McNutt, H. Rymer, & J Stix (Eds.), *Encyclopedia of Volcanoes* (pp. 915 - 930). San Diego: Academic Press.

Minnich, B., Bartell, H., Leeb, H., Bernroider, E. W. N, Krautgartner, W. D., & Lametschwandtner, A. (2001). Quantification of microvasculature by SEM and 3D morphometry, *Microscopy and Analysis*, *15*, 27-29.

Minitti, M. E., Hamilton, V. E., & Wyatt M.B. (2007). *Deconvolution of Martian thermal infrared spectra using a simplified, glass-rich library*. Lunar and Planetary Science Meeting. XXXVIII, Houston (abs. 2099).

Moersch, J. E., & Christensen, P. R. (1995). Thermal emission from particulate surfaces: A comparison of scattering models with measured spectra. *Journal of Geophysical Research, 100*, 7465-7477.

Moersch, J. E., Horton, K. A., Lucey, P. G., & Ruff, S. W. (2002). *Characterization of target adjacency effects in horizontal-viewing thermal infrared spectroscopy, with applications to the MER Mini-TES experiment*. Lunar and Planetary Science Conference #XXXIII, p. 1447.

Nakada, S., Miyake, Y., Sato, H., Oshima, O., & Fujinawa, A. (1995). Endogenous growth of dacite dome at Unzen volcano (Japan), 1993-1994, *Geology*, *23*, 157-160.

Newhall, C. G., & Self, S. (1982). The Volcanic Explosivity Index (VEI): an estimate of explosive magnitude for historical volcanism. *Journal of Geophysical Research*, *87*, 1231-1238.

Newton, I. (1704). *Opticks: Or, A treatise of the Reflections, Refractions, Inflexions and Colours of Light*. London.

Ondrusek, J., Christensen, P. R., & Fink, J. H. (1993). Mapping the distribution of vesicular textures on silicic lavas using the Thermal Infrared Multispectral Scanner. *Journal of Geophysical Research*, 98, 15903-15908.

Oppenheimer, C., Francis, P. W., Rothery, D. A., Carlton, R. W. T., & Glaze, L. S. (1993). Infrared Image analysis of Volcanic Thermal Features: Láscar Volcano, Chile, 1984-1992. *Journal of Geophysical Research*, *98*, 4269-4286.

Ozerov, A.Y., Ariskin, A. A., Kyle, P., Bogoyavlenskaya, G. E., & Karpenko, S. F. (1997). Petrological-geochemical model for genetic relationships between basaltic and andesitic magmatism of Klyuchevskoy and Bezymyanni volcanoes, Kamchatka. *Petrology*, *5*, 550-569.

Papp, K. P., Dean, K. G., & Dehn, J. (2005). Predicting regions susceptible to high concentrations of airborne volcanic ash in the North Pacific region: *Journal of Volcanology and Geothermal Research, 148,* 295-314.

Patrick, M. R., Smellie, J. L., Harris, A. J. L., Wright, R., Dean, K., Izbekov, P., Garbeil, H., & Pilger, E. (2005). First recorded eruption of Mount Belinda volcano (Montagu Island), South Sandwich Islands. *Bulletin of Volcanology*, *67*, 415-422.

Patrick, M. R., Harris, A. J. L., Ripepe, M., Dehn, J., Rothery, D. A., & Calvari, S. (2007). Strombolian explosive styles and source conditions: insights from thermal (FLIR) video. *Bulletin of Volcanology*, *69*, 769-784.

Peyton, V., Levin, V., Park, J., Brandon, M., Lees, J., Gordeev, E., & Ozerov, A. (2001). Mantle Flow at a slab edge: seismic anisotropy in the Kamchatka region. G*eophysical Research Letters*, *28*, 379-382.

Pieri D., & Abrams, M. (2004). ASTER watches the world's volcanoes: a new paradigm for volcanological observations from orbit. *Journal of Volcanology and Geothermal Research*, *135*, 13-28.

Podsiadlo, P., & Stachowiak, G. W. (1997). Characterization of surface topography of wear particles by SEM stereoscopy. *Wear*, *206*, 39-52.

Ramsey, M. S., & Christensen, P. R. (1998). Mineral abundance determination- Quantitative deconvolution of thermal emission spectra. *Journal of Geophysical Research*, *103*, 577-596.

Ramsey, M. S., & Fink, J. H. (1999). Estimating silicic lava vesicularity with thermal remote sensing: a new technique for volcanic mapping and monitoring. *Bulletin of Volcanology*, *61*, 32-39.

Ramsey, M. S. (2004). Quantitative geological surface processes extracted from infrared spectroscopy and remote sensing. In P. L. King, M. S. Ramsey, & G. A. Swayze (Eds.), *Infrared Spectroscopy in Geochemistry, Exploration Geochemistry, and Remote Sensing*, *Vol. 33* (pp. 197-213). London, Ontario: Mineralogical Association of Canada.

Ramsey, M. S., & Dehn, J. (2004). Spaceborne observations of the 2000 Bezymianny, Kamchatka eruption: The integration of high-resolution ASTER data into near real-time monitoring using AVHRR. *Journal of Volcanology and Geothermal Research*, *135*, 127-146.

Ramsey, M. S., Dehn, J., Wessels, R., Byrnes, J., Duda, K., Maldonado, L., & Dwyer, J. (2004). *The ASTER emergency scheduling system: A new project linking near-real-time satellite monitoring of disasters to the acquisition of high-resolution remote sensing data.* American Geophysical Union Fall Meeting (abs. SF23A-0026).

Ramsey, M. S., Schneider, D., Wessels, R., & Clark, M., (2005). *Modeling the ascent rate of the 2004 Mount St. Helens lava body using pre-eruption airborne thermal infrared camera data*. American Geophysical Union Fall Meeting (abs. V53D-1604).

Rasband, W. S. (1997). ImageJ, U. S. National Institutes of Health, Bethesda, Maryland, USA, http://rsb.info.nih.gov/ij/

Realmuto, V. J. (1990). Separating the effects of temperature and emissivity: Emissivity spectrum normalization. In E. A. Abbott (Ed.), *Proceedings of the second thermal infrared multispectral scanner (TIMS) workshop*. Pasadena, CA: Jet Propulsion Laboratory.

Rothery, D. (1989). Volcano Monitoring by Satellite. *Geology Today*, *11*, 1665-1667.

Ruff, S. W., Christensen, P. R., Barbera, P. W., & Anderson, D. L. (1997). Quantitative thermal emission spectroscopy of minerals: A laboratory technique for measurement and calibration, *Journal of Geophysical Research*, 14,899-14,913.

Sabins, F. (1987). *Remote Sensing: Principles and Interpretation*. New York: WH Freeman and Co.

Salisbury, J. W., Wald, A., & D'Aria, D. M. (1994). Thermal-infrared remote sensing and Kirchoff's law, 1, Laboratory measurements. *Journal of Geophysical Research*, *99*, 11897-11911.

Sarda, P., & Graham, D. (1990). Mid-ocean ridge popping rocks: implications for degassing at ridge crests, *Earth and Planetary Science Letters*, *97*, 268-289.

Simkin, T., & Siebert, L. (1994). *Volcanoes of the World*. Tuscon, AZ: Geoscience Press.

Sobel, M. (1987). *Light*. Chicago: University of Chicago Press.

Song, S-R., Jones, K. W., Lindquist, B. W., Dowd, B. A., & Sahagian, D. L. (2001). Synchrotron X-ray computed microtomography: studies on vesiculated basaltic rocks. *Bulletin of Volcanology*, *63*, 252-263.

Stevens, N. F., Garbeil, H., & Mouginis-Mark, P. J. (2004). NASA EOS Terra ASTER: Volcanic topographic mapping and capability. *Remote Sensing of Environment*, *90*, 405-414.

Swanson, D. A., Dzurisin, D., Holocomb, R. T., Iwatsubo, E. Y., Chadwick, W. W. Jr., Casadevall, T. J., Ewert, J. W., & Heliker, C. C. (1987). Growth of the lava dome at Mount Saint Helens, Washington (USA), 1981-1983. In J. H. Fink (Ed.), *The emplacement of silicic lava domes and lava flows*. Geological Society of America Special Paper, *Vol. 212* (pp. 1-16).

Thomas, T. R., (1999). *Rough Surfaces* (2nd edition). London: Imperial College Press.

Thome, K., Palluconi, F., Takashima, T., & Masuda, K. (1998). Atmospheric Correction of ASTER. *IEEE Transactions on Geoscience and Remote Sensing*, *36*, 1199-1211.

Thomson, J. L., & Salisbury, J. W. (1993). The mid-infrared reflectance of mineral mixtures. *Remote Sensing of Environment*, *45*, 1-13.

Vaughan, R. G., Hook, S. J., Ramsey, M. S., Realmuto, V. J., & Schneider, D. J. (2005). Monitoring eruptive activity at Mount Saint Helens with TIR image data. *Geophysical Research Letters*, *32*, L19305. doi:10.1029/2005GL024112

Walker, G. P. L., & McBroome, L. A. (1983). Mount Saint Helens 1980 and Mount Pelée 1902: flow or surge? *Geology*, *11*, 571-574.

Watts, R. B., Herd, R. A., Sparks, R. S. J., & Young, S. R. (2002). Growth patterns and emplacement of the andesitic lava dome at Soufrière Hills Volcano, Montserrat. In T. Druitt, & P. Kokelaar (Eds.), *The eruption of Soufrière Hills Volcano, Montserrat, from 1995 to 1999* (pp. 115-152). London: Geological Society.

Yamaguchi, Y., Kahle, A. B., Pniel, M., Tsu, H., & Kawakami, T. (1998). Overview of Advanced Spaceborne Thermal Emission and Reflection Radiometer (ASTER). *IEEE Transactions on Geoscience and Remote Sensing*, *36*, 1062-1071.

Yogodzinski, G. M., Lees, J. M., Churikova, T. G., Dorendorf, F., Wöerner, G., & Volynets, O. N. (2001). Geochemical evidence for the melting of subducting oceanic lithosphere at plate edges. *Nature*, *409*, 500-504.